Analysis of the Radiation Field in ATLAS Using 2008-2011 Data from the ATLAS-MPX Network

Michael Campbell[a], **Erik Heijne**[a, c], **Claude Leroy**[b], **Jean-Pierre Martin**[b], **Giuseppe Mornacchi**[a], **Marzio Nessi**[a], **Stanislav Pospisil**[c], **Jaroslav Solc**[c], **Paul Soueid**[b], **Michal Suk**[c], **Daniel Turecek**[c] **and Zdenek Vykydal**[c*]

[a] *CERN,*
CH-1211 Geneva 23, Switzerland
[b] *Université de Montréal,*
Montréal (Québec), H3C 3J7, Canada
[c] *Institute of Experimental and Applied Physics, Czech Technical University in Prague,*
Horská 3a/22, 12800 Praha 2, Czech Republic

E-mail: zdenek.vykydal@utef.cvut.cz

ABSTRACT: The ATLAS-MPX group has installed a network of 16 Medipix2 pixel detector-based, single-quantum-sensitive devices before the LHC start-up in 2008 at various positions in the ATLAS experimental and technical caverns. The aim of the network is to perform real-time measurements of spectral characteristics and composition of the radiation environment inside the ATLAS detector during its operation and in particular already in the early stages with low luminosity. The detectors are generally sensitive to all radiation species capable to deposit energy of at least 8 keV per single pixel. With the devices, in two different modes of operation, a large dynamic range of particle flux can be covered, of at least 9 orders of magnitude, which corresponds to the highest luminosity, while also background measurement can be made. An important goal is the determination of the neutron component of the mixed radiation field. To identify different types of neutrons, the 300 μm thick silicon sensor area of each ATLAS-MPX device is divided into several regions, covered by different neutron converter materials. A ^{6}LiF layer is used for thermal neutron detection and a polyethylene foil for fast neutron detection. The calibration of the detection efficiency for several energies in different regions of all devices has been performed with various known neutron sources: ^{252}Cf, ^{241}AmBe, thermal neutrons and 14 MeV neutrons from Van de Graaff accelerator. Based on these calibrations the spectral composition of the unknown neutron field can be estimated by comparing the responses from different regions. ATLAS-MPX devices have been operated almost continuously starting from early 2008 (background and cosmic radiation measurements and the first LHC beam appearances in 2008 and 2009) through the stable LHC operation during the 2010 and 2011 run periods up to nowadays. Data are acquired instantaneously by each detector station, with adaptable exposure times (currently 0.1 ms – 600 s) according to local particle flux. Rates of incidence of different particle types normalized per area and per luminosity during regular LHC running are evaluated online. This report highlights a selection of the results. Measured thermal neutron fluxes are found to be largely in agreement with the original simulations, mostly within a factor of two. Significant deviations are observed in the low radiation regions of ATLAS cavern, where measured thermal neutron fluxes are found to be lower than predicted by Monte Carlo simulations. High sensitivity of ATLAS-MPX devices also permits determination of LHC induced radioactivity. Starting from luminosity of about 10^{30} cm^{-2}.s^{-1} the induced radioactivity of short lived radionuclides has become observable. Presently also radioactive decays with longer half-lives are measurable. Online responses of the ATLAS-MPX devices follow reliably the course of the luminosity curve. Devices close to the beam demonstrated

ATL-GEN-PUB-2013-001
29 April 2013

* Corresponding author.

enough sensitivity to visualize van der Meer luminosity scans and provide measurement of the effective overlapping beam sizes and maximum collision rate.

KEYWORDS: ATLAS, LHC, Pixel detector, Neutron detection, Luminosity, Activation, Radiation fields.

Contents

1. Introduction

The precise evaluation of spectral characteristics and composition of radiation in and around the ATLAS detector is necessary for understanding the performance of various detector systems and to predict their useful lifetimes. The results of these measurements may prove to be an important feedback for data analysis and improvement of data taking strategy, particularly in the early phase of operation. For this purpose a network of 16 ATLAS-MPX detecting devices has been installed in the ATLAS experiment. This system is capable of providing quantitative real-time information on fluxes and flux distributions of the main radiation species in the experiment including thermal and fast neutrons. The proposal for installation and operation of this system was originally made in 2006 [1], [2]. Three tasks were identified from an operational point of view:

1) Measurement of the radiation field inside the ATLAS detector volume.
2) Measurement of background radiation in the experimental hall and in the detector surroundings.
3) Measurements close to some selected sub-detectors to determine characteristics such as particle/energy leakage, punch through, etc., which can contribute to the evaluation of their performances.

The ATLAS-MPX devices are based on the Medipix2 hybrid silicon pixel detector which was developed by the Medipix2 Collaboration [3]. It consists of a 2 cm^2 silicon sensor matrix, 256 × 256 cells, bump-bonded to a readout chip. Each matrix element (55 μm × 55 μm pixel, 300 μm thick) is connected to its respective readout chain integrated on the readout chip. Settings of the pulse height discriminators determine the input energy window and at the same time provide noise suppression. A counter in each pixel records interacting quanta of radiation, X- and γ-photons, neutrons, electrons, MIPs[1], ions, falling within the preset energy window (see Fig. 1 as an example).

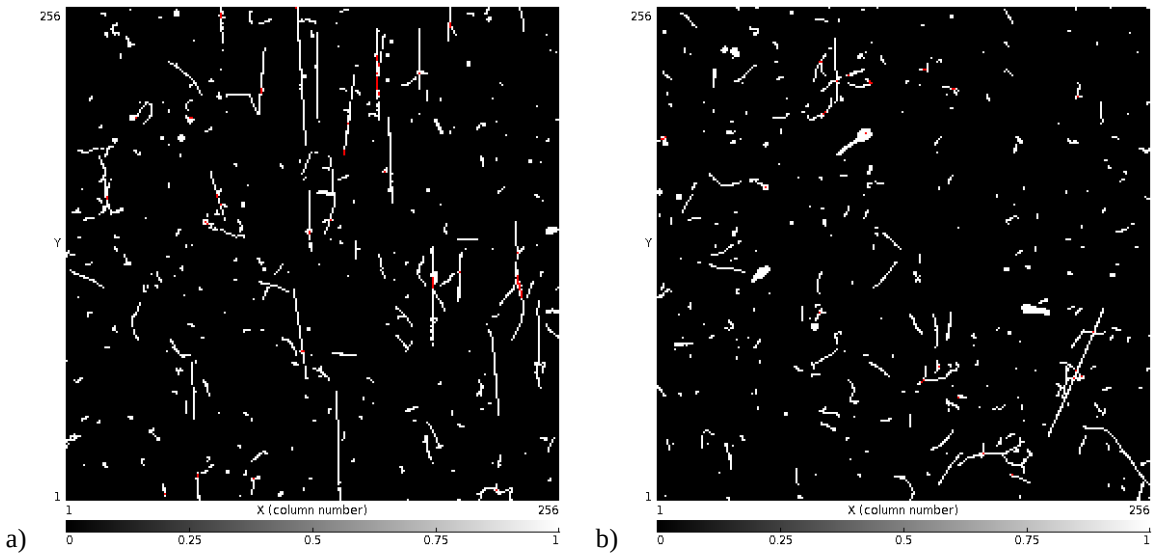

Figure 1. Radiation field in ATLAS as seen on 29th September 2011 (a) by an ATLAS-MPX detector placed horizontally with the detector plane parallel to beam pipe behind the forward muon wheels with an exposure time of 10 s and (b) by one on the small wheel with exposure time of 0.5 s. The tracks in (a), in reality are horizontally coming from the ATLAS region close to the interaction point (IP) because the detector is turned. In (b) the detector plane is perpendicular to the beam direction.

[1] Minimum Ionizing Particles

Using the adjustable energy threshold, the devices can be used for position and energy sensitive spectroscopic detection of radiation, from energy of 5 keV up to tens of MeV deposited in the silicon sensitive volume. Some more details on the MPX detectors will be described in section 2.1.

The radiation level inside and around the ATLAS detector ranges over more than seven orders of magnitude, and it is a challenge to study background levels as well as operational conditions during high luminosity collisions with the same device. The characteristics of the MPX detectors allow a very large dynamic range to be covered, of at least 9 orders of magnitude, by the use of two different modes of analyzing the detector output. The "cluster-tracking" mode which permits to visualize individual cluster of every charged particle interacting in the sensor (tracking mode) and the "pixel-hit-counting" mode (counting mode) will be described in section 2.2.

For neutron detection, the silicon detectors are covered with neutron converters (^{6}LiF for moderated (thermalized), in the following text referred to as "thermal", and polyethylene for fast neutrons, respectively). The calibration procedures will be detailed in section 2.3 and Appendix B.

From the total of 16 detectors of this standalone system, 13 are located in critical positions inside the ATLAS detector and 3 in the space outside. Precise location and the information expected from this disposition can be found in section A.1.3.

In section 3 the operation of the ATLAS-MPX detector network is described starting from early 2008 until middle of 2011. The typical results of the operation are presented in separate subsections for the different periods from 2008 to 2011.

The ATLAS-MPX detectors register that collisions take place at the ATLAS interaction point at a given time and measure the correlated radiation field for each particle species around each sub-detector and in the cavern as analyzed in section 1. In particular, section 4.3 presents the treatment of data taken during van der Meer luminosity scans in May 2010, October 2010 and May 2011.

Section 5 discusses the material activation in the ATLAS environment due to high radiation during collisions. The ATLAS-MPX detectors measure electrons and gamma photons from decay of radionuclides produced by the interaction of primary and secondary particles with surrounding materials. Comparison with dose rate calibration measurements using gamma sources permits an estimate of a photon ambient dose equivalent rate H*(10).

In section 6 we present the preliminary comparison between results of our measurements and earlier simulations. The different components, neutrons, gamma and X-rays, electrons, ions, MIPs, are studied separately. Mostly, there is a good correspondence, better than a factor 2. Exception is the radiation field outside the ATLAS detector, where our measurements indicate a 10-30 times lower particle flux.

Data generated by the ATLAS-MPX network are available at the ATLAS web page: http://atlas.web.cern.ch/Atlas/Collaboration/ under Detector Operation / Infrastructure / Radiation Monitors / ATLAS-MPX and are regularly sent to the ATLAS control room. A manual for accessing the information is found in Appendix A.

Conclusions and proposed future improvements of the ATLAS-MPX detector network are given in section 7.

2. The ATLAS-MPX detector

2.1 Description of the ATLAS-MPX detector unit

The ATLAS-MPX detector comprises the neutron enhanced position sensitive assembly mounted on the printed circuit board with passive components, connectors and drivers for three Ethernet cables (Fig. 3a left). The assembly itself consists of a silicon sensor of sensitive area about 2 cm^2, 300 μm thick and a Medipix2 [4] readout chip. It has a matrix of 256 × 256 pixels, each with an area of 55 μm × 55 μm, bump-bonded together. Each of the 65536 readout chains provides a preamplifier, a 13-bit counter and two discriminators (see pixel schematics in Fig. 2). An energy window can be set globally with lower and upper thresholds between 5 keV and ~500 keV. Pixel to pixel equalization is possible with 3 bit tuning. Setting of the lower threshold above the electronic noise allows noise-free operation. The maximum count rate sustained per pixel is ~100 kHz making possible to register 10^9 pixel hits per cm^2 per second.

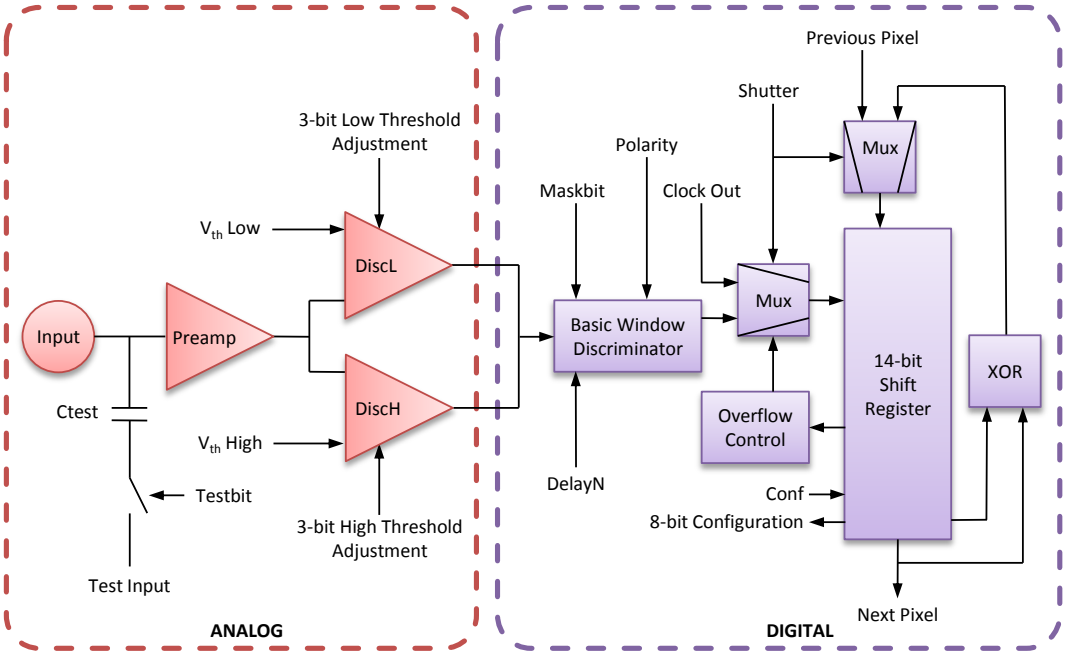

Figure 2. Medipix2 pixel cell block diagram. In red the analog part of the pixel and in violet the digital side.

When hitting the silicon sensor, an incoming particle deposits energy which creates free charge carriers. If the charge-generated signal exceeds the threshold, the pixel is activated and the counter is incremented by one. A single particle can activate one or several pixels forming a cluster of neighboring pixels. Cluster shape strongly depends on the physics of the interaction of the particle with the sensor material and on the process of charge collection. Different shapes are visible in the recorded frames (e.g., Fig. 1) similarly to what can be observed, for instance, in nuclear emulsion or bubble chamber.

All pixels are exposed simultaneously with a common, electronically adjustable shutter that allows precise selection of exposure times (within few ns) from 10 μs to minutes or hours. This precise exposure control is another key to the large dynamic range. Particle hits outside the active exposure time are simply not recorded in the counters. The resulting 256 × 256 pixel frame shows the illuminated pixels against the zero-count (not hit) pixels. After exposure, the counters of all pixels are read out in ~6 s to obtain a snapshot with a frame rate of 0.15 fps (frames per second).

a)  b) 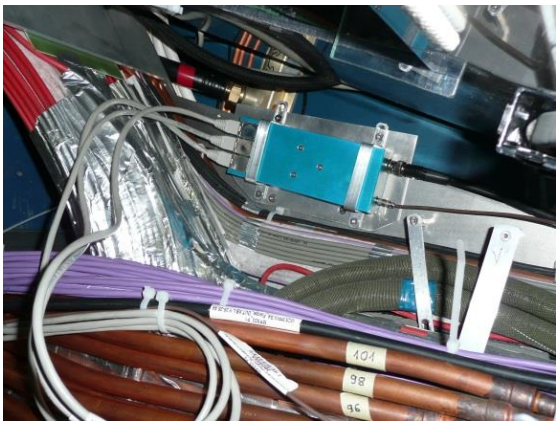

Figure 3. a) The ATLAS-MPX detector with the LVDS adapter (on the left) and the Universal Serial Bus (USB) based readout interface which controls the detector (on the right); b) Placement of an ATLAS-MPX (MPX 03) detector mounted in the blue duralumin box in real ATLAS environment.

The detector data acquisition is controlled by the Universal Serial Bus (USB) based readout interface (Fig. 3a yellow-blue box on the right). Because the ATLAS-MPX detectors are mostly operated at positions in high radiation level, the USB interfaces are located in USA15 and the connection with the ATLAS-MPX detector is achieved through LVDS[2] signals - 3× Ethernet cables, 1× power cable (5 V), 1× bias cable (100 V) (Fig. 3a on the left). Each ATLAS-MPX detector is fitted in a blue duralumin box (see MPX03 on Fig. 3b) with dimensions of 160 mm × 25 mm × 60 mm and an appropriate entrance window.

For neutron detection, each detector is covered with a mask of converter materials dividing its area into regions sensitive to different types of neutrons (thermal and fast). In the masked regions, the sensor is shielded against free alpha particles and other short-range ionizing particles. The structure of neutron converters is shown in Fig. 4a, where converting materials, ^{6}LiF and polyethylene (PE), are recognizable. These materials and their overlap with the aluminum support foils divide the sensitive area of each detector into six different regions as shown on Fig. 4b. The ^{6}LiF layer region (1), 3 mg/cm^2 thick sprayed powder below a 50 μm thick aluminum foil faced to silicon sensor, is used for thermal neutrons detection, exploiting the large cross section of the ^{6}Li(n,α)^{3}H reaction. To enhance sensitivity to fast neutrons a technique of recoil protons from polyethylene foil 1,3 mm thick (region 2) is used. Fast neutrons can be also directly registered via their nuclear reactions in silicon itself and in surrounding materials. The PE+Al region (3), 1.3 mm thick polyethylene layer on 100 μm thick aluminum support, allows measurement of recoiling protons which penetrate Al support (with energies above 3.5 MeV). Here the aluminum foil acts as energy threshold. The 100 μm thick Al foil (4) serves as an attenuator of low energy muons, electrons and X-rays. Thick Al foils (5), 50 μm + 100 μm thick aluminum, achieve further electron and X-ray attenuation. Some remaining uncovered area (6) is directly exposed to all incoming radiation. This region is almost insensitive to slow (thermal) neutrons, the fast neutrons can only be detected via nuclear reactions in silicon Si(n,p)Al and Si(n,α)Mg. The efficiencies of the masks are discussed in section 2.3.

[2] Low Voltage Differential Signaling

a) 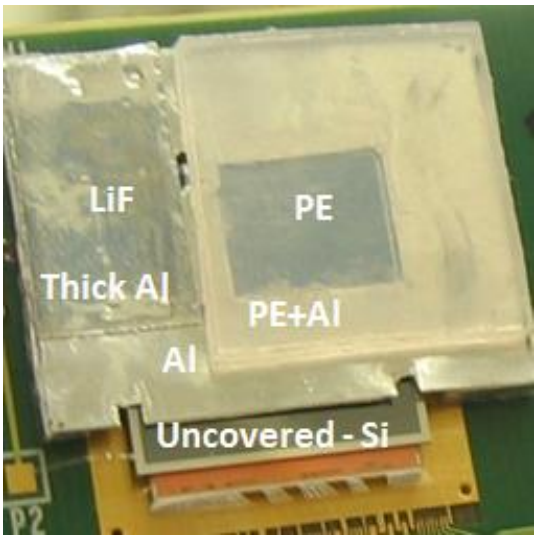

b) 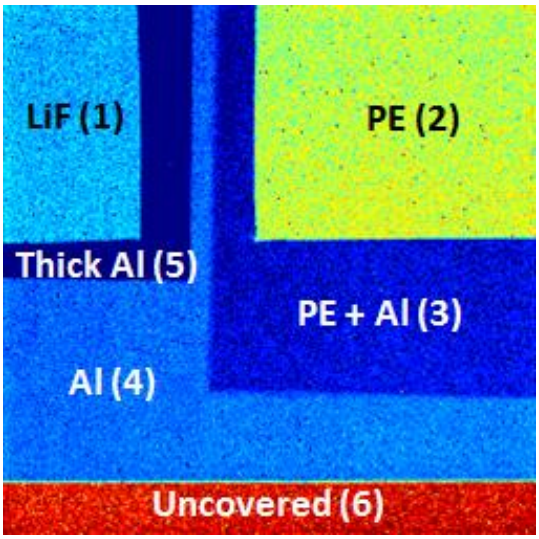

Figure 4. View on the MPX sensor covered with conversion layers (a) and X-ray radiogram of the MPX detector conversion layers (b). Labels are explained in the text.

2.2 Modes of operation

The ATLAS-MPX detectors are usually operated at the lowest possible threshold (LT). The criterion is that there are no noisy pixels in the frame. The device can also be used with high threshold setting (HT) so that particles with low energy transfer (LETP) are discriminated. The recorded frames in either situation can be analyzed in two different complementary modes: the cluster-tracking mode and the pixel-hits counting mode. In this way a very large dynamic range can be achieved.

A.1.1 Cluster-tracking mode – pattern recognition and particle assignment

The cluster-tracking mode (or shortly tracking mode) is based on the observation and analysis of shapes of individual clusters as generated by individually interacting particles [5]. It is applicable at low particle rates or shorter exposure times to avoid cluster overlap and enable cluster shape recognition. It is the preferred mode of measurement for the ATLAS-MPX network operation. At present LHC luminosity this mode permits the observation of individual clusters in the sensitive silicon volume and allows an assignment of clusters to individual interacting quanta of radiation. The signature of interacting particle is seen as a cluster of adjoining activated pixels with different size and shape depending on the type of particle, its energy, incidence angle and the nature of its interactions in the detector sensitive volume. The operation of a pixel detector in tracking mode requires the use of a pattern recognition software. The clusters are classified according to the following characteristics:

- area (number of adjacent activated pixels);
- roundness (comparing cluster area to length of its border);
- linearity (consistency of activated pixels in the cluster with straight-line track);
- width of the straight track.

Low pixel threshold value (8 - 10 keV) is set for measuring in tracking mode. This low threshold is necessary to record single photons, electrons and MIPs. Photons are detected indirectly. They can deposit energy through three interactions: photoelectric effect, Compton scattering and pair creation. In each case, they transfer all or part of their energy to electrons or electron – positron pairs, which are detected. Low energy X-rays and electrons will leave dots labeled 1) in Fig. 5a. More energetic gamma rays, X-rays and electrons are observed either as small blobs, labeled 2) in Fig. 5a, or as curly tracks, labeled 3) in Fig. 5a. These types of clusters are classified as signatures of particles with low energy transfer (LETP).

Minimum ionizing hadrons, muons and electrons produce continuous long straight tracks, labeled 6) in Fig. 5a. Their clusters are easily recognizable except when they are hitting nearly perpendicularly the silicon layer and thus activate only a few pixels. To be classified by the pattern recognition algorithm undoubtedly as MIPs, incident particles must create a thin straight track of at least 20 pixels length in the sensor.

Clusters generated by heavy charged non-relativistic particles like low-energy protons, alpha particles, nuclear fragments and ions will typically appear as heavy blobs, labeled 4) in Fig. 5b, or heavy tracks, labeled 5) in Fig. 5b, depending on their energy and incidence. Cluster types 4 and 5 fall into the category of particles with high energy transfer (HETP).

Neutrons are detected via secondary HETPs produced in convertors. Thermal neutrons appear as heavy blobs caused by $^{6}Li(n,\alpha)^{3}H$ reactions [6]. Fast neutrons are observable below the PE converter as blobs or heavy tracks of recoiled protons [7]. The typical ionization density according to the Bragg ionization law can even be recognized in the sensor (see cluster 5 in Fig. 5b). Moreover, fast neutrons also generate signals everywhere in the silicon sensor via nuclear recoils or reactions as illustrated in Fig. 7.

The reliability of the cluster pattern recognition procedure was tested with measurements of alpha, beta, gamma, neutron sources, in proton beams and in their mixed fields.

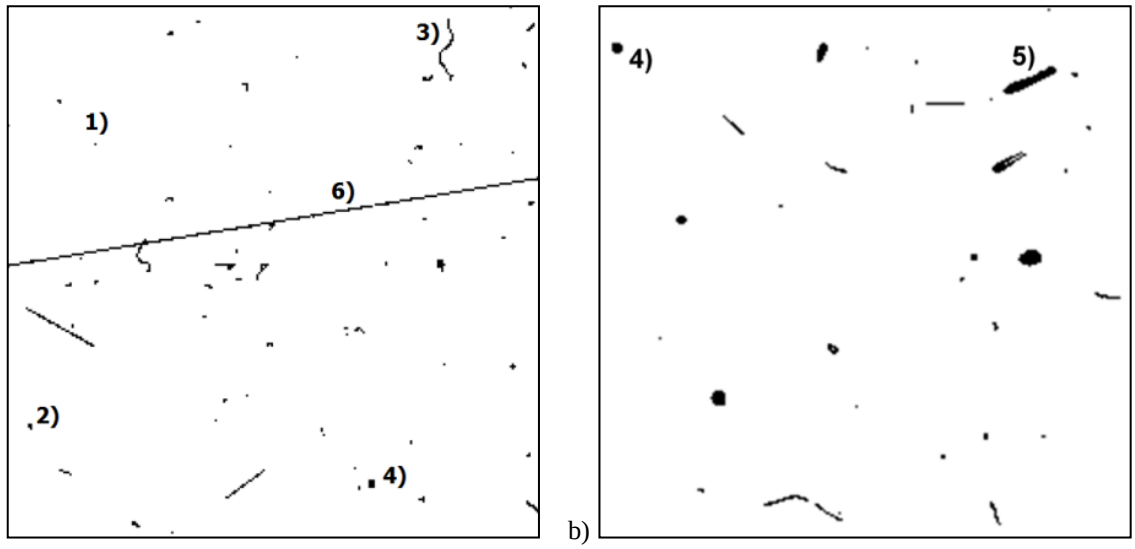

Figure 5. a) Background measurement in the ATLAS cavern in 2008 before any collision period with MPX11. The long straight track apparently corresponds to a cosmic muon which traverses the detector vertically (the detector is turned by 90^{0}) Two other muon tracks corresponding to non-parallel incidence on the sensor have smaller track lengths. Various clusters of X-ray photons, electrons (including delta-rays along the muon track) are also visible (low threshold of 10 keV, exposure time of 100 min); b) For comparison: response under fast neutron irradiation in a cyclotron beam (wide energy spectrum from 2 – 30 MeV). The characteristic comet-like clusters can be observed, following the Bragg law of energy deposition, from protons recoiled into silicon from the PE converter layer at low threshold with an exposure time of 100 µs. The inserted labels 1 to 6 describe the assignment of clusters to individual interacting quanta of radiation by means of the pattern recognition software as explained in the text.

A.1.2 Pixel-hits counting mode

In the pixel-hits counting mode (or shortly counting mode) the frames are analyzed by summing all hits registered in all pixels, separately summed for each region as well as for the full detector area. This mode is used as an analysis tool in radiation environment with high particle fluxes. When the cluster rate exceeds 10^{5} clusters.cm^{-2}.s^{-1}, overlapping of the clusters complicates the pattern recognition procedure making the hit-counting mode analysis compulsory.

At high threshold (HT) value (typically 230 – 300 keV) the low energy transfer particles (LETP – gamma and X-rays, electrons) do not contribute to the count rate (see Fig. 6). The detector records only high energy transfer particles (HETP – alpha-particles, energetic ions, hadrons) including neutrons. This HT mode can be effectively used in radiation fields with high fluxes and for neutron detection. Moreover, the use of extremely short (~μs) exposure times can be avoided. Using the adjustable pixel thresholds it would be possible to execute threshold scans and estimate in this way the LETP and HETP contributions to the radiation environment, even at high particle fluxes.

a) 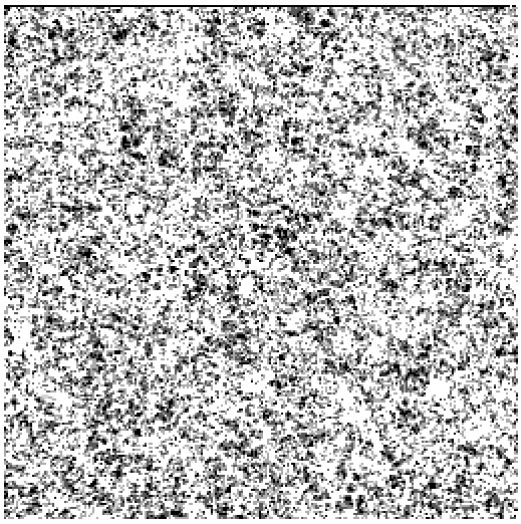 b) 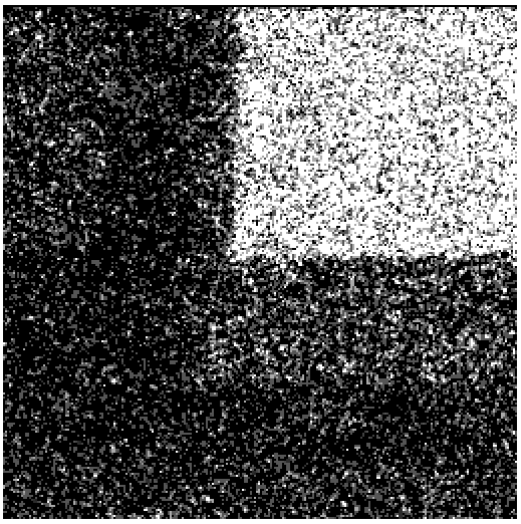

Figure 6. a) ATLAS-MPX detector, with layout as depicted in Fig. 4b, irradiated by the ^{252}Cf source at low threshold with 1 s exposure time. b) Idem at high threshold with 2000 s exposure time.

2.3 Detection efficiency of the ATLAS-MPX detectors, in particular for neutrons

The internal detection efficiency is defined as the probability that a particle which enters the detector sensitive volume generates an appropriate signal. For incident neutrons this varies typically between 0.1 and 1.4%. Device internal detection efficiencies for neutrons were determined in the following neutron fields of (see Fig. 7):

- Fast neutrons of ^{252}Cf (fission spectrum, mean energy ~2 MeV) with emission of 1×10^{8} neutrons.s^{-1}.
- Fast neutrons of ^{241}AmBe (mean energy ~4 MeV) with emission of 4×10^{7} neutrons.s^{-1}.
- Fast neutrons of Van de Graaff accelerator (14 MeV neutrons) with emission of 1×10^{7} neutrons.s^{-1}.
- Fast neutrons of cyclotron (^{6}Li target, 2 - 30 MeV neutrons) with flux of 5×10^{6} neutrons.s^{-1}.
- Thermal neutrons in a graphite prism with flux of 2.5×10^{6} neutrons.cm^{-2}.s^{-1}.

The typical internal detection efficiencies for different types of radiations (for 300 μm thick silicon sensor) are:

- 100% for charged particles with energies above 8 keV (standard low threshold value).
- About 90% for 10 keV X-rays, 2% for 60 keV X-rays, 0.5% for 662 keV gamma rays.
- About 0.1% for gamma rays with energy above 1 MeV.
- About 1% for thermal neutrons of energy below 1 eV (within the ^{6}LiF converter region)
- About 0.1% for fast neutrons of energy in the 1 – 15 MeV range (within the PE converter region).
- The detection efficiency for MIPs is 100%. However, their recognition depends on the number of hit pixels and the track length is determined by the incidence angle of the incoming MIP.

It has been proven in the calibration procedures that the detection efficiencies of installed ATLAS MPX detectors are about of the same values within 20%. The detailed description of the calibration procedure is given in Appendix B.

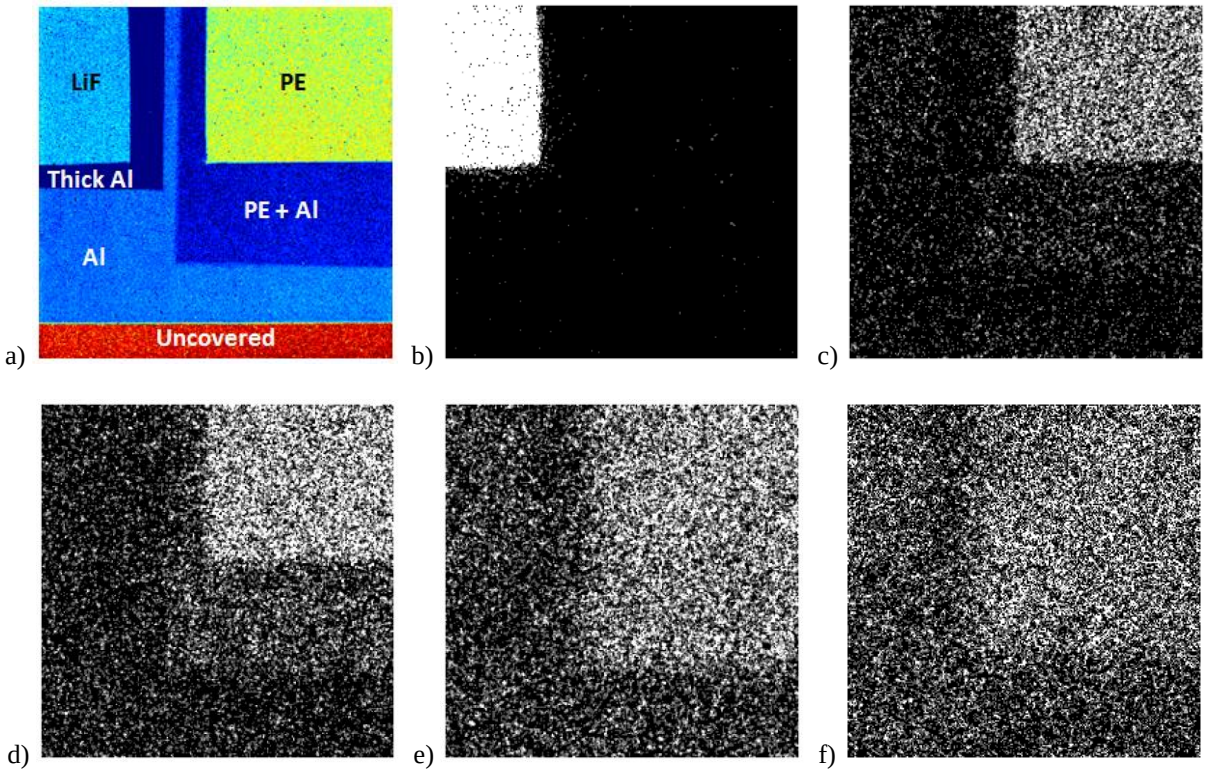

Figure 7. a) X-ray radiogram of converter layout of an MPX device. b) - f) Images of integrated responses of the MPX device set to high threshold mode (HT @ 230 keV) to, respectively b) thermal neutrons (25 meV), c) 2 MeV neutrons from ^{252}Cf, d) 4 MeV neutrons from ^{241}AmBe, e) 14 MeV neutrons from Van de Graaff accelerator and f) 2 - 30 MeV neutrons from cyclotron. Increased contribution of neutron induced reactions in silicon is easily seen with increasing neutron energy.

A.1.3 Positions and expected information from the ATLAS-MPX detectors

The ATLAS-MPX detectors are installed in UX15 experimental cavern (15 devices) and USA15 cavern (one device) in positions depicted on Fig. 8 and 9 where exact coordinates are summarized in Tab. 1:

- Two devices are between ID and JM plug in front of LAr calorimeters (one on side A and one on side C).
- Three devices are between TILECAL barrel and TILECAL External Barrel (two on side A and one on side C).
- One device is on top of TILECAL barrel and one is on top of TILECAL External Barrel, both on side A.
- Three devices are on the muon small wheel chambers (side A) and one is attached to EIL4 part of the muon spectrometer (side A).
- One device is placed within JF shielding at the back of LUCID detector close to the LHC vacuum chamber.
- Four devices are placed outside of the experiment volume where they are dedicated to the measurement of radiation environment during LHC operation. One detector sits on top of the JF shielding; two on cavern walls and the last one is in the USA15 cavern.

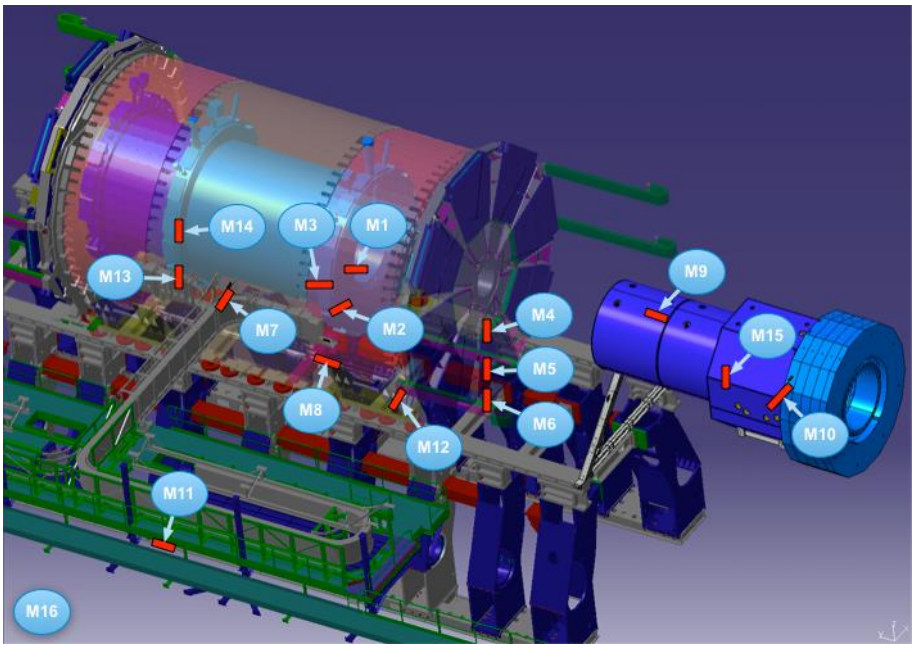

Figure 8. The network of ATLAS-MPX detectors in ATLAS. The precise detector locations are given in Tab. 1.

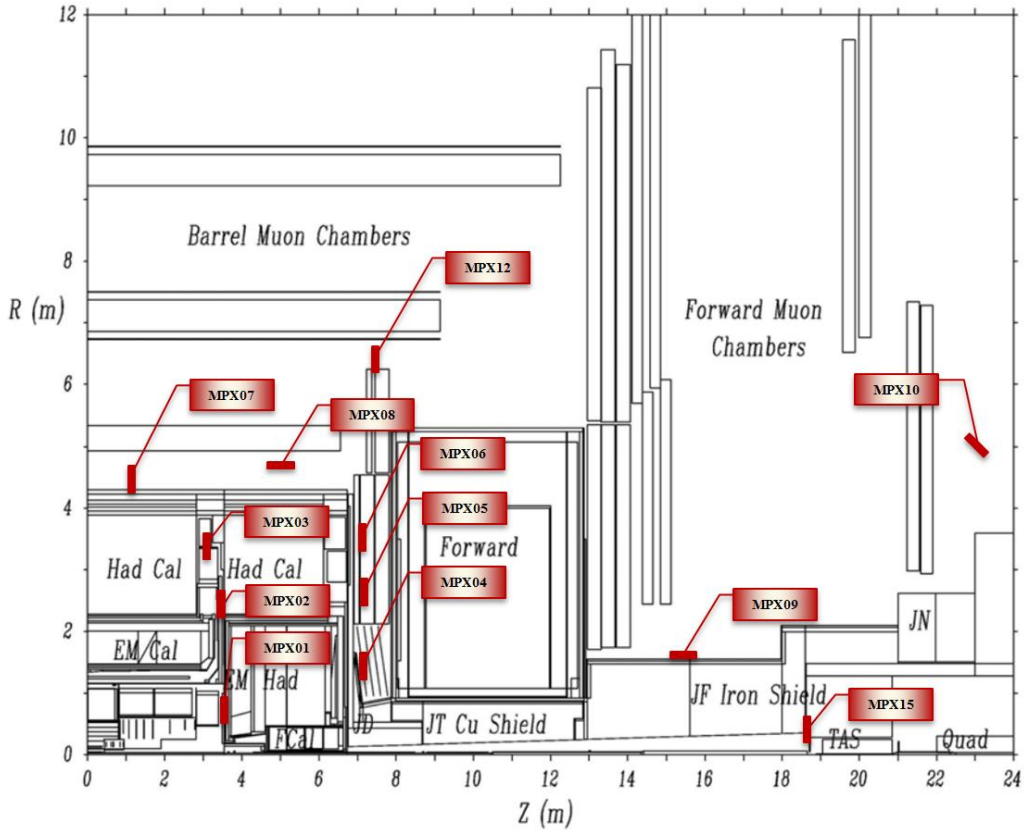

Figure 9. Locations and orientations with labels for 12 of the 16 ATLAS-MPX detectors on side A in ATLAS. MPX13 and MPX14 are placed on side C almost symmetrically to MPX01 and MPX02. MPX11 is out of R-axis range and MPX16 is located in USA15. The detectors are oriented in three different directions: Perpendicular to the beam axis (Z-axis) facing the IP: MPX01, MPX02, MPX03, MPX04, MPX05, MPX06, MPX07, MPX12, MPX13, MPX14, MPX15; parallel to the beam axis: MPX08, MPX09, MPX11, MPX16; at 45º to the beam axis: MPX10.

The ATLAS MPX detector coordinates are summarized in Tab. 1. At these positions the devices provide the real time measurement of count rates of different particle species. These measurements fulfill radiation monitoring tasks inside the ATLAS detector volume and cavern. More specifically, one task is to measure radiation fields (neutrons, X-rays, gamma rays, ions…) close to selected ATLAS sub-detectors such as forward regions of LAr calorimeter, TileCal and Muon chambers. The measurement of neutron fields can be used to estimate deterioration of electronics and detectors in positions with high radiation level. Another task is to determine the neutron contribution to the radiation field close to the JM shielding. The detectors MPX 09 and MPX 15 were placed with the specific aim to assess the effectiveness of the ATLAS neutron JF shielding. Wherever possible, the comparison of measured neutron fluxes with results of Monte Carlo simulations is also required.

The location of ATLAS-MPX detectors close to calorimeters can also serve to provide information on the composition of cascades and related particle fluxes possibly leaking out of calorimeters. Such calorimetric information is relevant for transverse energy measurements.

The correlation observed between the recorded numbers of clusters of each species measured in each ATLAS-MPX device and the LHC machine luminosity allows the ATLAS-MPX detectors to be used as a 3D-system of luminosity monitors. This is particularly true for the three ATLAS-MPX detectors, MPX01, MPX14 and MPX15 positioned close to the beam axis, which are the most sensitive. But also the other detectors positioned at lower pseudorapidity, e.g., MPX02, MPX03, MPX04, MPX13, can provide useful information. The variation in count rates measured in these detectors reflects the van der Meer luminosity scans performed in IP1.

Name	**Location description**	**X**	**Y**	**Z**	**R**	**Exposure time [s]**		
		[m]	**[m]**	**[m]**	**[m]**	**May 2010**	**Nov 2010**	**May 2011**
MPX01	between ID and JM plug	-0.71	0.29	3.42	0.77	30	1.0_{HT}	0.2_{HT}
MPX02	between TILE and EB	-2.23	-1.12	3.42	2.50	--	--	1.0
MPX03	between TILE and EB	-3.45	0.93	2.94	3.57	60	10	1.0
MPX04	on the Small Wheel	-0.65	-1.30	7.12	1.30	60	5.0	1.0
MPX05	on the Small Wheel	-0.55	-2.36	7.20	2.36	60	10	1.0
MPX06	on the Small Wheel	-0.65	-3.36	7.20	3.36	60	20	5.0
MPX07	top of TILECAL barrel	-4.53	0.79	0.35	4.59	60	200	100
MPX08	top of TILECAL EB	-4.37	-0.53	4.02	4.40	60	200	100
MPX09	on the JF cylinder	0.00	1.56	15.39	1.56	60	100	10
MPX10	cavern wall HO	-3.96	3.36	22.88	5.19	60	200	50
MPX11	cavern wall USA side	-16.69	0.05	4.86	16.69	60	200	200
MPX12	on the EIL 4	-6.25	0.00	7.23	6.25	60	100	50
MPX13	between TILE and EB, C	-2.21	-1.02	-3.42	2.44	60	1.0	0.1
MPX14	between ID and JM plug, C	-0.71	-0.30	-3.43	0.77	300_{HT}	1.0_{HT}	0.2_{HT}
MPX15	at the back of LUCID	0.19	-0.08	18.74	0.20	60_{HT}	0.1_{HT}	0.02_{HT}
MPX16	USA15	-39.48	0.90	-6.55	39.48	60	200	200

Table 1. ATLAS-MPX detector locations and positions with respect to the ATLAS interaction point IP1. Axes X, Y and Z correspond to the standard ATLAS coordinate system, $R = (X^2 + Y^2)^{1/2}$ is the distance from the beam axis at position Z). The detectors were in operation during the all beam-off LHC periods. The frame exposure times in seconds were selected for each detector according to instantaneous luminosity. Typical exposure times are given for all detectors for the running periods of May 2010, November 2010 and May 2011 as examples. Most of the devices were set to low threshold mode (LT), except MPX01, MPX14 and MPX15 which were measuring in high threshold mode (HT).

2.4 User access to ATLAS-MPX data

ATLAS user may have access to the data currently or previously recorded by the ATLAS-MPX detectors. The user accessing the ATLAS-MPX web page [8] (under Detector Operation / Infrastructure / Radiation Monitors / ATLAS-MPX) may select a particular ATLAS-MPX detector use a frame browser to visualize frames of any detector either in real time or in past periods. He also may construct histograms to visualize different cluster types or hits in pixels over a given period of time. Detailed description of the WEB user interface is given in Appendix A.

3. Operational results during the period 2008-2011

3.1 History of ATLAS-MPX operation from 2008

The network of ATLAS-MPX detectors was installed in ATLAS UX15 cavern in 2008. At that time, the network was consisting of 14 detectors. Since then, two more detectors were added to complete the present network of 16 detectors. Before any collision period, measurements of background including cosmic muon clusters were performed. These measurements allowed one to establish the ATLAS-MPX detection sensitivity to different types of radiation present in ATLAS detector environment and to test the pattern recognition algorithm that associates a particle type to a given cluster (see Fig. 5).

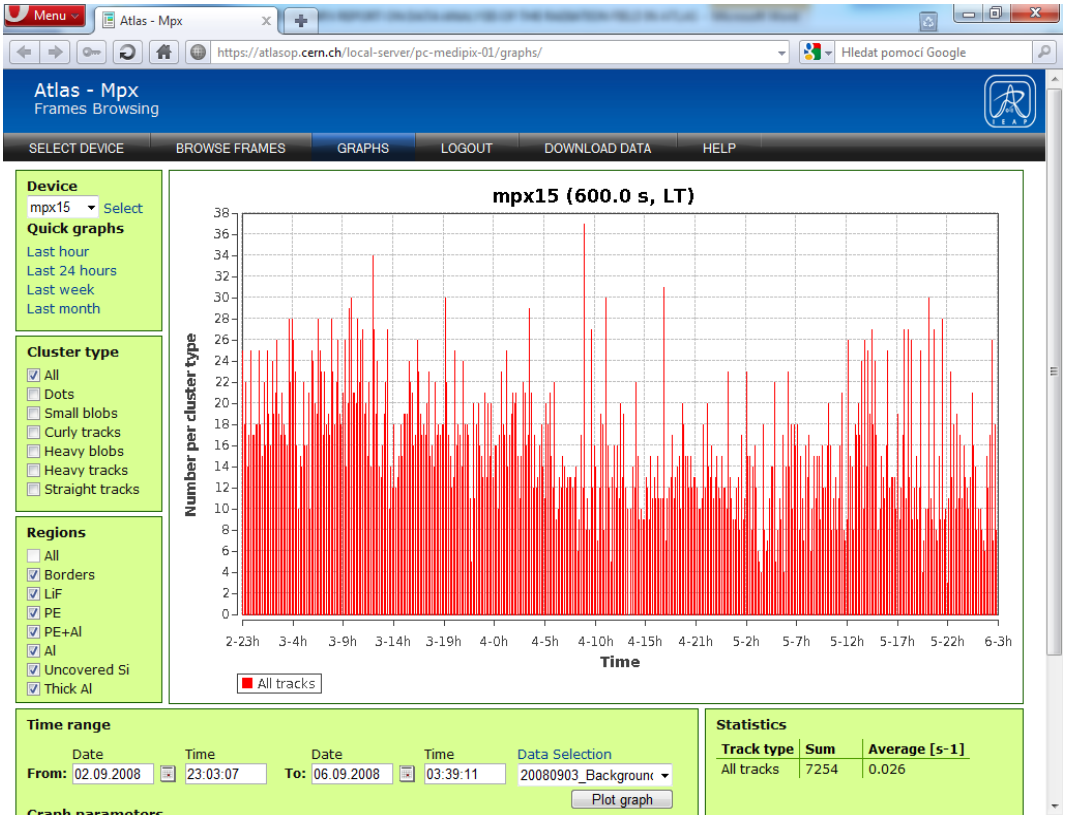

Figure 10. The background in ATLAS measured with the MPX15 detector in September 2008 before any beam collisions period (figure taken from https:// atlasop.cern.ch/local-server/pc-medipix-01/devices). The time scale is GMT.

Figure 10 shows the background measured in September 2008 with the MPX15 detector positioned close to LUCID before any beam arrival. The number of clusters per exposure (frame) is shown as a function of time. The detector was operated in tracking mode with a threshold set at 10 keV and an exposure time of 600 s. Variations in cluster counts correspond to fluctuation of natural radioactivity. The average rate of all clusters was 2.6×10^{-2} s^{-1} and the average rate of registered cosmic muons by ATLAS MPX detectors oriented vertically was about 1.0×10^{-4} s^{-1}.

3.2 First LHC beam arrivals (September 2008)

The correlation established between the recorded numbers of clusters of each species measured in each ATLAS-MPX detector and beam presence allows the direct observation with high sensitivity to any

beam manipulation including arrival, set-up and adjustment. At a given position (MPX03), it also allows the detection of radiation produced by a ^{137}Cs source used for TileCal inter-calibration measurement or X-rays used for radiography inspection in USA15 (MPX16). The first LHC beam arrival was in September 2008. The radiation level recorded by MPX15 on Wednesday 10th September 2008 is shown as a function of time in Fig. 11. The observation of clusters in MPX15 is correlated with beam arrival. The MPX15 was operated in tracking mode (low threshold of 10 keV and exposure time of 60 s). The measured average count rate for all cluster types was 0.062 s^{-1} during the period 16:30 - 17:30 GMT (Fig. 11a). This represents a counting rate twice higher than the average counting rate measured before any beam arrival. The detected number of clusters of all types measured on 10th September is shown as function of time in three inserts showing frames that correspond to no beam (background) and beam periods. The frame corresponding to this beam period shows higher number of pixel hits (Fig. 11b).

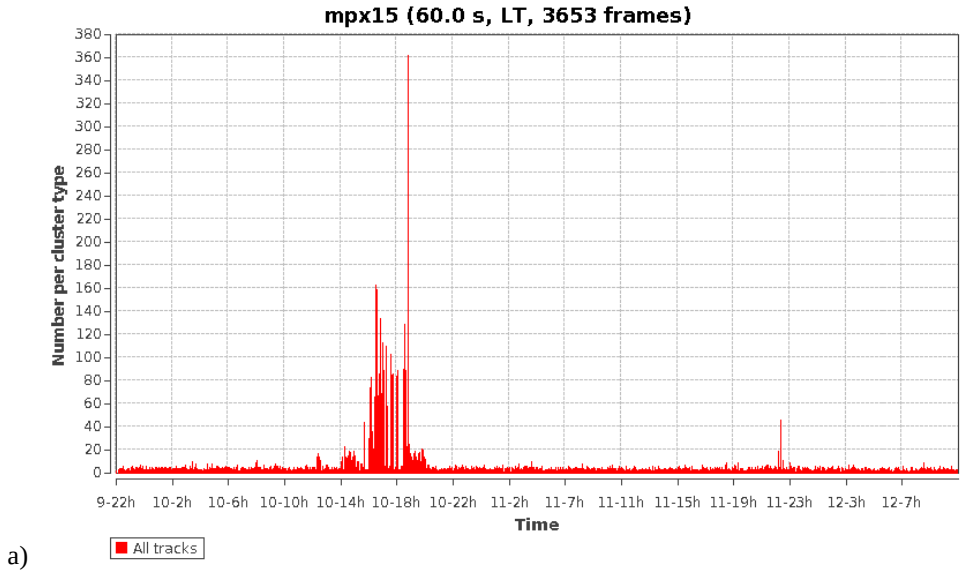

a)

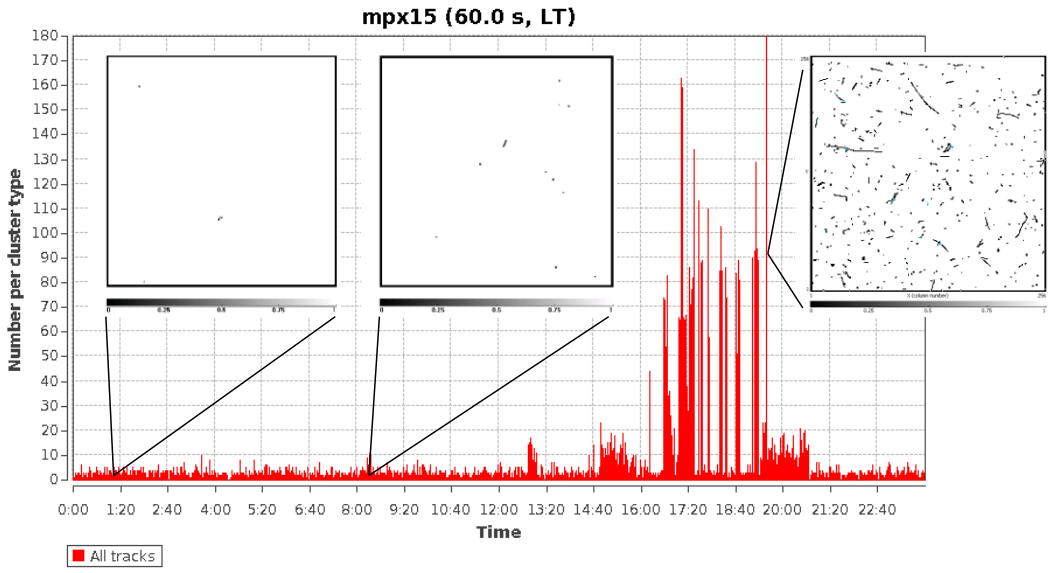

b)

Figure 11. a) The first LHC beam arrivals recorded by MPX15 between 9th and 12th September. b) Three inserts show in details frames corresponding to no beam (background) - left, a beam appearance - middle and further increased cluster rate during beam operation on 10th September 2008 (16:00 - 21:00 GMT) - right. The exposure time was 60 s. In both figures the time scale is GMT.

3.3 Restart of LHC in 2009

The LHC beam operation resumed in November 2009. Beams were brought into collision at 450 GeV per beam for the first time in the LHC on 23rd November 2009.

The correlated radiation level recorded with MPX15 during the period 21st November - 20th December 2009 is shown as a function of time in Fig. 12. The MPX15 was operated in tracking mode (low threshold of 10 keV and exposure time of 60 s). The average cluster rate for all cluster types (0.412 s^{-1}) measured during the period 12:30 - 13:30 CET on 16th December 2009 is two orders of magnitude higher as compared to the background cluster rate (2×10^{-3} s^{-1}) measured before beam arrival during the time period 10:00 - 12:10 CET on the same day.

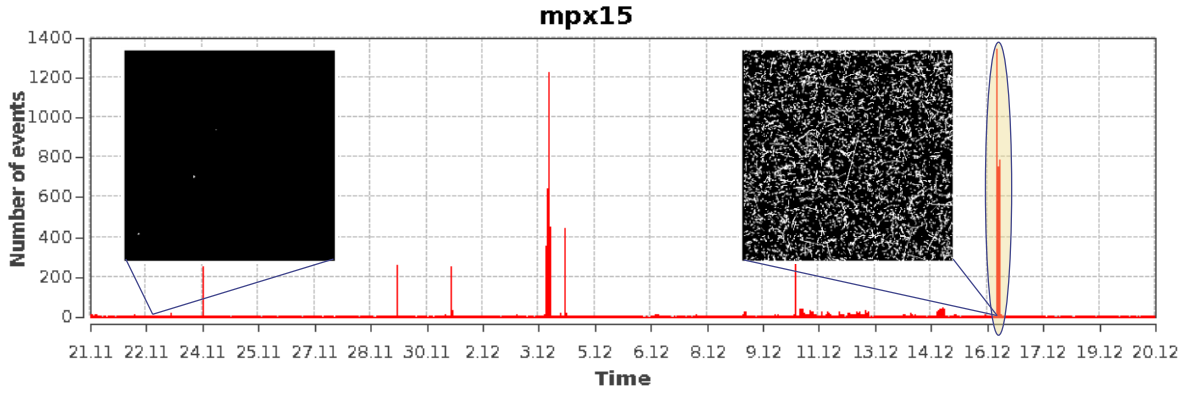

a)

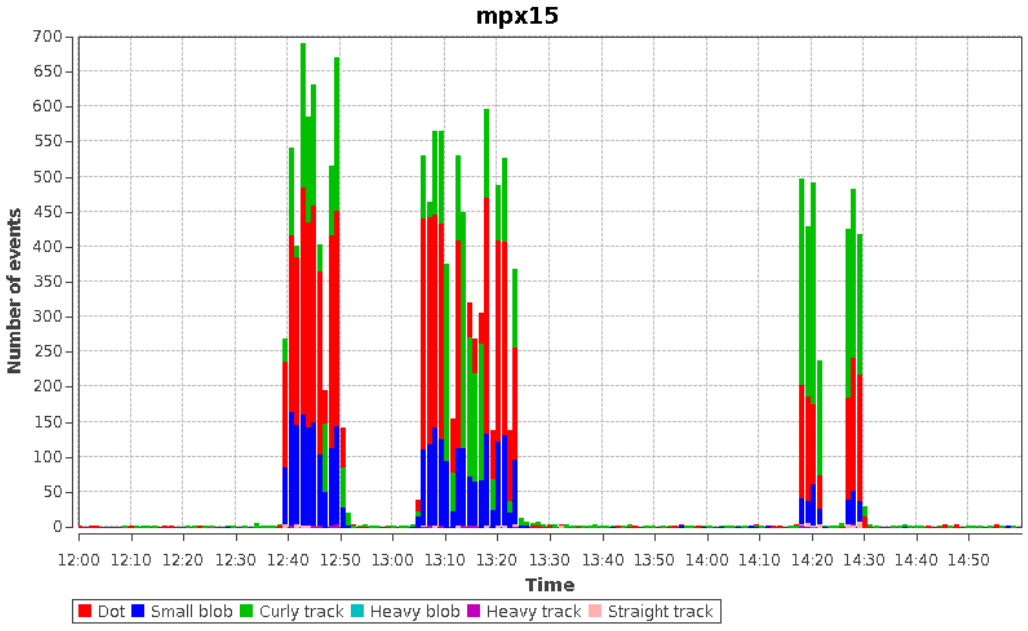

b)

Figure 12. Characterization of radiation level by means of cluster rate as recorded by MPX15 during the period 21st November - 20th December 2009 is shown as a function of time. a) Two inserts showing frames that correspond to the measured background (no beam) and beam periods. Correlation is observed between clusters measured in MPX15 and the beam arrival. b) Instantaneous count rate for different cluster types (depicted by different colors) measured during the period 12:30 - 13:30 CET on 16th December 2009 is two orders of magnitude higher compared to the measured background count rate.

3.4 Operation in 2010

The first collisions at 3.5 TeV per beam were achieved on 30th March 2010. The response of MPX15 detector is shown in Fig. 12. The detector was operated with an exposure time of 30.0 s at low threshold which allowed the observation of all radiation species at this low luminosity regime.

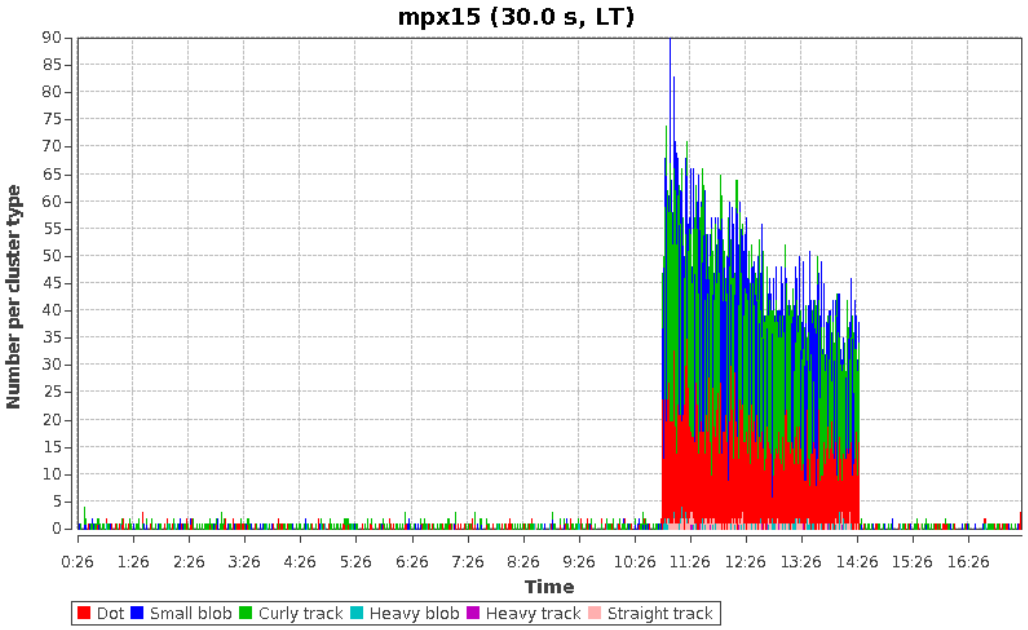

Figure 13. The first collisions at 3.5 TeV per beam on 30th March 2010 visualized with MPX15 (GMT scale).

A.1.4 ATLAS-MPX detectors network sensitivity to LHC luminosity (2010)

The sensitivity of the ATLAS-MPX detectors to any LHC activities was demonstrated in previous sections. Then, each ATLAS-MPX detector can measure in real-time at its position also the radiation field that results from any proton-proton collision occurring at the ATLAS interaction point. The detector response depends on the luminosity achieved by these collisions. The luminosity decay with time during a given run shows a decreasing exponential behavior with a lifetime defined by various sources such as the decay of the intensities of the two beams, emittance growth and possible increase of the bunch length over the duration of the run. Then, the number of clusters measured with an ATLAS-MPX detector decreases from the time of the start until the end of the run. This sensitivity of the ATLAS-MPX detectors to LHC luminosity, from low to increased value, was proven in 2010. An example of the correlation between the response of the ATLAS-MPX detectors and the LHC luminosity is shown in Fig. 14 for the October 2010 period. The 3D plot of registered clusters of all types (number of registered clusters per cm^2) compares the response for all detectors with the luminosity achieved during the successive fills in this period. Distance from beam line (R) and distance from the IP along the Z-axis (D) are giving the detectors positions. The black contours in the back plane of Fig. 14 indicate the LHC luminosity (as delivered by LHC/ATLAS luminosity monitors) during the period of October 2010 selected for display.

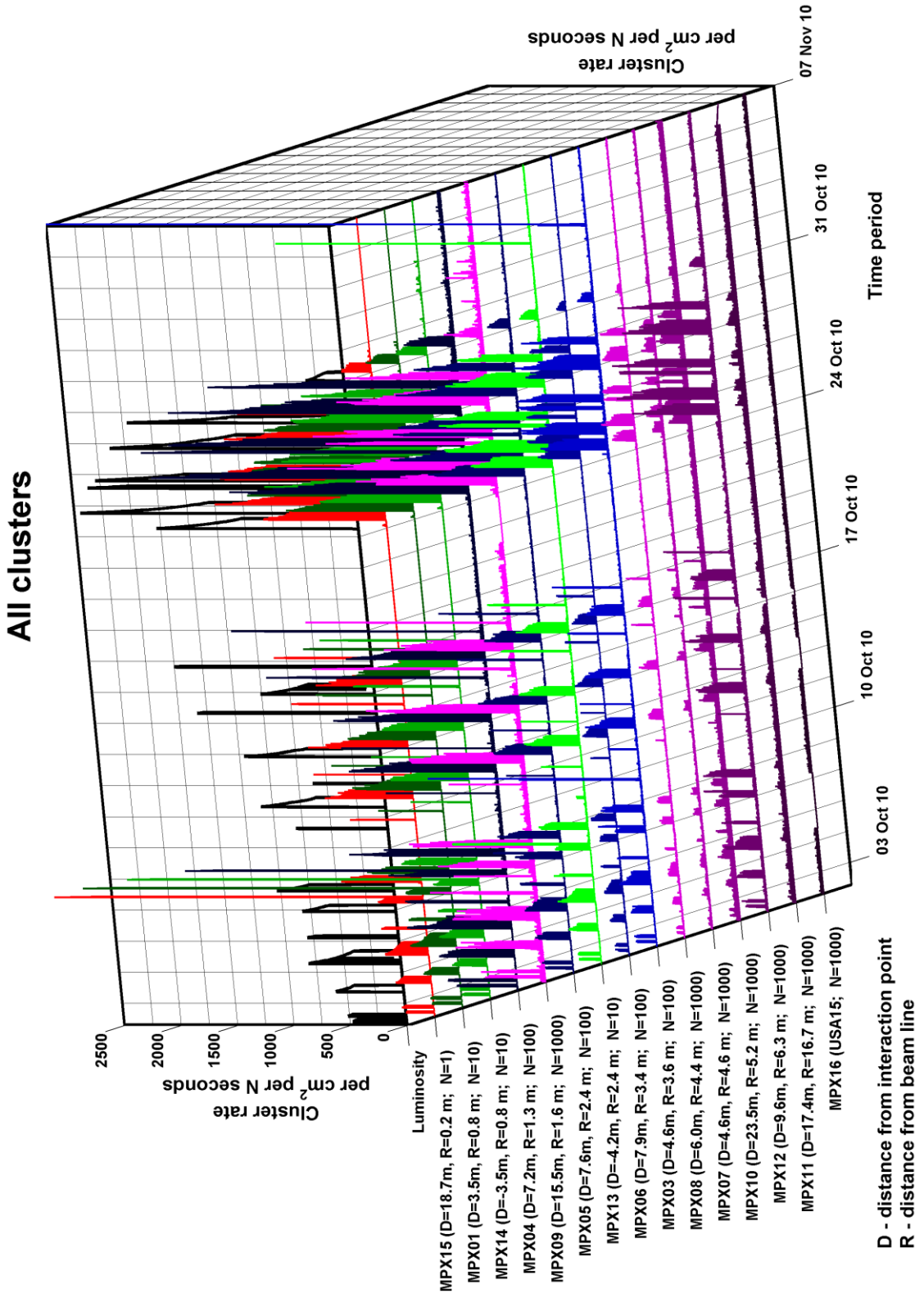

Figure 14. Data from 15 MPX detectors from 1st October to 7th November 2010, showing for each LHC fill the correlation between delivered luminosity and the responses of all ATLAS MPX detectors measuring the radiation. The y-axis shows the number of registered clusters of all types, normalized per cm^2 but scaled for different exposure times of N seconds. This scaling factor N is indicated to the left of each plane, together with the distance from the beam line R and the distance D from the IP along the Z-axis. The decrease of local flux in dependence on decrease of luminosity is clearly visible for most of the detectors. The black contours in the back plane of the figure indicate the evolution of the LHC luminosity independently measured in ATLAS.

A.1.5 Observation of Pb-Pb collisions

The example of the ATLAS MPX detector response to radiation field produced during Pb-Pb run in 2010 is depicted in Fig. 15. More detailed analysis is given in Appendix D.

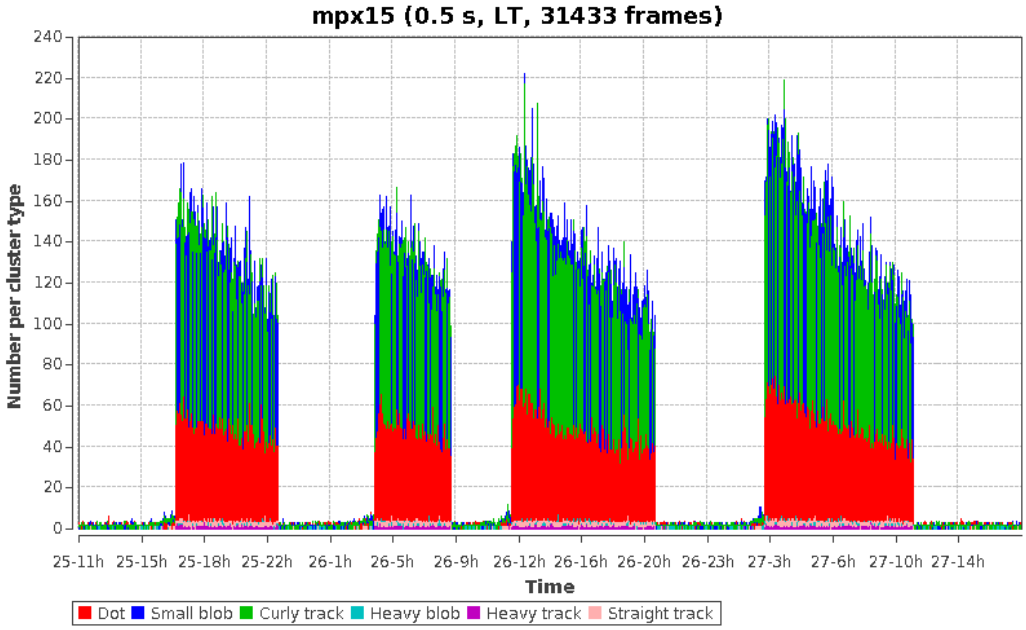

Figure 15. The MPX15 detector response as measured during the Pb-Pb run from 25th to 27th November 2010.

A.1.6 Radiation from the ^{137}Cs source used for the Tile Calorimeter inter-calibration

The MPX03 detector is positioned close to TileCal. MPX03 is sensitive to gamma ray emission of the ^{137}Cs source used for TileCal inter-calibration measurement. For example one measurement on 3rd August 2010 in absence of beam can be seen in Fig. 16.

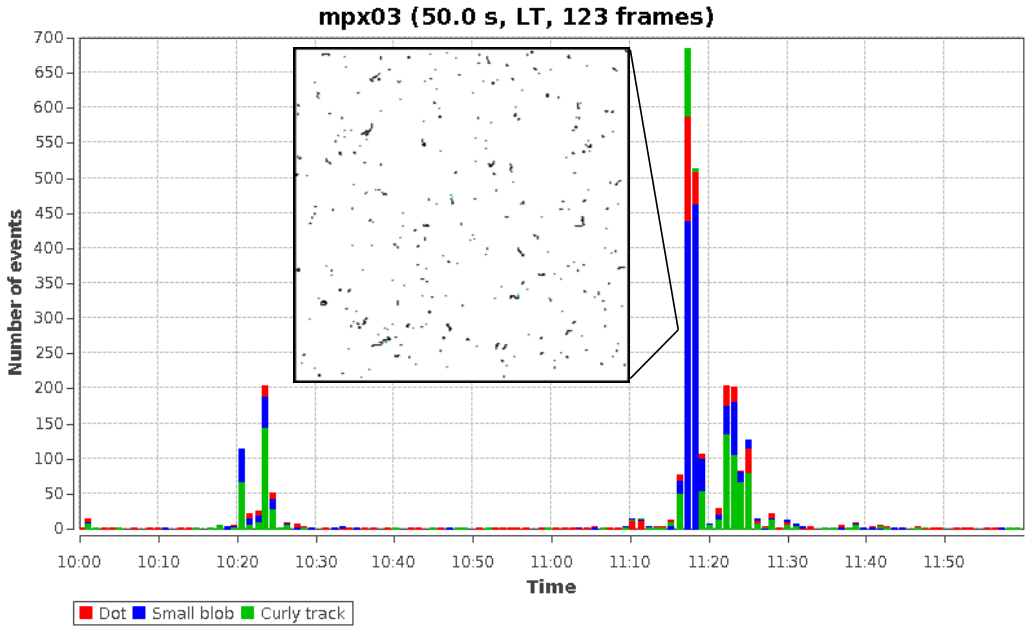

Figure 16. Sensitivity of MPX03 close to TileCal to gamma rays emitted by a ^{137}Cs source used for TileCal inter-calibration on 3rd August 2010. MPX03 was used in tracking mode (low threshold of 10 keV and exposure time of 50.0 s). The time scale is GMT.

The maximal count rate for the sum of dots and small blobs, corresponding to gamma and X-rays, was measured to be 2.055 s^{-1} and 3.128 s^{-1} during the periods 10:20 - 10:27 and 11:07 - 11:30 (GMT), respectively. These count rates represent 75% and 67% of the maximum count rate of clusters of all types (2.725 s^{-1} and 4.659 s^{-1}) measured during these two periods. These count rates are significantly higher than the background count rate (0.032 s^{-1}) measured in absence of beam, before and after the ^{137}Cs source appearances.

A.1.7 X-ray radiography in USA15 cavern

MPX16 is positioned in level 1 of USA15 cavern in rack no. Y.27-21.A1. Its sensitivity to X-rays used for radiography inspection in USA15 is demonstrated in Fig. 17. The maximum count rate for dots (3.75 s^{-1}) and small blobs (3.73 s^{-1}) corresponding to gamma and X-rays represents 92% of the maximum count rate of clusters of all types (8.12 s^{-1}) on 07th April 2010 for the period 17:30 - 19:10 GMT. These count rates are significantly higher than the background count rate (0.03 s^{-1}) measured in absence of beam, before and after this radiography inspection.

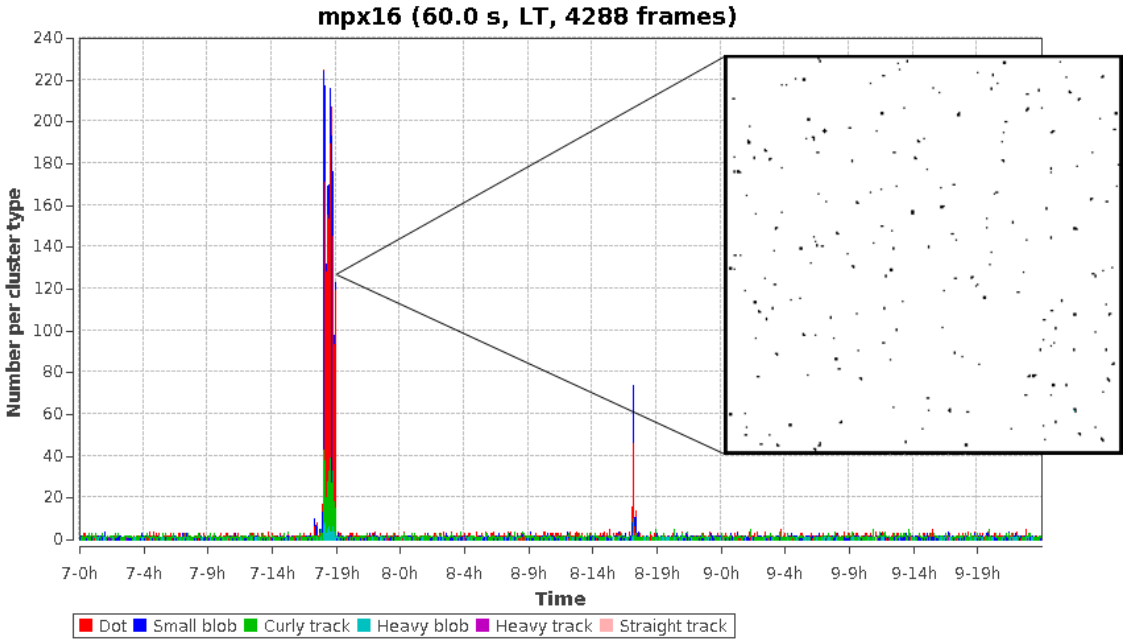

Figure 17. Sensitivity of MPX16 positioned in USA15 to X-rays used for radiography inspection in USA15 on 7th April 2010. MPX16 was used in tracking mode (low threshold of 10 keV and exposure time of 60.0 s). GMT scale.

4. Analysis of radiation fields in ATLAS and LHC luminosity in 2010 and 2011

The data from ATLAS-MPX operation in 2010 and 2011 were analyzed with the aim to understand and relate responses of all ATLAS-MPX detectors to the information on luminosity delivered by LHC.

4.1 Response of the ATLAS-MPX detectors to LHC luminosity

An example of the correlation between the response of the ATLAS-MPX detectors and the LHC luminosity is shown in Fig. 19 for the period from 21st April to 1st May 2011 and Fig. 20 for the period from 22nd May to 24th May 2011. The 3D plot of registered clusters of all types (number of registered clusters per cm^2) compares the response of all detectors with the luminosity achieved during the successive fills during these periods. As for Fig. 14, the number of registered clusters of all types is shown for each ATLAS-MPX detector whose position is given by the distance from the beam line (R) and distance from the IP along the Z-axis (D).

In the case of beam-beam collisions, one expects the ATLAS-MPX detector response to be proportional to the product of the two beam intensities resulting from bunch pairs (paired bunches) collided at the ATLAS interaction point (IP1). Then, the ATLAS-MPX detector response is a linear function of the machine integrated luminosity. Figure 18 shows the MPX03 detector response during collisions. The detector response (number of clusters.cm^{-2}) is a linear function of the integrated luminosity. The number of clusters counted with an ATLAS-MPX detector is decreasing as function of time with the rate of collisions over the duration of the run.

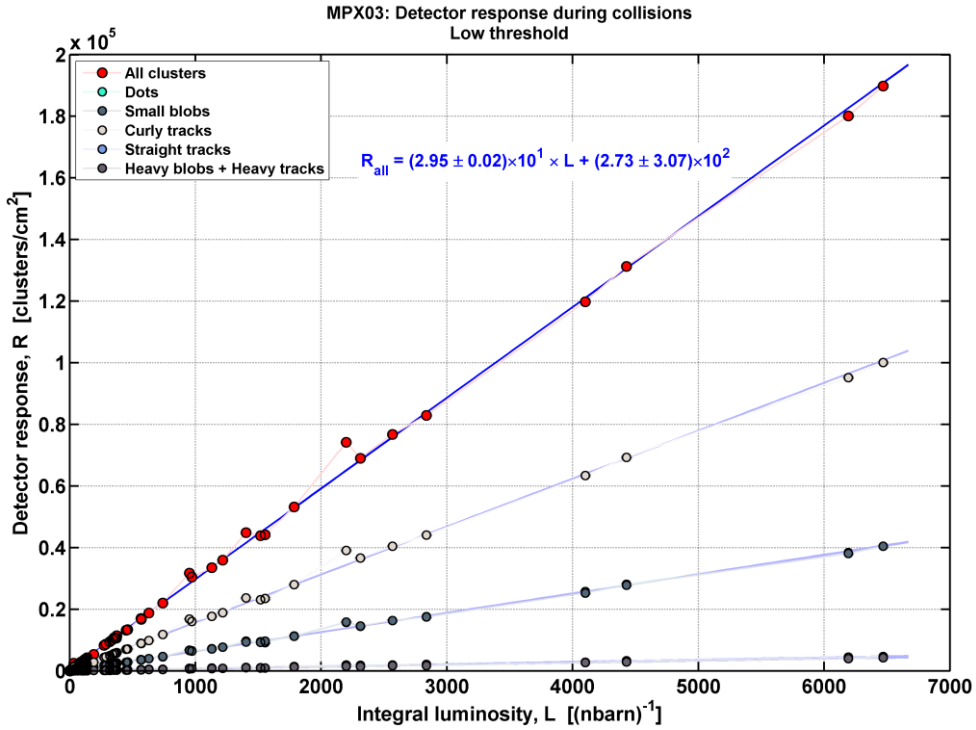

Figure 18. The MPX03 detector response recorded at low threshold (clusters.cm^{-2}) during collisions is shown as a function of the integrated luminosity (nb^{-1}). The response recorded for the various types of clusters is a linear function of the integrated luminosity over the whole available range of values.

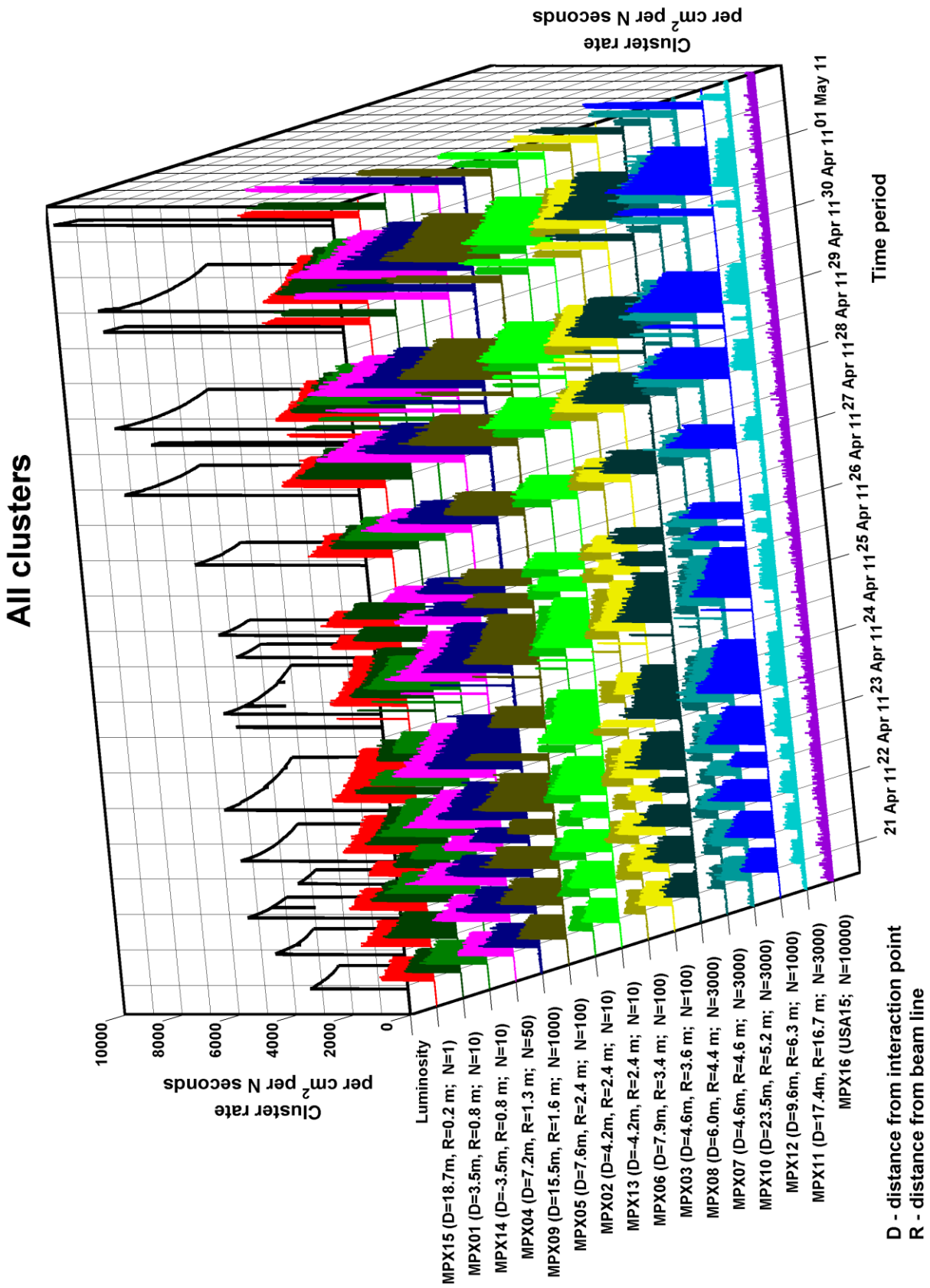

Figure 19. Data from 16 MPX detectors from 21st April – 1st May 2011, similar to Fig. 14.

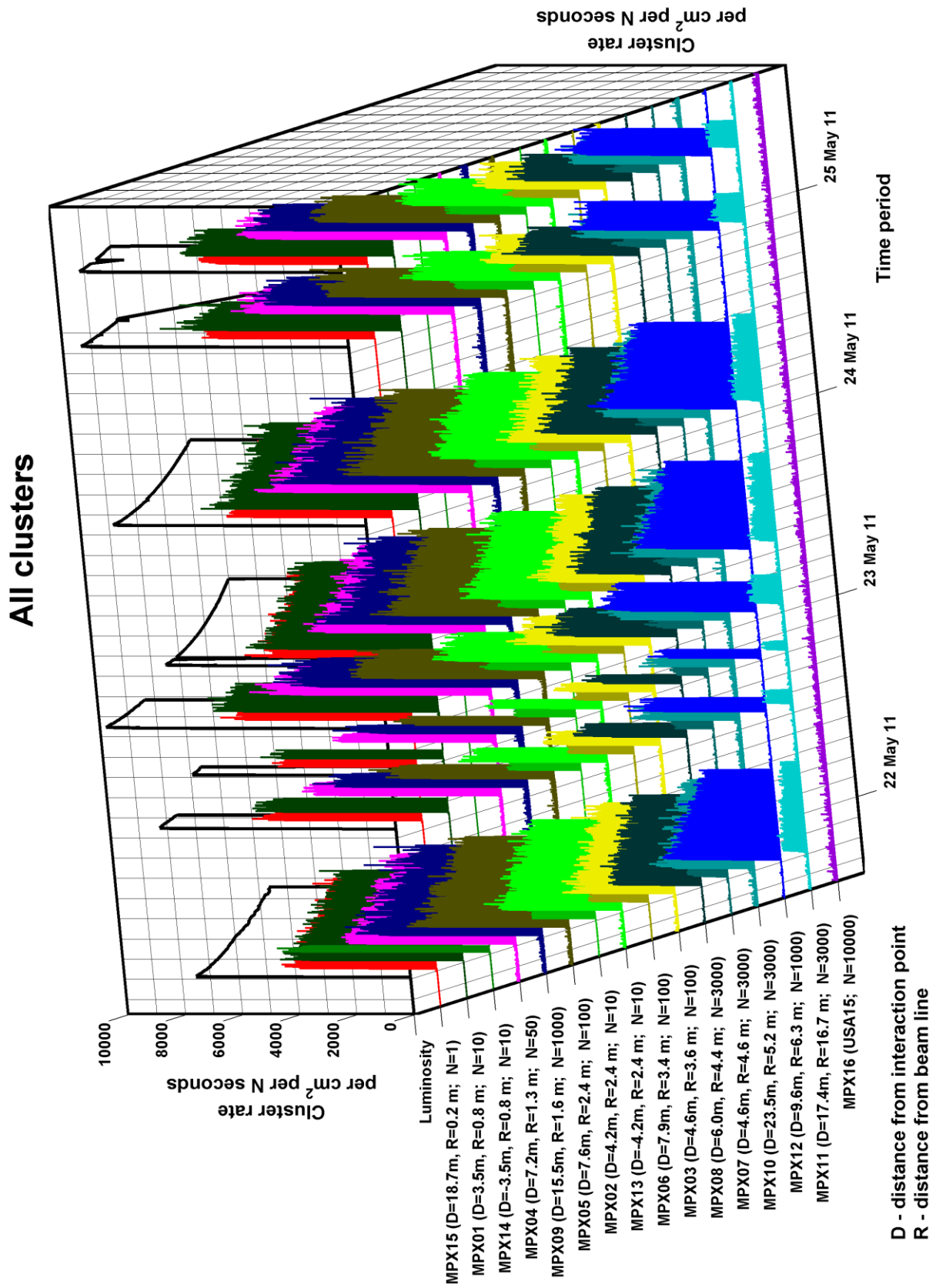

Figure 20. Data from 16 MPX detectors from 22nd May – 24th May 2011, similar to Fig. 14.

4.2 Components of radiation field in ATLAS

This subsection summarizes the evaluation of the complex radiation field in the UX15 cavern measured by ATLAS-MPX detectors. The original complex field is separated into several main radiation categories: LETP (primarily electrons), HETP (primarily protons and ions), MIPs and thermal neutrons. The figures normalized per cm^2 and fb^{-1} are calculated from the particle current measurements and summarized in Tab. 2. It is assumed that ratios of the different radiation components are preserved and the corresponding fluxes increase linearly with increasing luminosity.

The procedure of determination of measured data presented in this section is described in detail in Appendix F.

Detector	Low energy transfer particles clusters/[cm^2.fb^{-1}]	High energy transfer particles clusters/[cm^2.fb^{-1}]	MIPs clusters/[cm^2.fb^{-1}]	Thermal neutron fluence neutrons/[cm^2.fb^{-1}]
MPX01	(5.98 ± 0.01 ± 0.69) E+10	(6.68 ± 0.02 ± 1.04) E+08	(1.21 ± 0.01 ± 0.28) E+09	(3.33 ± 0.06 ± 0.58) E+10
MPX02	(2.27 ± 0.01 ± 0.19) E+08	(3.25 ± 0.01 ± 0.28) E+06	(9.61 ± 0.01 ± 0.84) E+06	(1.66 ± 0.01 ± 0.15) E+09
MPX03	(3.11 ± 0.01 ± 0.17) E+07	(4.92 ± 0.01 ± 0.30) E+05	(9.03 ± 0.01 ± 0.54) E+05	(2.45 ± 0.01 ± 0.16) E+08
MPX04	(1.16 ± 0.01 ± 0.02) E+08	(1.77 ± 0.01 ± 0.04) E+06	(1.55 ± 0.01 ± 0.07) E+06	(3.40 ± 0.01 ± 0.08) E+09
MPX05	(4.87 ± 0.01 ± 0.18) E+07	(5.23 ± 0.01 ± 0.24) E+05	(5.05 ± 0.01 ± 0.30) E+05	(6.87 ± 0.01 ± 0.27) E+08
MPX06	(2.03 ± 0.01 ± 0.07) E+07	(2.20 ± 0.01 ± 0.10) E+05	(2.30 ± 0.01 ± 0.14) E+05	(1.81 ± 0.01 ± 0.06) E+08
MPX07	(4.55 ± 0.01 ± 0.10) E+05	(4.26 ± 0.03 ± 0.32) E+03	(9.77 ± 0.05 ± 0.53) E+03	(6.02 ± 0.03 ± 0.37) E+06
MPX08	(1.22 ± 0.01 ± 0.03) E+06	(1.18 ± 0.01 ± 0.07) E+04	(1.48 ± 0.01 ± 0.09) E+04	(1.66 ± 0.01 ± 0.06) E+07
MPX09	(5.96 ± 0.01 ± 0.53) E+06	(8.95 ± 0.02 ± 0.83) E+04	(2.52 ± 0.01 ± 0.25) E+05	(2.56 ± 0.01 ± 0.19) E+07
MPX10	(1.06 ± 0.01 ± 0.02) E+06	(1.16 ± 0.01 ± 0.05) E+04	(9.11 ± 0.05 ± 0.62) E+03	(1.77 ± 0.01 ± 0.07) E+07
MPX11	(3.07 ± 0.01 ± 0.07) E+05	(6.41 ± 0.04 ± 0.38) E+03	(2.46 ± 0.03 ± 0.21) E+03	(2.82 ± 0.03 ± 0.27) E+06
MPX12	(4.04 ± 0.01 ± 0.11) E+06	(5.37 ± 0.02 ± 0.20) E+04	(5.58 ± 0.02 ± 0.31) E+04	(6.24 ± 0.01 ± 0.21) E+07
MPX13	(3.81 ± 0.01 ± 0.09) E+08	(5.38 ± 0.01 ± 0.17) E+06	(1.47 ± 0.01 ± 0.04) E+07	(2.75 ± 0.01 ± 0.11) E+09
MPX14	(5.61 ± 0.01 ± 0.65) E+10	(6.17 ± 0.02 ± 0.81) E+08	(1.03 ± 0.01 ± 0.16) E+09	(2.93 ± 0.04 ± 0.86) E+10
MPX15	(2.59 ± 0.01 ± 0.33) E+12	(1.20 ± 0.01 ± 0.26) E+10	(1.57 ± 0.01 ± 0.34) E+10	(1.85 ± 0.13 ± 0.58) E+10
MPX16	(6.99 ± 0.03 ± 2.94) E+02	(9.02 ± 0.23 ± 3.78) E+01	(3.54 ± 0.20 ± 1.46) E+01	(1.12 ± 3.73 ± 0.67) E+04

Table 2. Radiation exposure of ATLAS-MPX devices normalized to fb^{-1}. Low energy transfer particles represent primarily electrons, high energy transfer particles represent primarily protons and ions. The mean values are stated together with their statistical and overall uncertainties, respectively. The statistical uncertainty is based on the total number of detected clusters only. The value of 0.01 in brackets usually corresponds to even much lower statistical uncertainty. However, due to the expression of mean value to 3 significant digits, the statistical uncertainty had to be rounded to 0.01. The overall uncertainty expresses the dispersion of the individual cluster rates per unit luminosity calculated for each collision period around the mean and it is calculated according to a procedure described in Appendix F.

4.3 p-p van der Meer luminosity scan results

The luminosity of a hadron collider can be determined from measured colliding beam parameters [9] and expressed as:

$$\mathcal{L} = n_b n_1 n_2 \mathcal{L}_{spec} \tag{1}$$

where

$$\mathcal{L}_{spec} = \frac{f_r}{2\pi \Sigma_x \Sigma_y} \tag{2}$$

is the specific luminosity. n_b is the number of bunches per beam, f_r is the machine revolution frequency (~11 kHz), n_1 and n_2 are the bunch populations (number of protons) in beam 1 and beam 2, respectively, and Σ_x and Σ_y are the effective widths of the horizontal and vertical profiles of the colliding beams, respectively. Measurement of these effective widths is done by recording the relative interaction rates as function of the transverse beam separation using the van der Meer luminosity scan method. At LHC, the scans are performed, at a given interaction point, by moving the beams step-wise with respect to each other in the two transverse planes, first in horizontal (x) and, then, in the vertical (y) direction. In practice, the two beams are moved simultaneously in opposite directions by $\pm 3\,\sigma_b$ (the nominal beam diameter) representing a total scan range of $\pm 6\,\sigma_b$ at the IP [9]. The total number of scan steps per plane was 27 for fills 1059 and 1089 in 2010 and 25 for fill 1783 in 2011. The time measurement at each step position is 30 s usually, but may vary with different luminosity scan. The interaction rates measured as function of the beam separation during the set of scans done in both transverse planes yield two bell-shaped curves with the maximum rate at zero beam separation. Double Gaussian or a single Gaussian with a constant background can be used to fit the count rates of clusters recorded during the luminosity horizontal and vertical scans. Application of either fit procedure, gives the value of the effective horizontal, Σ_x and vertical, Σ_y profiles of the colliding beams as well as the maximum achievable collision rate.

An ATLAS-MPX detector can measure instantaneously at its position the radiation field produced by a collision at the ATLAS interaction point. Such a correlation gives to the ATLAS-MPX detectors the capability of bringing real-time information on any beam movement. In particular, ATLAS-MPX detectors positioned close to the beam axis, namely MPX01, MPX14 and MPX15, can directly visualize luminosity scans performed according to the van der Meer beam displacement method and permit an evaluation of the effective overlapping beam sizes and maximum collision rate. Figure 21 shows, as a function of time, the clusters recorded with the MPX15 detector during luminosity scans done during fills 1059 (26th April 2010) and 1089 (9th May 2010), respectively. For both fills, MPX15 was set at low threshold (10 keV) and measurements were performed in tracking mode with exposure times of 30.0 s and 10.0 s for fill 1059 and 1089, respectively. In Fig. 21a, one can observe a horizontal scan followed by a vertical scan done during fill 1059. Figure 21b shows two horizontal scans followed by two vertical scans done during fill 1089.

a)

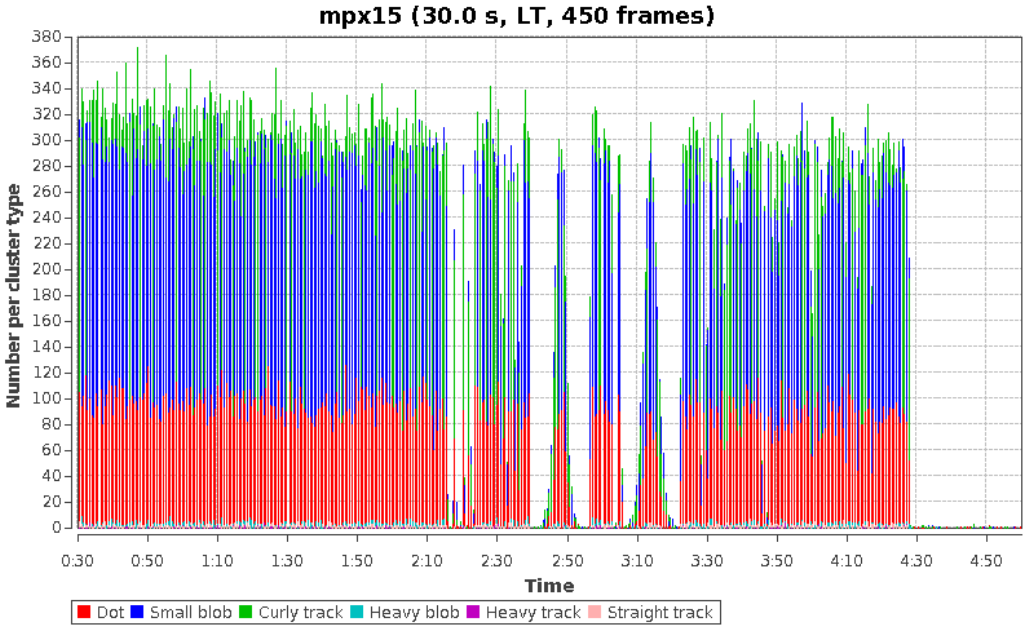

b)

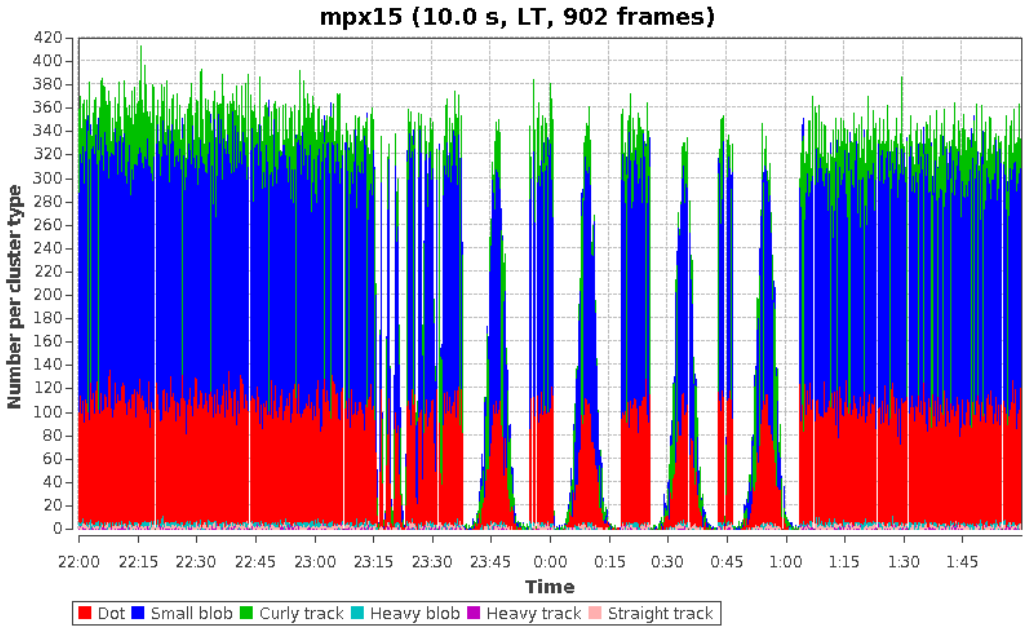

Figure 21. Van der Meer scans as observed with MPX15 with threshold set at 10 keV. a) A horizontal scan followed by a vertical scan during fill 1059 on 26th April 2010 (GMT) with MPX15 and exposure of 30.0 s. b) Two horizontal scans followed by two vertical scans during fill 1089 on 9th May 2010 (GMT) with MPX15 and frame time of 10.0 s. Different colors represents the different cluster types as described on Fig. 5.

With the continuing increase of the number of bunches, the ATLAS-MPX detectors exposure time had to be shortened in order to obtain tracking mode data of good quality (i.e., to avoid cluster overlap). This leads to very short exposure time and large dead time. That is why the MPX15 detector was set to low threshold mode with 10 s exposure time during the van der Meer luminosity scan on 15th May 2011. Instead of cluster rate, the count rate in counting mode was used for evaluation of the measured data. As depicted in Fig. 22, high counting rates with very good statistics were obtained resulting in Gaussian fits with low uncertainty ($R^2 > 0.994$ for all four scans; see Fig. 23b).

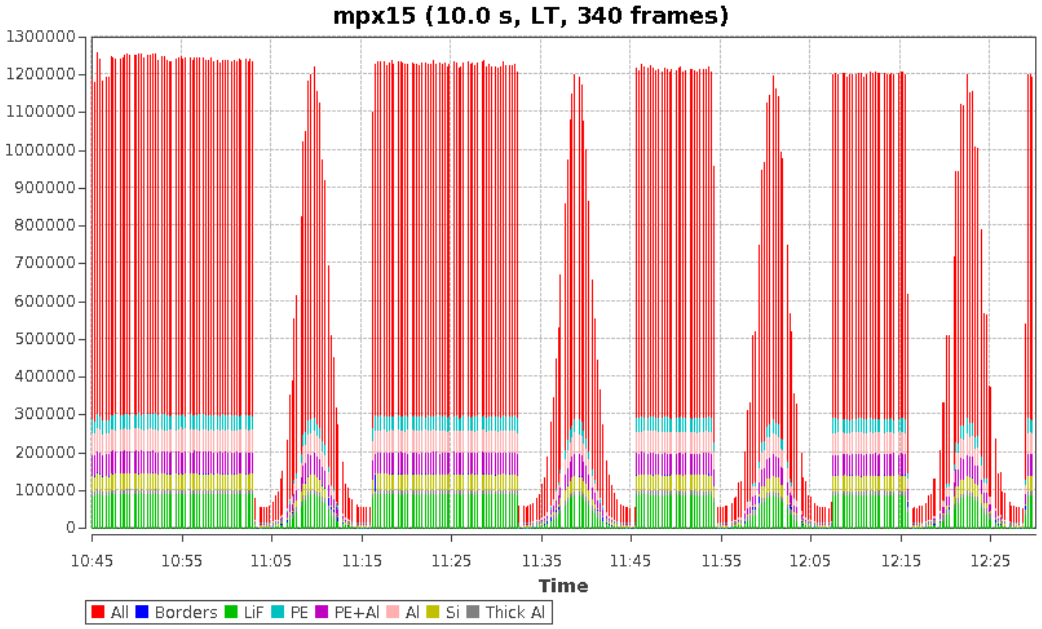

Figure 22. Van der Meer scans as observed with the detector MPX15 running in counting mode during fill 1783. The scans were done on 15th May 2011. Two horizontal and two vertical scans are visualized. The detector threshold was set at 10 keV and measurements were performed with an exposure time of 10.0 s. Different colors represent the response of the different detector regions (see Fig. 4).

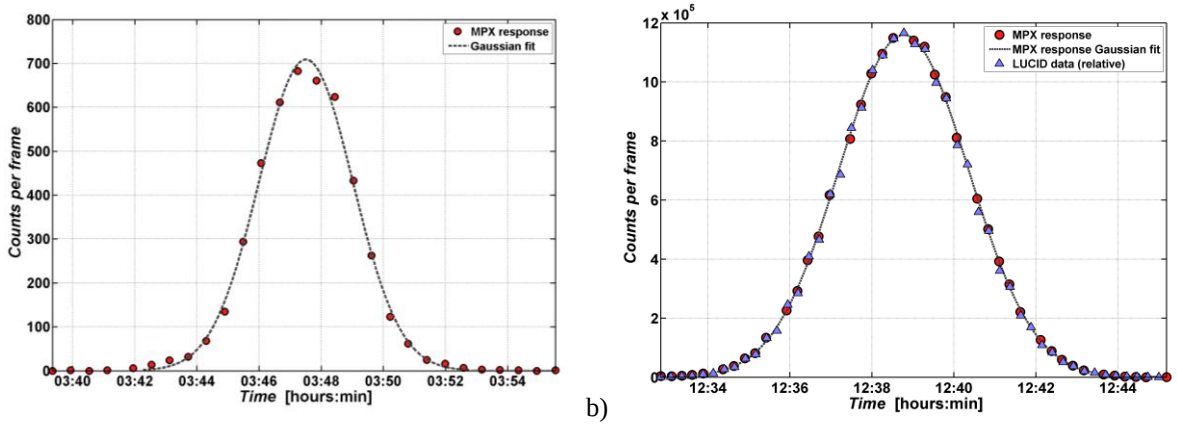

a) b)

Figure 23. Gaussian curve fitted to the count rates measured with MPX15 as function of time a) during the first horizontal van der Meer scan of fill 1059 (26th April 2010) and b) during the first vertical van der Meer scan of fill 1783 (15th May 2011). Scaled LUCID readings (blue triangles) are compared to MPX15 data (red circles).

After evaluation of fill 1783 scan data, it was decided that during future van der Meer scans, two of the ATLAS-MPX devices closest to the interaction point (MPX01) and beam pipe (MPX15) will be temporarily set to low threshold mode with longer exposure time and the measured data will be evaluated in the counting mode regime.

The ATLAS-MPX detectors are recording cluster rates continuously during the van der Meer transverse scans. The cluster rates measured during these scans as a function of time appear as bell-shaped curves with their maximum achieved at a time corresponding to zero beam separation. Frames being collected continuously, one can obtain several frames per one van der Meer step (short exposure time) or one frame per more van der Meer steps (long exposure time).

Then, for all ATLAS-MPX detectors considered, a Gaussian with a constant background was used to fit the cluster rates recorded during the horizontal and vertical luminosity scans. Application of

the fit procedure, gives the value of the effective horizontal (σ_x) and vertical (σ_y) profiles of the overlapping beams in units of seconds (Fig. 23). As the van der Meer luminosity scans method is measuring interaction rates as function of the beam separation (expressed in microns), the σ_x and σ_y measurements have to be translated from time units (seconds) into length units (micrometers) expressing beam separation. To do this conversion, one needs to use the scan step length and the dead time interval between steps. While the scan step length is taken from available information on ATLAS luminosity, the mean dead time interval between steps had to be calculated using the knowledge of the total scan duration. This value was found from MPX15 measurement and also independently checked using LUCID luminosity data.

Total van der Meer scan time (performed on 9th May 2010) is obtained from LUCID and MPX15 luminosity scan data (fill 1089, first vertical scan) and the mean dead time interval t_D between scan steps as calculated from Eq. (3) below:

- Total scan duration of (1015 ± 16) s (first vertical scan), LUCID data (fill 1089) - The LUCID scan length was determined from LUCID data which were measured in 20 s intervals. The uncertainty is estimated as two times the one fourth of the length of one LUCID reading (uncertainty in estimation of exact start and end of the scan).
- Total scan duration of (1016 ± 12) s (first vertical scan), MPX15 data (fill 1089) - The MPX15 scan length was determined as the time between the beginning of the first frame with background signal only and the end of the last frame with background signal only, increased by two time intervals necessary for frame download (2 × 6 s). Uncertainty is then estimated as the total length of these two time intervals. The exposure time was 10 s. Mean "dead time" interval (t_D) between scan steps was 10.25 s.

No detailed data on exact scan timing were available therefore only the mean value of the dead time interval between scan steps could be determined from the equation

$$t_D = \frac{(T_{LUCID} - N.t)}{N+1} \tag{3}$$

where t_D is the mean dead time interval between scan steps, T_{LUCID} is the total scan time determined from LUCID data, N is the number of scan steps, t is the nominal time of one scan step. For scans done during fills 1059 and 1089 t_D = 10.25 s for T_{LUCID} = 1015 s, N = (27 - 2) = 25 and t = 30 s [9]. N + 1 in the denominator corresponds to the assumption that the total scan time T_{LUCID} begins and ends with the dead time interval. Then, the effective horizontal (Σ_x) and vertical (Σ_y) profiles of the colliding beams expressed in microns can be calculated using the formula

$$\Sigma = \sigma.\frac{\Delta.\sigma_b}{N.(t+t_D)} \tag{4}$$

where Σ is the effective width of the horizontal or vertical profile of the colliding beams expressed in micrometers, σ is the sigma parameter of the Gaussian fit to the MPX data expressed in seconds, Δ is the range of the whole van der Meer scan in units of σ_b (Δ = 12) with the nominal beam diameter σ_b = 45 μm for fills 1059 and 1089 [9] or σ_b = 40 μm for fill 1783 scans.

The procedure followed for the calculation of the scan step length and the dead time interval between steps for the luminosity scan data of fill 1089, was also applied for the data of fill 1059 (on 26th April 2010) and 1783 (on 15th May 2011). The results obtained for Σ_x and Σ_y from fitting a Gaussian to MPX15, MPX01 and MPX14 van der Meer scans data recorded during fills 1059, 1089 and 1783 are summarized in Tab. 3.

MPX detector	Date	Fill	Scan direction*	Scan number	Σ_x or Σ_y [μm]	Uncertainty σ [μm]	Gaussian fit R^2
MPX15	26th April 2010	1059	H	1	48.63	0.65	0.997
MPX15	26th April 2010	1059	V	1	59.82	0.75	0.997
MPX01	9th May 2010	1089	H	2	60.61	1.69	0.994
MPX14	9th May 2010	1089	H	2	61.70	1.94	0.992
MPX15	9th May 2010	1089	H	2	62.07	0.76	0.993
MPX15	9th May 2010	1089	H	3	61.31	0.88	0.990
MPX15	9th May 2010	1089	V	2	65.28	0.81	0.992
MPX15	9th May 2010	1089	V	3	64.66	0.82	0.993
MPX15	15th May 2011	1783	H	1	55.14	0.61	0.9978°
MPX15	15th May 2011	1783	V	1	56.84	0.24	0.9997°
MPX15	15th May 2011	1783	H	2	55.83	0.73	0.9966°
MPX15	15th May 2011	1783	V	2	57.05	1.00	0.9941°

*H = horizontal, V = vertical

°Fits obtained from counting mode data (see text).

Table 3. Σ_x and Σ_y obtained from fitting a Gaussian (with a constant background) to MPX15, MPX01 and MPX14 van der Meer scans data recorded during fills 1059, 1089 and 1783.

Very good agreement of measured Σ_x or Σ_y values with the values reported in [9] and [10] was obtained and are presented in Tab. 3. The eventual difference can be caused by the inaccurate estimation of beam step lengths and dead time interval, as well as insufficient measurement statistics or, in some cases, detector response saturation in tracking mode regime. There is an on-going effort to eliminate these uncertainties in the analysis of future van der Meer scans data.

5. Activation of the environment - decay, gamma signature, dose rate

The high rate head-on collisions of protons at high luminosity at the LHC yield large multiplicities of secondary particles such as pions, kaons and protons. The interactions of primary and secondary particles with materials in the ATLAS environment produce large amounts of neutrons and material activation, including detectors and their electronics. The size and effective duration of the generated activation depends on incident fluxes and the activation cross sections, radionuclides half-life and their decay branching ratios, mainly gamma ray emissions. The activation of material parts also depends on their geometry and location within the ATLAS environment, on their content and types of nuclei. The activation is expected to grow with machine luminosity and duration of machine operation.

The ATLAS-MPX detectors become themselves activated as the result of the interaction of particles with the silicon layer, materials of microelectronics readout and duralumin box of the ATLAS-MPX detectors. Evaluation of the activation of a given ATLAS-MPX detector requires the precise knowledge of its material composition, which is unknown at present, and spectral flux distributions (high energy hadrons and neutrons) calculated using Monte Carlo transport code such as Fluka and GCalor.

ATLAS-MPX detectors self-activation is under experimental investigation (CNGS[3], nuclear reactor). In the case of "inner" devices where ATLAS-MPX devices are surrounded by a large amount of material, the self-activation contribution is negligible. The self-activation will be measured during LHC shutdown when there will be possibility to remove some devices from the UX15 cavern.

Due to their sensitivity to electrons and gamma rays, ATLAS-MPX detectors can measure radioactive decays. Activation is observed at the end of fills with most of ATLAS-MPX detectors.

Figure 24a shows the measured cluster counts (number of clusters per one exposure) of different cluster types as measured with the MPX04 detector between 20th April 2011 and 6th May 2011. Figure 24b shows the detail of Fig. 24a. Both exponential increase of a long decay component of induced activity due to the first fill and decrease after the last fill (highlighted with a black curve in Fig. 24b) of the selected period is clearly visible.

[3] CERN Neutrinos to Gran Sasso

a)

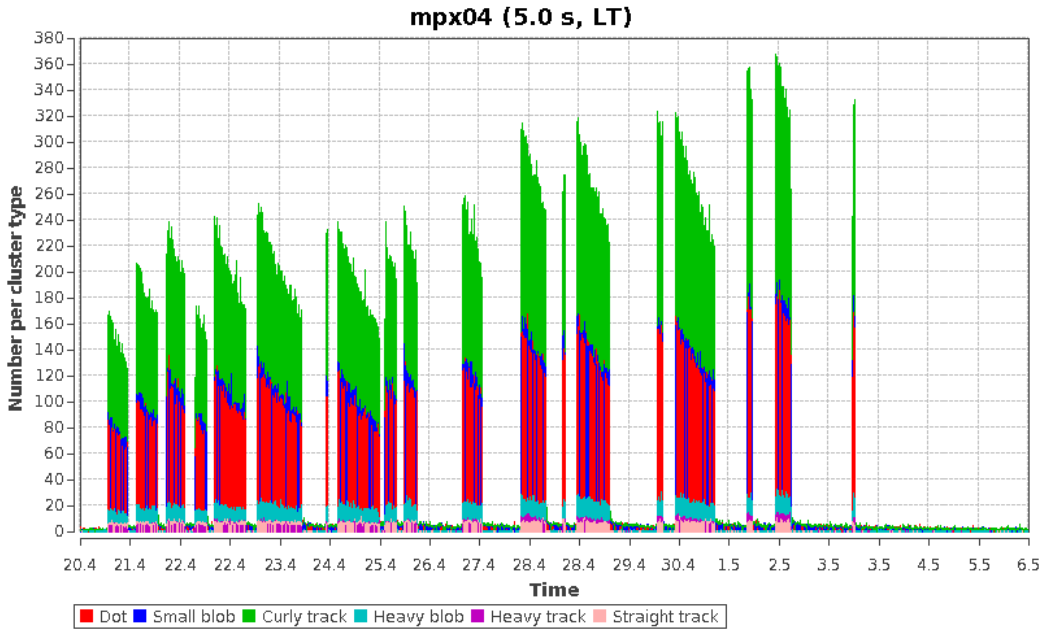

b)

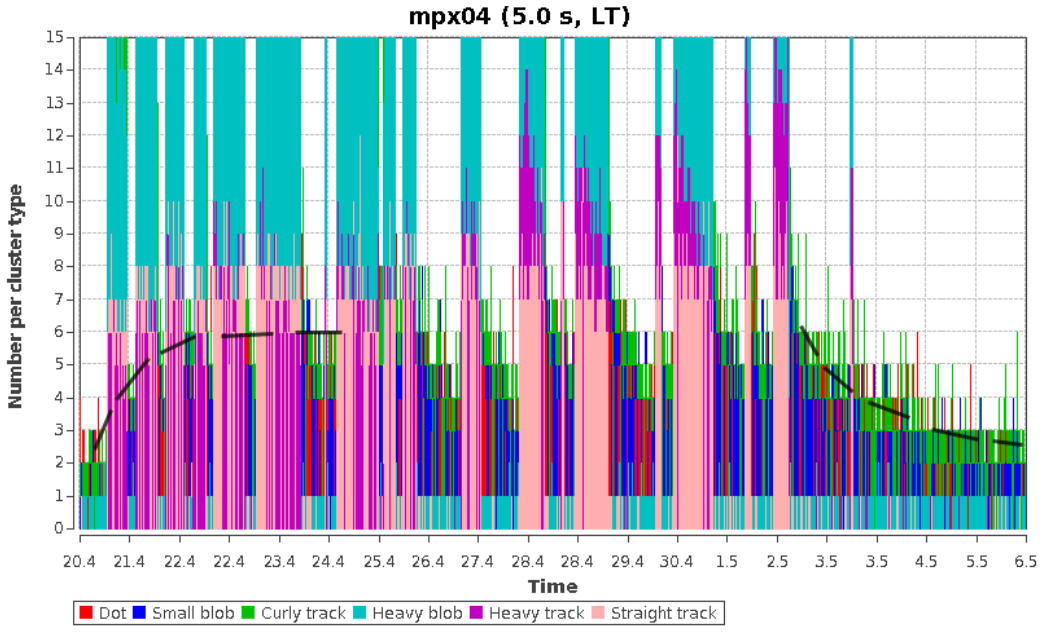

Figure 24. a) Cluster counts of different cluster types as measured with MPX04 between 20th April and 6th May 2011. b) Detail of the previous figure. The exponential increase of induced activity of the long decay component due to the first fills and decrease after the last fills are clearly visible (highlighted by dashed black curves).

The detailed composition of the measured cluster counts of the different cluster types measured with MPX04 is shown in Fig. 25 for seven runs done during the period from 27th May 2011 (12:00) to 31st May 2011 (00:00). From this figure, it is observed that the signal measured in between beam collision periods is caused only by electrons and photons as only 89 heavy blobs, 2 heavy tracks and 7 straight tracks were observed per 6270 seconds of measurement (6270 frames) compared to a total of 9500 dots, small blobs and curly tracks.

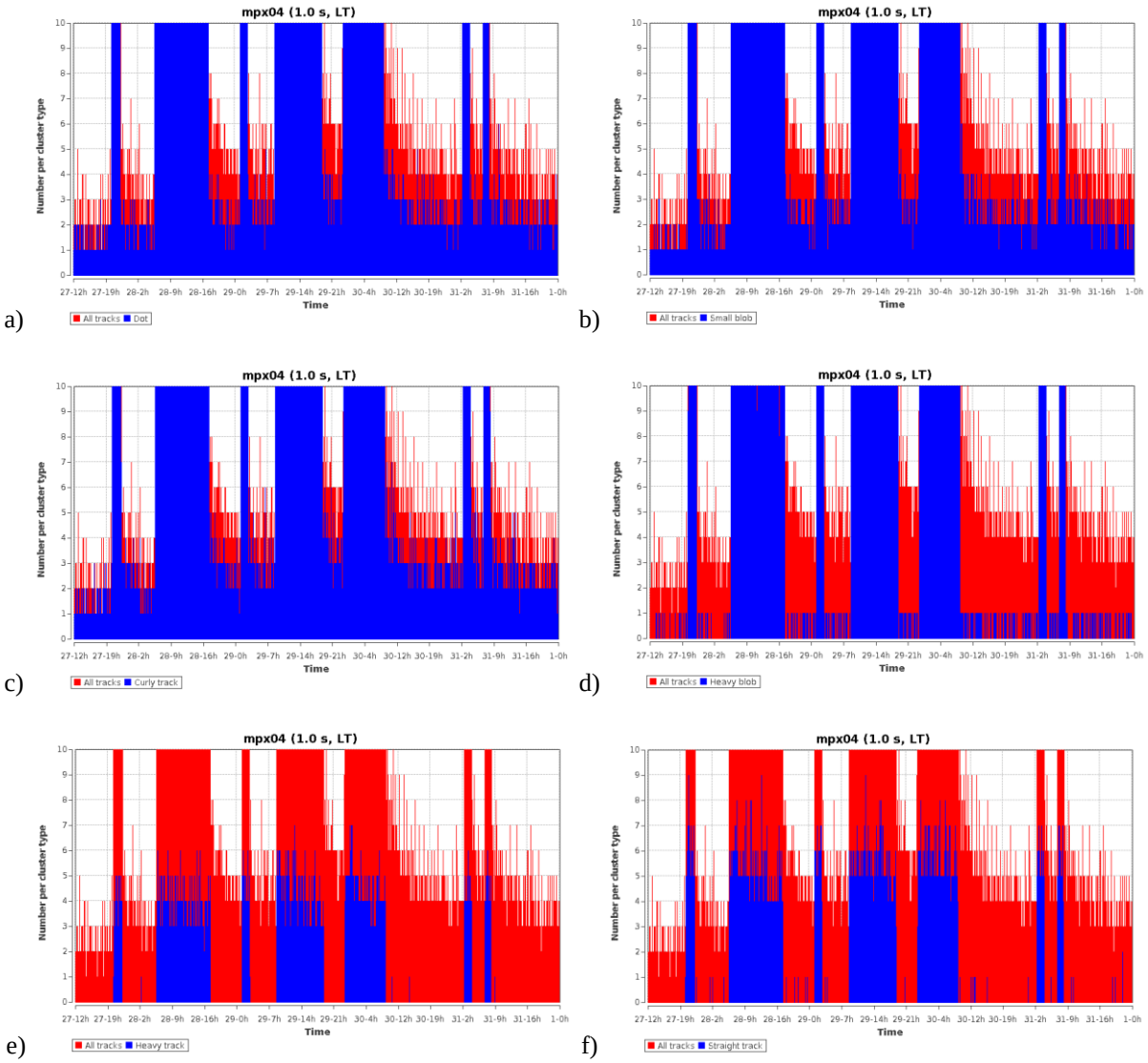

Figure 25. Cluster counts of different cluster types measured by MPX04 between 27th May 2011 (12:00) and 31st May (00:00). Seven runs were done during this time period corresponding to 7 columns in each figure. Red color indicates the sum of all clusters per frame, the blue color identifies cluster counts of different cluster types: a) dots (low energy electrons and photons), b) small blobs (electrons and photons), c) curly tracks (electron and photons), d) heavy blobs (low energy heavy charged particles including products of thermal neutrons reaction with ^{6}Li), e) heavy tracks (high energy heavy charged particles), and f) straight tracks (MIPs). Signal during no run is caused almost only by photons and electrons.

5.1 Environment activation

The induced activation as measured with an MPX detector can be further analyzed in terms of different decay components. An example of activation seen in detector MPX04 is shown in Fig. 26 with the inset cluster counts measured after the end of collisions. It shows three decay components with the following half-lives: 1.6 min, 4 hours and 32 hours (see Figs. 27 and 28). Beside this, in MPX15 measurements, the additional very long decay component is visible (see Fig. 28d) with the half-life more than 50 days.

Along the fast component, this count rate is initially two orders of magnitude higher than the background count rate as measured before any collision in 2008 with the same detector (see Fig. 10, where the exposure time was 120 times longer than in Fig. 27). After a period of two hours, the count rate decreases following the slow component.

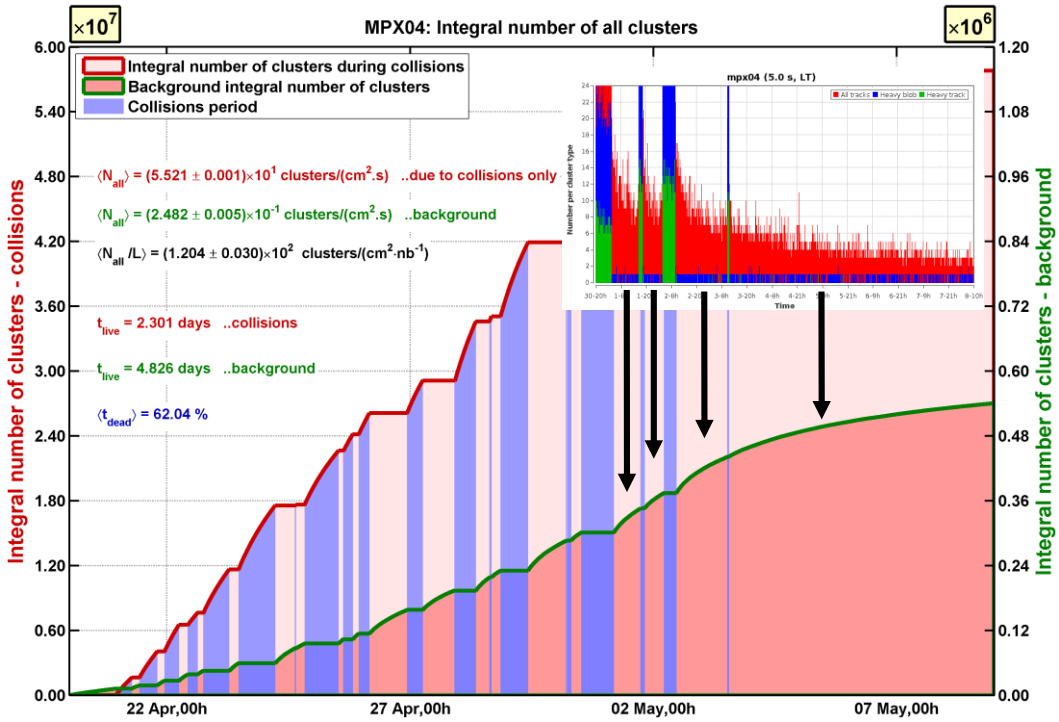

Figure 26. Example of environment activation observed in MPX04 in April and May 2011 (as shown on measured cluster counts inserted frame) and in a plot representing the integral number of clusters of all types measured during no-beam periods (green line). Beam periods are highlighted by blue columns. The observed activation corresponds to an integrated luminosity of 230 pb^{-1} and mean luminosity rate of 0.5 $nb^{-1}s^{-1}$ (20^{th} April – 3^{rd} May 2011).

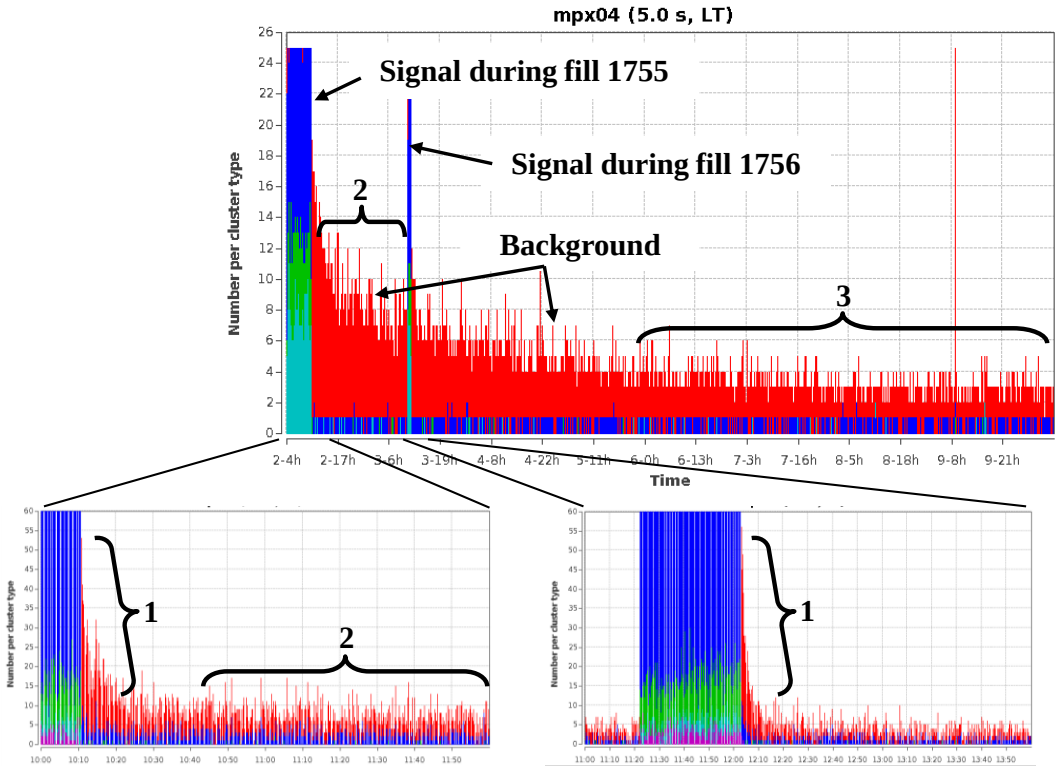

Figure 27. Measured background cluster counts in MPX04 from the end of fill 1755 from 2^{nd} May to 10^{th} May 2011. Details of the measured signal just after the end of beam collisions (fills 1755 and 1756) are presented in two detailed figures.

The shortest decay component in Fig. 27 numbered by 1 is especially visible just after the very short fill 1756 where radionuclides with a longer half-life have not yet been created with large activity (fill 1756 parameters: length 43 min, integrated luminosity 1590 nb^{-1}, mean luminosity rate 0.62 $nb^{-1}s^{-1}$). Different decay components fitted in Fig. 28 are labeled: 1 – very short, 2 – short, and 3 – long decay component. Colors represent different cluster types to visually distinguish collision periods (fills; blue/green columns over the whole height of the plots) from background signal produced by X-rays, gamma rays and electrons (red color).

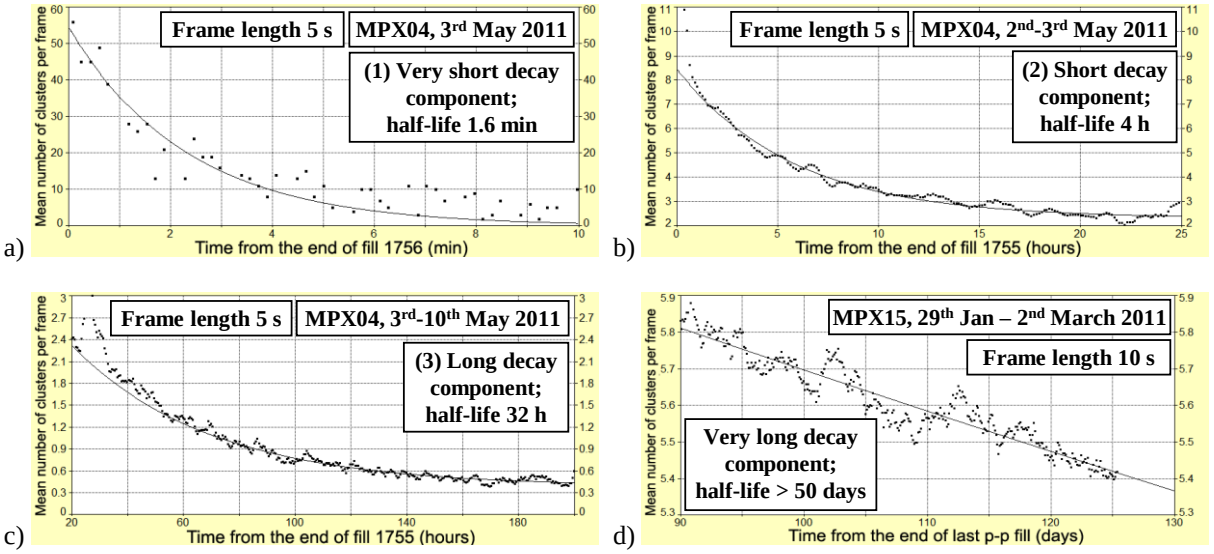

Figure 28. Exponential fits ($y = B + C.e^{-\lambda t}$, $\lambda = \ln(2)/T_{1/2}$, B is a constant background level; C is a normalization constant; y is a mean number of clusters per frame, $T_{1/2}$ is the half-life) of the measured individual radionuclide decay components. In figures a), b) and c) are presented fits to data highlighted by (1), (2) and (3) in Fig. 27 as measured by MPX04 between 2nd May and 10th May 2011. In figure d) the MPX15 measurement of background during no-beam period between 29th January and 2nd March 2011 shows the very long radionuclide decay component. The exponential fits give half-life $T_{1/2}$ of the very short (1), short (2), long (3) and very long (4) decay components 1.6 min, 4 h, 32 h, and > 50 days, respectively. Measured signal in figures b), c) and d) has been smoothed (arithmetic mean of measured cluster counts).

The radiation background expressed by the mean number of clusters per 60 s per cm^2 measured during periods with no beam at the ATLAS-MPX detectors positions from 2008 until end of May 2011 is shown in Tab. 4. The increase of the radiation background presented in Tab. 4 compared to data obtained before 2010 is seen from Tab. 5. Measured values are influenced by long-term statistical variations of natural radiation background and by residual material activation. Increase of the background signal caused by activation is visible mainly at the positions of MPX01, MPX02, MPX04, MPX05, MPX13, MPX14, and MPX15.

Date	MPX 01	MPX 02	MPX 03	MPX 04	MPX 05	MPX 06	MPX 07	MPX 08	MPX 09	MPX 10	MPX 11	MPX 12	MPX 13	MPX 14	MPX 15	MPX 16
	Mean number of background clusters per 60 s per cm^2															
Sep 2008	0.80	0.31	0.83	1.51	0.56	0.55	0.48	0.65	1.15	1.77	1.72	0.63	1.12	0.45	0.95	-
Sep 2008 uncertainty	0.13	0.07	0.15	0.25	0.10	0.12	0.10	0.14	0.19	0.18	0.17	0.10	0.21	0.08	0.22	-
Oct 2009	0.66	-	0.72	1.09	0.51	0.62	0.41	0.34	-	1.70	1.70	0.71	0.97	0.47	0.62	-
24 Feb 2010	0.76	-	0.92	1.00	0.51	0.61	0.44	0.34	0.59	1.73	1.67	0.68	0.78	0.46	0.60	0.91
13 May 2010	0.70	-	0.74	0.87	0.45	0.56	0.55	0.37	0.83	1.72	1.68	0.66	1.02	0.45	0.71	0.97
20 Jun 2010	0.76	-	0.88	0.86	0.47	0.56	0.48	0.31	0.89	1.73	1.67	0.65	1.01	HT	HT	0.97
28 Jul 2010; after 10 days without beam	0.99	-	0.65	0.89	0.46	0.60	0.61	0.32	0.60	1.71	1.69	0.67	1.10	HT	HT	0.98
29 Aug 2010; after end of August runs (after fill 1309)	9.15	-	0.83	1.20	0.58	0.62	0.50	0.30	0.73	1.75	1.66	0.57	1.41	8.83	94.14	1.19
14 Sept 2010; after 16 days without beam	1.01	-	0.77	1.11	0.50	0.61	0.65	0.34	0.79	1.71	1.69	0.53	0.89	1.03	11.60	1.17
12 Nov 2010; end of 2010 p-p runs	4.60	-	0.79	1.10	0.48	0.58	0.74	0.33	0.63	1.76	1.70	0.59	1.03	4.39	1034	1.16
4 Dec 2010; end of Pb-Pb runs	4.23	-	0.69	1.05	0.50	0.59	0.58	0.31	0.62	1.73	1.72	0.61	1.01	2.75	78.16	1.21
9 Mar 2011; 3 months without beam	1.56	0.26	0.51	0.68	0.49	0.56	0.56	0.32	2.44	1.76	1.98	0.58	0.78	3.26	24.32	0.95
16 Mar 2011; start of 2011 high lumi runs (before fill 1634)	3.15	0.35	0.47	0.73	0.53	0.60	0.59	0.33	2.44	1.78	1.93	0.59	0.80	4.41	37.01	0.95
25 Mar 2011; just after a set of fills 1634-1647	HT	2.89	1.06	3.80	1.66	1.08	0.52	0.37	2.57	1.73	2.10	0.64	5.94	HT	2004	1.02
7 Apr 2011; after 13 days without beam	HT	0.68	0.67	1.06	0.64	0.63	0.46	0.34	2.48	1.71	1.89	0.53	1.19	HT	HT	0.92
3 May 2011; just after a set of fills 1711-1756	HT	23.84	4.65	21.61	10.53	4.96	0.67	0.55	3.04	1.86	2.01	1.30	46.21	HT	HT	0.89
12 May 2011; after 8 days without beam	26.31	2.22	0.89	4.54	1.46	0.99	0.62	0.37	2.45	1.75	1.91	0.58	3.26	HT	1212	0.91
27 May 2011; after 2 days without beam	HT	22.38	3.73	18.68	8.31	3.69	0.71	0.50	2.90	1.87	1.98	1.21	36.45	HT	HT	0.96

Table 4. Radiation background (mean number of clusters per 60 s per cm^2) measured during periods with no beam at the ATLAS-MPX detectors positions from 2008 until end of May 2011 (MPX16 was installed later during February 2010, MPX02 and MPX09 were replaced during 2010-2011 LHC shutdown). Statistical uncertainties are within 3% except for September 2008 where they are stated individually. HT means detector in high threshold mode.

Date	MPX 01	MPX 02	MPX 03	MPX 04	MPX 05	MPX 06	MPX 07	MPX 08	MPX 09	MPX 10	MPX 11	MPX 12	MPX 13	MPX 14	MPX 15	MPX 16
	Ratio of mean number of background clusters															
Sep 2008	1.21	1.00	1.15	1.38	1.10	0.88	1.16	1.91	1.94	1.04	1.01	0.88	1.15	0.96	1.53	-
Oct 2009	1.00	-	1.00	1.00	1.00	1.00	1.00	1.00	-	1.00	1.00	1.00	1.00	1.00	1.00	-
24 Feb 2010	1.15	-	1.27	0.91	1.01	0.99	1.07	0.99	1.00	1.02	0.98	0.96	0.80	0.98	0.96	1.00
13 May 2010	1.06	-	1.02	0.80	0.89	0.91	1.34	1.08	1.41	1.01	0.99	0.93	1.05	0.96	1.14	1.07
20 Jun 2010	1.15	-	1.22	0.79	0.93	0.91	1.17	0.91	1.51	1.02	0.98	0.92	1.04	HT	HT	1.07
28 Jul 2010; after 10 days without beam	1.49	-	0.90	0.81	0.91	0.97	1.48	0.94	1.02	1.01	0.99	0.95	1.13	HT	HT	1.08
30 Aug 2010; after end of August runs (after fill 1309)	13.81	-	1.15	1.10	1.14	1.01	1.21	0.88	1.24	1.03	0.97	0.80	1.45	18.88	151.1	1.31
14 Sept 2010; after 16 days without beam	1.52	-	1.06	1.02	0.99	0.99	1.58	0.99	1.34	1.01	0.99	0.75	0.92	2.20	18.62	1.29
12 Nov 2010; end of 2010 p-p runs	6.94	-	1.09	1.01	0.95	0.94	1.80	0.96	1.07	1.03	1.00	0.83	1.06	9.39	1660	1.27
4 Dec 2010; end of Pb-Pb runs	6.38	-	0.95	0.96	0.99	0.96	1.41	0.91	1.05	1.02	1.01	0.86	1.04	5.88	125.5	1.33
9 Mar 2011; 3 months without beam	2.35	0.83	0.70	0.62	0.97	0.91	1.36	0.94	4.14	1.03	1.16	0.82	0.80	6.97	39.04	1.04
16 Mar 2011; start of 2011 high lumi runs (before fill 1634)	4.75	1.12	0.65	0.67	1.05	0.97	1.43	0.96	4.14	1.05	1.13	0.83	0.83	9.43	59.41	1.04
25 Mar 2011; just after a set of fills 1634-1647	HT	9.22	1.46	3.48	3.27	1.75	1.26	1.08	4.36	1.02	1.23	0.90	6.13	HT	3217	1.12
7 Apr 2011; after 13 days without beam	HT	2.17	0.93	0.97	1.26	1.02	1.12	0.99	4.20	1.01	1.11	0.75	1.23	HT	HT	1.01
3 May 2011; just after a set of fills 1711-1756	HT	76.02	6.42	19.76	20.77	8.04	1.63	1.61	5.15	1.09	1.18	1.83	47.67	HT	HT	0.98
12 May 2011; after 8 days without beam	39.71	7.08	1.23	4.15	2.88	1.61	1.51	1.08	4.15	1.03	1.12	0.82	3.36	HT	1945	1.00
27 May 2011; after 2 days without beam	HT	71.36	5.15	17.08	16.39	5.98	1.72	1.46	4.92	1.10	1.16	1.71	37.60	HT	HT	1.05

Table 5. Mean number of background clusters given in Tab. 4 related to Oct 2009 data (9th March 2011 for MPX02 and Feb 2010 for MPX09 and MPX16). Statistical uncertainties are within 3%. HT means detector in high threshold mode.

5.2 Dose rate calibration

The instantaneous radiation background level depends on the luminosity rate, the integrated luminosity, and the total time over which the luminosity is integrated.

Dose rate calibration measurements were done with an ATLAS-MPX detector of reference exposed to gamma ray sources of known ambient dose equivalent rate (H*(10) rate) in a set-up of known geometry to provide a quantitative estimate of activation and associated H*(10) rate due to LHC operation (see Fig. 29). If the radiation background photon field mean energy is close to the photon energies in the calibration field, one conversion coefficient can be used to calculate the photon H*(10) rate from measured cluster rate caused by photons from the natural background and from the residual material activation. The ATLAS-MPX detector of reference was exposed to ^{60}Co (main energies of 1173 and 1332 keV) and ^{137}Cs (main energy of 662 keV) photon sources in separate measurements. The calibration coefficient between cluster rate and H*(10) rate was found to be $(2.26 \pm 0.19) \times 10^{-10}$ Sv.cluster^{-1} and $(1.71 \pm 0.07) \times 10^{-10}$ Sv.cluster^{-1} for ^{60}Co and ^{137}Cs, respectively. The average value of 2.0×10^{-10} Sv.cluster^{-1} was used to convert cluster rate into H*(10) rate.

Using this conversion coefficient, it was found that the natural radiation background measured by all ATLAS-MPX detectors in September 2008 was ranging from 0.01 to 0.04 μSv.h^{-1} which is in good agreement with the supposed natural background level in the ATLAS cavern.

Figure 29 illustrates the increase of the radiation background as measured by MPX01 after fill 1309 on 30th August 2010 and the comparison to the measured signal in photon calibration fields. During the first 15 minutes after the end of collisions, applying the pattern recognition, it is observed that 54% of clusters measured with MPX01 consist of dots and small blobs and 46% of clusters correspond to curly tracks. By comparing with the ^{60}Co calibration test measurements, one observes that the MPX01 response is similar to the response of the ATLAS-MPX detector of reference exposed to the ^{60}Co source (Fig. 29a). A mean H*(10) rate of 1.30 μSv.h^{-1} is measured with MPX01. During the second period of 15 minutes after the end of collisions, the mean H*(10) rate for this detector is estimated to be 0.91 μSv.h^{-1}.

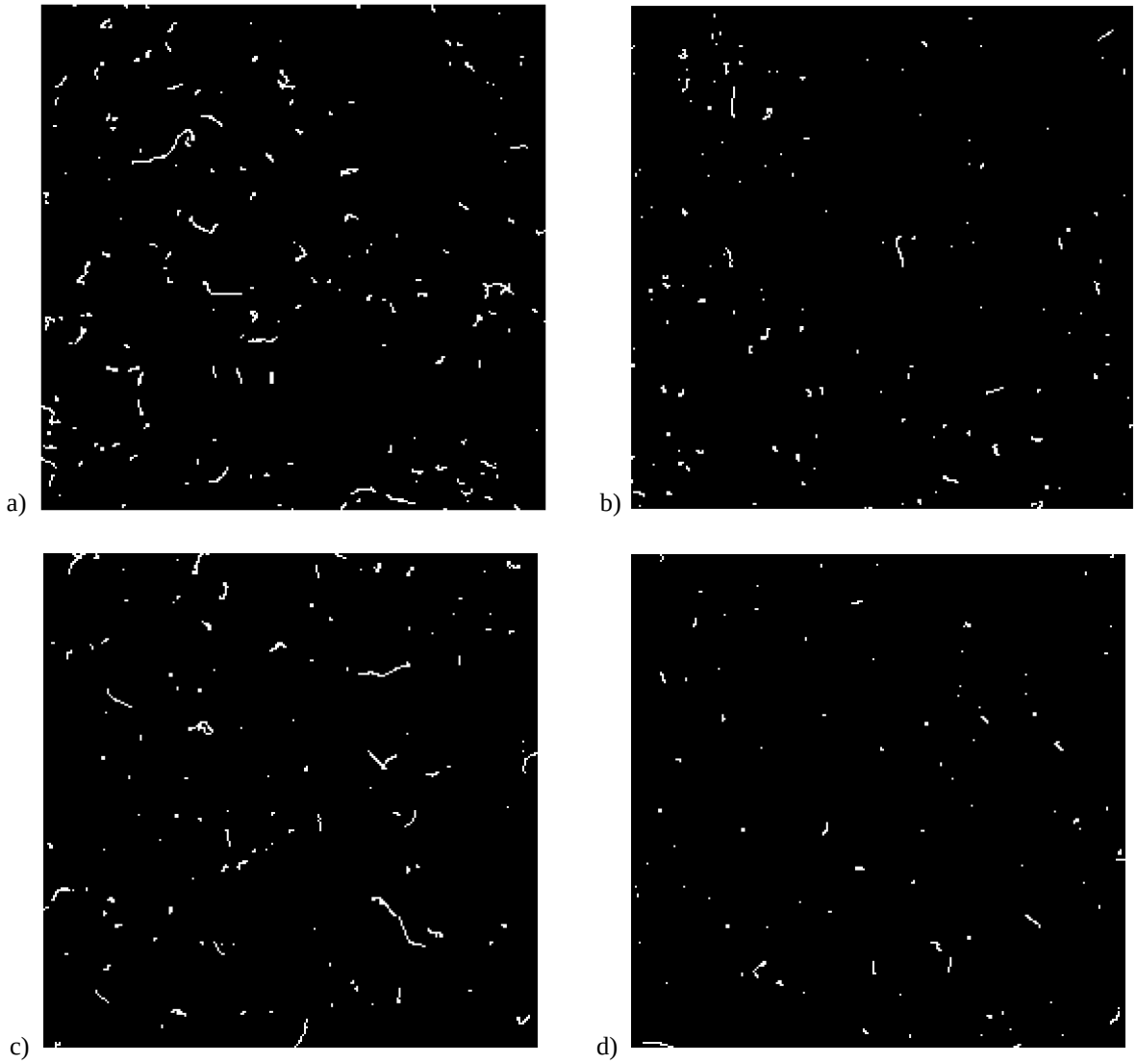

Figure 29. Example of the response of an ATLAS-MPX detector of reference exposed to: a) ^{60}Co radiation source (1173 keV and 1333 keV photons), b) ^{137}Cs radiation source (662 keV photons). The mean length of the tracks is increasing with increasing incident photon energy. Comparison with the response of MPX01 recorded after end of collisions (fill 1309 on 30th August 2010). c) Integration during first 15 min after the collision (1 min lifetime) shows a composition similar to ^{60}Co. d) Integration during next 15 min (1 min lifetime) shows a composition similar to ^{137}Cs.

Table 6 describes the photon ambient dose equivalent rate H*(10) caused by induced activity as determined with ATLAS-MPX detectors on 29th May 2011. Between 15th and 29th May there were 16 fills with integrated luminosity greater than 2.5 pb^{-1}, with total integrated luminosity of 260 pb^{-1} and

luminosity rate between 0.6 and 1.0 $nb^{-1}.s^{-1}$. Significant increase of H*(10) rate caused by induced activity was detected at the positions of MPX02, 03, 04, 05, 06, 12 and 13 (note that MPX01, 14 and 15 were set in high threshold mode, thus insensitive to low energy transfer particles). The radiation background level was compared before fill 1815 (29th May; integrated luminosity 38 pb^{-1}; mean luminosity rate 1.0 $nb^{-1}.s^{-1}$) and after this fill during several periods of time ranging from 5 min up to 24 hours. It can be seen that for this integrated luminosity and luminosity rate, the H*(10) rate is increased by a factor of about 2 - 6.

	H*(10) rate [µSv.h^{-1}]			**H*(10) rate caused by induced activity, normalized at its value 5 min after fill 1815 on 29th May 2011 (integrated luminosity 38 pb^{-1}; mean luminosity rate 1.0 nb^{-1}.s^{-1})**					
Device	**15th May 2011; 12 days before fill 1782**	**29th May 2011, 30 min before fill 1815**	**29th May 2011, 5 min after fill 1815**	**5 min after fill 1815**	**30 min after fill 1815**	**2 h after fill 1815**	**5 h after fill 1815**	**10 h after fill 1815**	**1 day after fill 1815**
MPX02	0.03	0.83	5.87	100%	55%	39%	25%	18%	8%
MPX03	0.01	0.15	0.94	100%	66%	52%	46%	24%	17%
MPX04	0.06	0.79	3.41	100%	63%	48%	40%	29%	15%
MPX05	0.02	0.49	1.82	100%	62%	46%	32%	24%	8%
MPX06	0.03	0.15	0.77	100%	69%	53%	38%	26%	16%
MPX12	0.01	0.06	0.12	100%	73%	61%	49%	42%	37%
MPX13	0.06	1.28	7.26	100%	57%	39%	24%	18%	6%

Table 6. Comparison of photon H*(10) rate caused by induced activity in May 2011 and decrease of H*(10) rate after fill 1815 for detectors MPX02, 03, 04, 05, 06, 12 and 13 (detectors operated at low threshold for which activation was clearly visible).

Figure 30 shows the decrease of the H*(10) rate as measured by MPX02 during a period of 13 days after the end of fill 1901 (integrated luminosity 46.5 pb^{-1}, mean luminosity rate 3.4 $pb^{-1}.h^{-1}$).

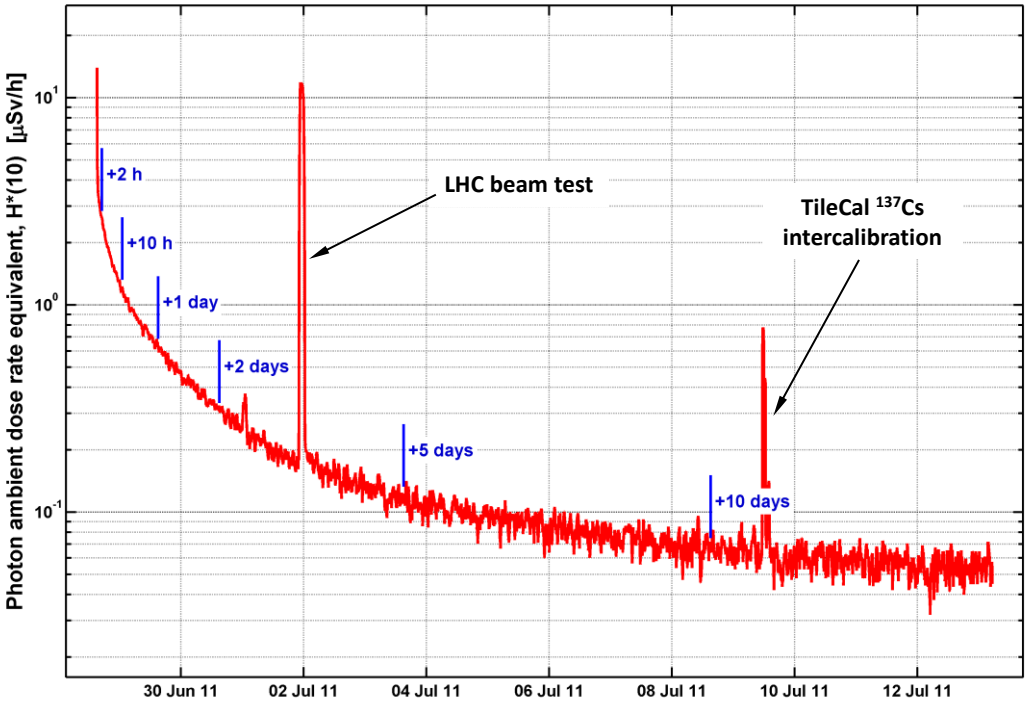

Figure 30. Decrease of the ambient dose rate equivalent as measured by MPX02 during a 13 days period after the end of fill 1901 (integrated luminosity of 46.5 pb^{-1}, mean luminosity rate of 3.4 $pb^{-1}.h^{-1}$). Blue marks represent time from the end of the fill.

6. Comparison of measurements with simulations

The results of measurements done with the ATLAS-MPX detectors presented in this section were obtained by operating the ATLAS-MPX detectors in tracking mode (at low threshold – 10 keV and relatively short exposure times). For the presentation of these results, it was found convenient to separate the measured particle types into four categories (see section 2.2):

- **Low energy transfer particles (LETP)**
  - electrons not recognized as MIPs (see below);
  - gamma and X-rays (through scattered electrons);
  - protons with approximately E > 200 MeV not recognized as MIPs (see below);
  - muons with approximately E > 25 MeV not recognized as MIPs (see below);
  - pions with approximately E > 32 MeV not recognized as MIPs (see below);
  - charged kaons with approximately E > 110 MeV not recognized as MIPs (see below);
- **High energy transfer particles (HETP)**
  - deuterons, tritons, alphas, heavy ions;
  - protons with approximately E < 200 MeV;
  - fast neutrons (through nuclear reactions);
  - muons with approximately E < 25 MeV;
  - pions with approximately E < 32 MeV;
  - charged kaons with approximately E < 110 MeV;
- **MIPs**
  - electrons with approximately E > 20 MeV registered as a straight track;
  - protons with approximately E > 200 MeV registered as a straight track;
  - muons with approximately E > 25 MeV registered as a straight track;
  - pions with approximately E > 32 MeV registered as a straight track;
  - charged kaons with approximately E > 110 MeV registered as a straight track;
- **Thermal neutrons**
  - neutrons with E < 0.5 eV.

The energy limit for HETP protons, muons, pions and charged kaons comes from the collision stopping power in silicon which was set to approximately 45 keV of deposited energy per 55 μm track length (i.e. the size of one pixel). This value was experimentally verified with the evaluation of the detector response to 200 MeV proton irradiation.

After the cluster analysis (see description in section A.1.1), several types of clusters are grouped into the following categories:

- LETP are visualized as sum of dots, small blobs and curly tracks registered in the whole chip area,
- HETP are visualized as heavy blobs and heavy tracks registered in the whole chip area, LiF and border regions excepted,
- MIPs are recognized as sum of straight tracks registered in the whole chip area,
- Thermal neutrons are identified by heavy blobs below the LiF converter.

ATLAS-MPX results obtained during collisions are normalized to the unit luminosity (nb^{-1}). The luminosity data used comes from LUCID measurements.

The procedure of determination of measured values presented in this section is described in detail in Appendix F.

6.1 Monte Carlo calculations

ATLAS-MPX measurements were compared to two different Monte Carlo simulations of ATLAS cavern. The first Monte Carlo simulated data were obtained from the Radiation Background Task Force web page [11]. The simulations were done in 2003 using GCALOR package for GEANT3 with the Baseline Shielding Layout geometry of January 2003 and resulted in 2D maps of flux of different types of particles in ATLAS detector. These simulated 2D distributions were compared to the interpolated ATLAS-MPX measurement data to graphically visualize the match between both data. For the data interpolation the side and axial symmetry has been assumed. These simulations are referred to as "MC-2003" in the following text.

The second set of Monte Carlo simulated data was obtained from Mike Shupe in 2010 [12]. Simulations were performed with a PHOJET Geant3/GCALOR Monte Carlo code especially for ATLAS-MPX detectors locations using a model with 16 m radius ATLAS cavern. The simulations followed all particles created in proton-proton interactions at $\sqrt{s} = 7$ TeV and any subsequent interactions along their path through the ATLAS cavern up to their absorption. Every particle crossing the scoring volume was recorded and its type, energy, position and direction vector were stored in a file. Thermal neutron flux and neutron spectral flux distribution presented in this section were obtained from information stored in these files. Scoring volumes were cylindrical shells around beam axis either with several cm length and 1 mm thickness or with 1 mm length and several cm thickness, depending on sensor chip orientation (see Fig. 9). There were 13 scoring volumes with radii and Z-coordinates matching position of 15 ATLAS-MPX detectors (MPX01 and MPX02 were assumed to be symmetrical to MPX14 and MPX13, respectively). Data obtained from these simulations were used for comparison with measurement results of each individual ATLAS-MPX detector. These simulations are referred to as "MC-2010" in the following text.

For normalization of simulated data per unit luminosity, the inelastic p-p cross section at $\sqrt{s} = 7$ TeV of 71 mb was assumed [13] as a mean of values presented in [9]. The procedure of determination of simulated values presented in this section is described in detail in Appendix G.

Supplemental Monte Carlo calculations were performed in order to obtain ATLAS-MPX energy and angular detection efficiency to photons, thermal and fast neutrons, electrons, protons, muons and pions. Such data were used to convert the MC-2010 simulated particle numbers into ATLAS-MPX cluster rates. In case of thermal neutrons, the efficiency data were also used to estimate the anisotropy correction of thermal neutron fluence. These MC simulations were done utilizing the general-purpose MC code MCNPX in version 2.7e [14] and they are described in more detail in Appendix H.

6.2 Low energy transfer particles (LETP)

The spatial distribution of low energy transfer particles (LETP) cluster rate per unit luminosity as measured with the ATLAS-MPX detectors is shown in Fig. 31a as a function of the distance R from the beam axis and the coordinate Z along the beam axis, from the interaction point (IP1). The lowest cluster rate per unit luminosity is recorded with MPX11 which is located on the UX15 cavern wall (see Tab. 1). The highest cluster rate per unit luminosity is recorded with MPX15 (closest to the beam axis, along LUCID).

For comparison, Fig. 31b shows the distribution of electrons determined by MC-2003 simulations. The comparison with simulated data is approximate because the LETP count rate measured with ATLAS-MPX detectors consists of several different particle types as described at the beginning of this section.

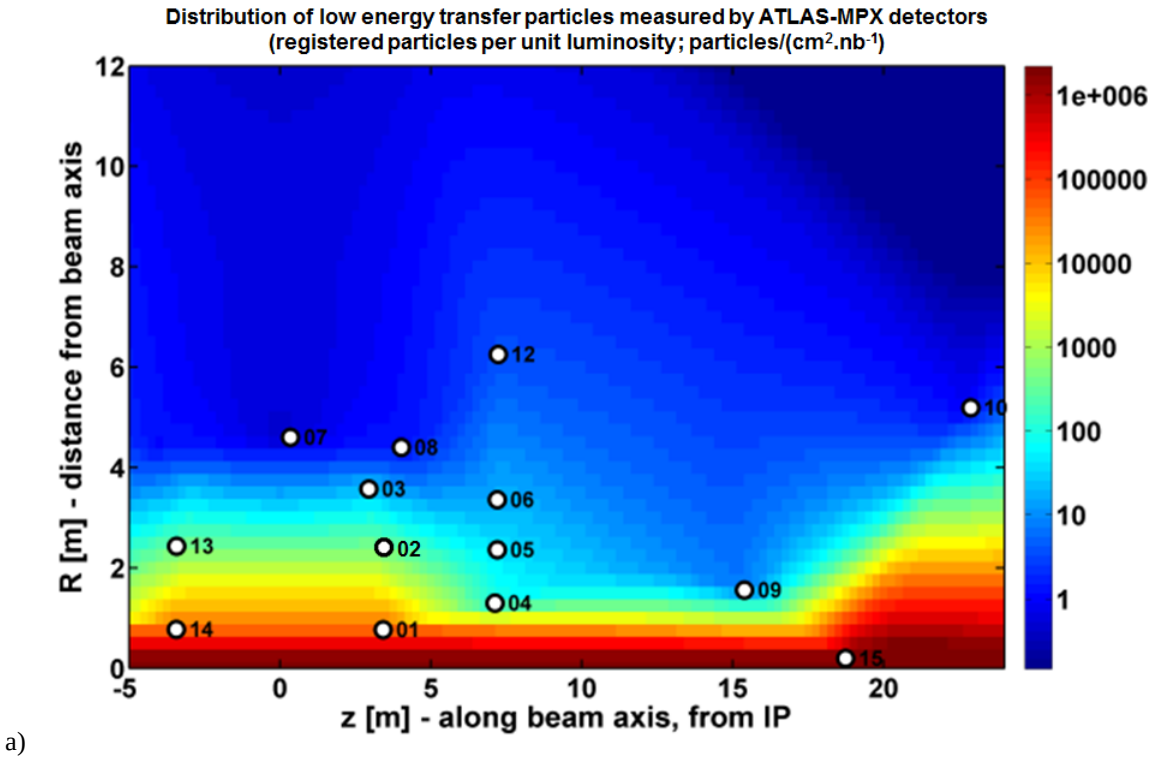

a)

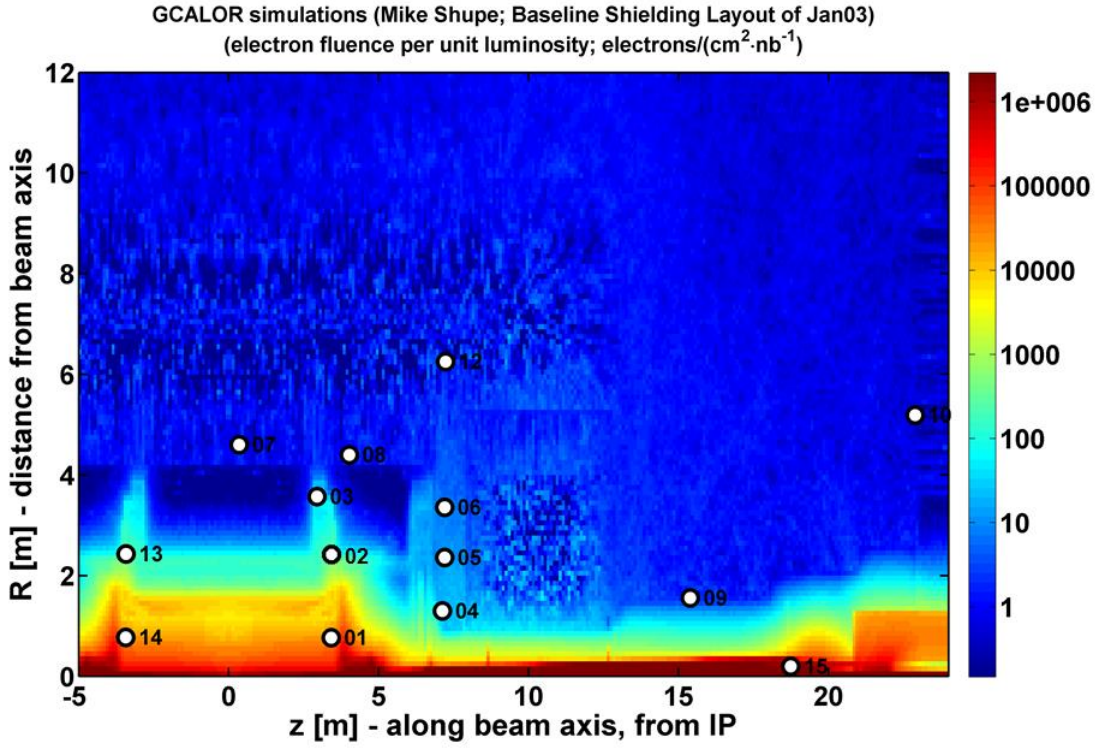

b)

Figure 31. a) Spatial distribution of low energy transfer particles interpolated from data obtained from ATLAS-MPX measurements. b) Calculated spatial distribution of electrons (MC-2003 simulations). MPX11 is not shown on the figure as its coordinates (Z = 4.86 m, R = 16.69 m) do not match the y-scale used for the display of the simulated distribution of electrons.

The summary of ATLAS-MPX measurements compared to MC-2010 simulations is presented in Tab. 7 and depicted in Fig. 32. Simulated value of LETP currents is the sum of contributions from

electrons, photons, protons, muons, pions and charged kaons. Particles with the following energies and angles were counted only: muons, pions, charged kaons and protons not counted as MIPs with energy higher than 25, 32, 110 and 200 MeV, respectively, all electrons not counted as MIPs and photons. The contribution of each particle type to the simulated LETP current was calculated from the number of above mentioned particles multiplied by corresponding mean energy-angular detection efficiency according to the method described in detail in subsection H.2 of Appendix H. The potential contribution of fast neutrons through the elastic scattering on silicon nuclei in the sensor chip was neglected.

Measurement uncertainty in Tab. 7 expresses the dispersion of the individual values of LETP cluster rate around the mean and it is calculated according to a procedure described in Appendix F. In any case this uncertainty should not be confused with the measurement statistical uncertainty during collisions which varies between 0.01 and 0.07% for MPX01-15 and rises to 0.3% for MPX16.

Detector	**ATLAS-MPX average LETP background cluster rate per second [$cm^{-2}.s^{-1}$]**	**ATLAS-MPX average LETP collision cluster rate per unit luminosity [cm^{-2}/nb^{-1}]**	**MC-2010 LETP collision current per unit luminosity [cm^{-2}/nb^{-1}] ***	**Ratio MC-2010 / ATLAS-MPX**	**Contribution of photons to the total LETP count rate**
MPX01	(1.77 ± 0.01) E-2	(5.98 ± 0.69) E+04	(3.55 ± 0.01) E+04	0.59 ± 0.07	14%
MPX02	(2.31 ± 0.01) E-2	(2.27 ± 0.19) E+02	(1.22 ± 0.02) E+02	0.54 ± 0.05	67%
MPX03	(1.57 ± 0.01) E-2	(3.11 ± 0.17) E+01	(1.42 ± 0.03) E+01	0.46 ± 0.03	73%
MPX04	(1.98 ± 0.01) E-2	(1.16 ± 0.02) E+02	(8.65 ± 0.12) E+01	0.75 ± 0.02	84%
MPX05	(8.80 ± 0.01) E-3	(4.87 ± 0.18) E+01	(2.11 ± 0.05) E+01	0.43 ± 0.02	70%
MPX06	(1.08 ± 0.01) E-2	(2.03 ± 0.07) E+01	(1.04 ± 0.02) E+01	0.51 ± 0.02	81%
MPX07	(9.22 ± 0.01) E-3	(4.55 ± 0.10) E-01	(7.31 ± 0.32) E-01	1.61 ± 0.08	80%
MPX08	(5.61 ± 0.01) E-3	(1.22 ± 0.03)	(6.37 ± 0.31) E-01	0.52 ± 0.03	80%
MPX09	(1.42 ± 0.01) E-2	(5.96 ± 0.53)	(1.68 ± 0.06)	0.28 ± 0.03	86%
MPX10	(2.87 ± 0.01) E-2	(1.06 ± 0.02)	(6.63 ± 0.28) E-01	0.62 ± 0.03	77%
MPX11	(2.77 ± 0.01) E-2	(3.07 ± 0.07) E-01	(5.47 ± 0.05) E-01	1.78 ± 0.04	98%
MPX12	(1.25 ± 0.01) E-2	(4.04 ± 0.11)	(1.88 ± 0.02)	0.47 ± 0.01	97%
MPX13	(2.09 ± 0.01) E-2	(3.81 ± 0.09) E+02	(1.22 ± 0.02) E+02	0.32 ± 0.01	67%
MPX14	(1.53 ± 0.01) E-2	(5.61 ± 0.65) E+04	(3.55 ± 0.01) E+04	0.63 ± 0.07	14%
MPX15	(1.74 ± 0.01) E-2	(2.59 ± 0.33) E+06	(2.01 ± 0.01) E+06	0.78 ± 0.10	14%
MPX16	(1.80 ± 0.01) E-2	(6.99 ± 2.94) E-04	-	-	-

* pp inelastic cross section of 71 mb assumed [13]

Table 7. Average background LETP cluster rate (no collisions period) and the average LETP cluster rate per unit luminosity during collisions as measured by ATLAS-MPX detectors. The background LETP cluster rates are calculated from measurements done in 2010 (before the activation caused by high luminosity runs in 2011). On the other hand, the LETP collision cluster rates were determined from runs in 2011 (except for detectors MPX01, MPX14 and MPX15 operating in high threshold in 2011). The statistical uncertainty of the measurement during collisions varies between 0.01 and 0.07% for MPX01 - MPX15 and rises to 0.3% for MPX16. For comparison, MC-2010 calculated LETP currents are stated as well. Values from MC simulation include the following particles: muons, pions, charged kaons and protons not counted as MIPs with the energy higher than 25, 32, 110 and 200 MeV, respectively. Also, electrons not counted as MIPs are included and photons. See Appendices F, G and H for details on determination of measured and simulated values and their uncertainties presented in this table.

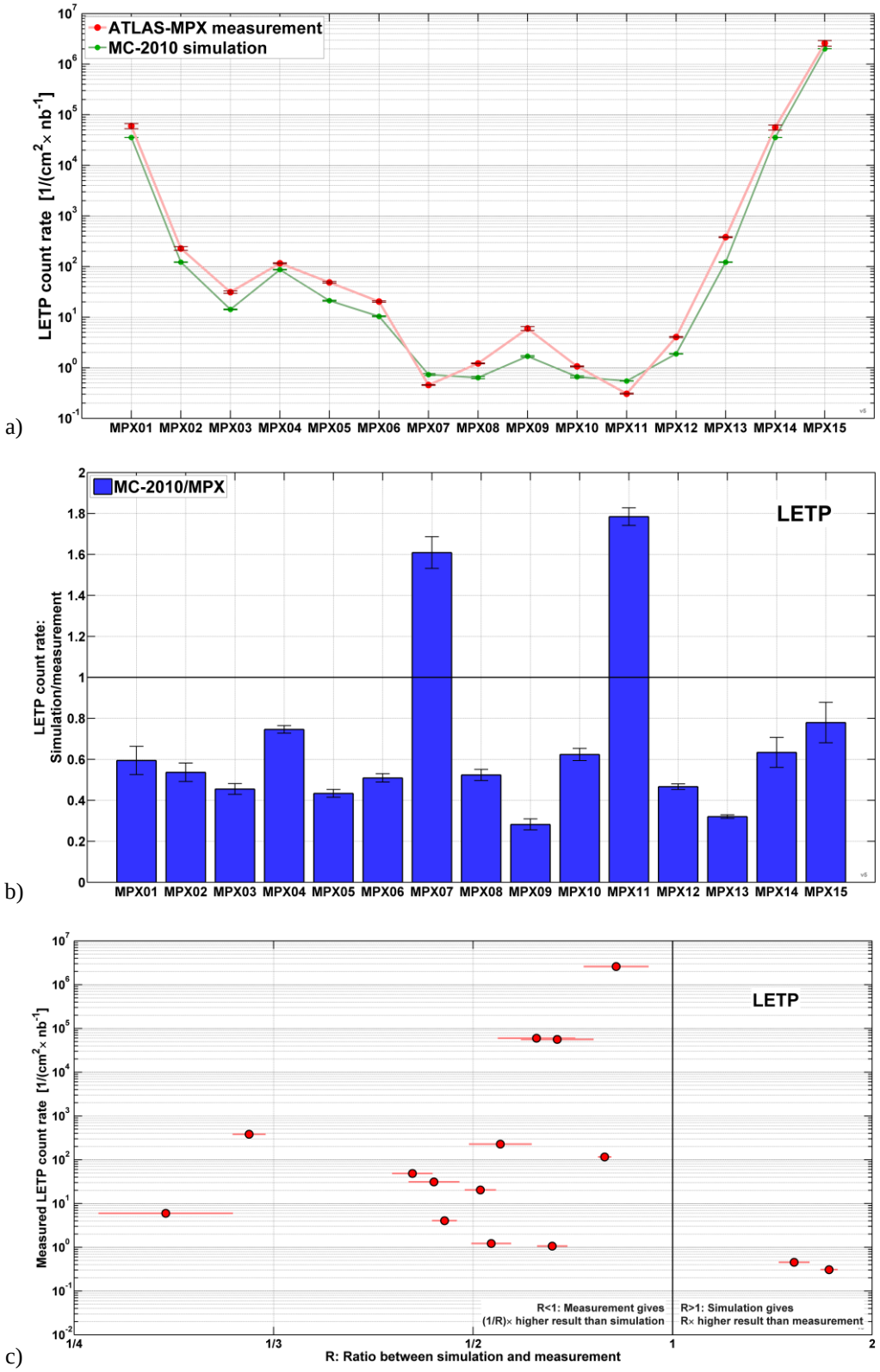

Figure 32. a) Measured (red) and MC-2010 simulated (green) LETP count rates during collisions at all ATLAS-MPX positions. b) Ratio of simulated and measured LETP count rates at all ATLAS-MPX positions. The ratio usually varies around the value of 0.5. This can be caused by lower energy cut-off limit in MC-2010 simulations which was set to 0.8 MeV resulting in underestimation of the number of electrons at MPX locations. c) Measured LETP count rate plotted against the corresponding ratio of simulated and measured LETP count rates.

6.3 High energy transfer particles (HETP)

The spatial distribution of high energy transfer particles (HETP) cluster rate per unit luminosity as measured with the ATLAS-MPX detectors is shown in Fig. 33a as a function of the distance R from the beam axis and the coordinate Z along the beam axis, from the interaction point (IP1). The lowest cluster rate is recorded with the detector MPX11 which is located on the UX15 cavern wall (see Tab. 1). The highest cluster rate is recorded with MPX15 (closest to the beam axis, along LUCID).

For comparison, Fig. 33b shows the distribution of protons calculated with MC-2003 simulations. The comparison with simulated data is approximate because the HETP count rates measured with ATLAS-MPX detectors consist of several different particle types as described at the beginning of this section: protons, heavy charged particles and low energy muons, pions and charged kaons, coming from outside the ATLAS-MPX detector, protons created by neutron recoils in the ATLAS-MPX device, including polyethylene convertor above the sensor, and signal from atomic nuclei recoiled by fast neutron interactions inside the sensor.

The summary of ATLAS-MPX measurements compared to MC-2010 simulations is presented in Tab. 8 and depicted in Fig. 34. Values of simulated HETP currents include protons with $E < 200$ MeV, all light nuclei, muons with $E < 25$ MeV, pions with $E < 32$ MeV, charged kaons with $E < 110$ MeV and signal caused by fast neutrons. The contribution of each particle type to the simulated HETP current was calculated from the number of above mentioned particles multiplied by corresponding mean energy-angular detection efficiency according to the method described in subsection H.3 of Appendix H. As seen from Tab. 8, there is a decent agreement between measured and simulated data. However, for some MPX detectors there is very low statistics of HETP from MC simulations.

Measurement uncertainty in Tab. 8 expresses the dispersion of the individual values of HETP cluster rate around the mean and it is calculated according to a procedure described in Appendix F. In any case this uncertainty should not be confused with the measurement statistical uncertainty during collisions which varies between 0.1 and 0.7% for MPX01 - MPX15 and rises to 2.5% for MPX16.

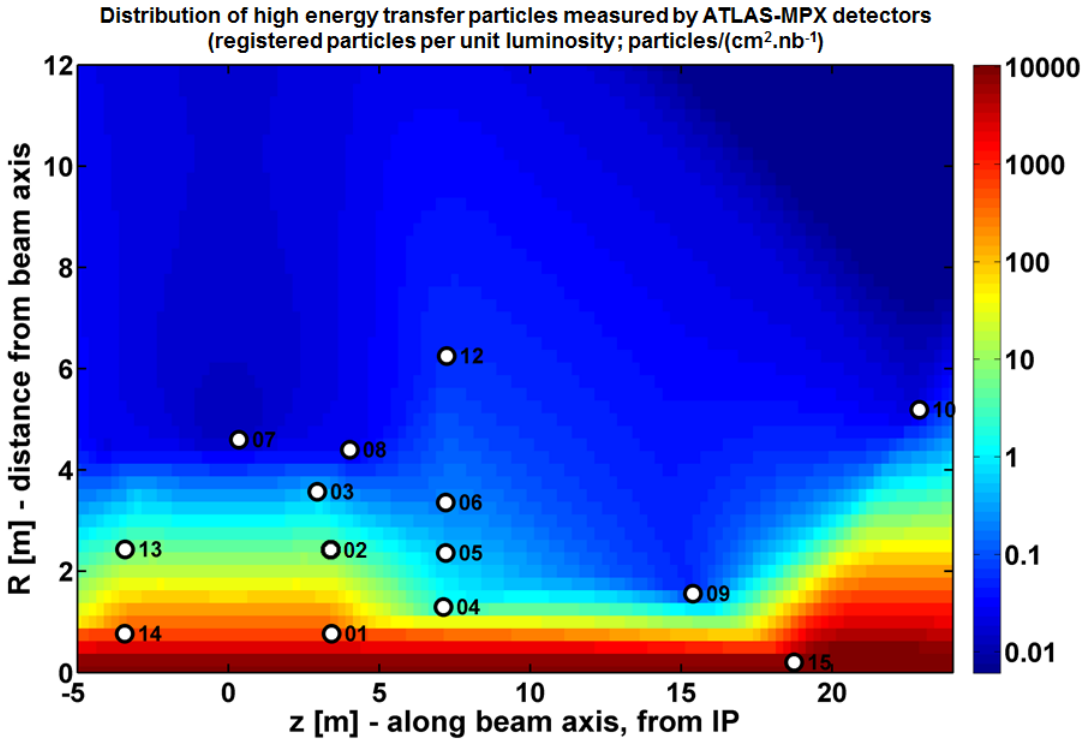

a)

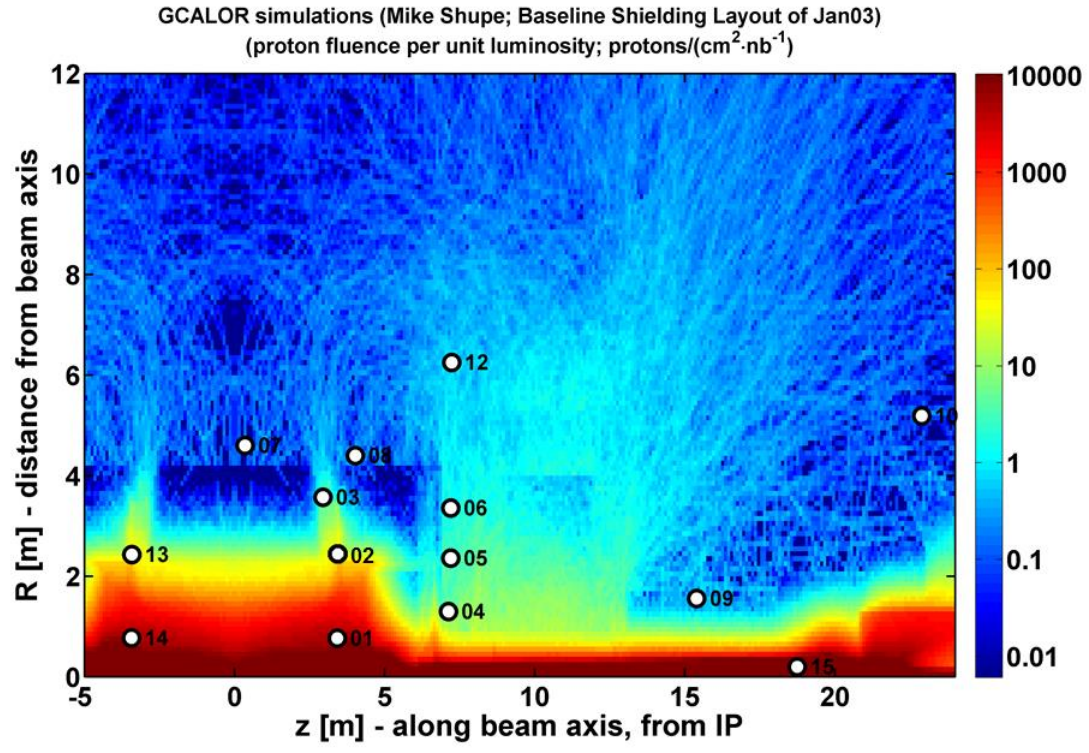

b)

Figure 33. a) Spatial distribution of high energy transfer particles (HETP) interpolated from data obtained from ATLAS-MPX measurements. b) Calculated spatial distribution of protons (MC-2003 simulations). The detector MPX11 is not shown on the figure as its coordinates (Z = 4.86 m, R = 16.69 m) do not match the y-scale used for the display of the simulated distribution of protons.

Measured HETP count rates compared to the MC-2010 simulated HETP count rates are depicted in Fig. 34.

Detector	ATLAS-MPX average HETP background cluster rate per second [$cm^{-2}.s^{-1}$]	ATLAS-MPX average HETP collision cluster rate per unit luminosity [cm^{-2}/nb^{-1}]	MC-2010 HETP collision current per unit luminosity [cm^{-2}/nb^{-1}] *	Ratio MC-2010 / ATLAS-MPX	Contribution of fast neutrons to the total HETP count rate
MPX01	(3.10 ± 0.05) E-4	(6.68 ± 1.04) E+02	(1.51 ± 0.02) E+03	2.27 ± 0.35	6%
MPX02	(1.13 ± 0.03) E-3	(3.25 ± 0.28)	(4.44 ± 0.27)	1.37 ± 0.14	43%
MPX03	(2.69 ± 0.03) E-4	(4.92 ± 0.30) E-01	(7.61 ± 0.40) E-01	1.55 ± 0.12	81%
MPX04	(1.21 ± 0.01) E-3	(1.77 ± 0.04)	(5.20 ± 0.55)	2.94 ± 0.32	33%
MPX05	(3.18 ± 0.04) E-4	(5.23 ± 0.24) E-01	(3.90 ± 0.17) E-01	0.75 ± 0.05	91%
MPX06	(2.97 ± 0.04) E-4	(2.20 ± 0.10) E-01	(2.68 ± 0.32) E-01	1.22 ± 0.16	76%
MPX07	(2.72 ± 0.03) E-4	(4.26 ± 0.32) E-03	(5.25 ± 0.51) E-02	12.35 ± 1.52	73%
MPX08	(2.50 ± 0.03) E-4	(1.18 ± 0.07) E-02	(1.35 ± 0.73) E-02	1.15 ± 0.62	46%
MPX09	(1.41 ± 0.02) E-4	(8.95 ± 0.83) E-02	(2.12 ± 0.26) E-01	2.37 ± 0.37	58%
MPX10	(3.87 ± 0.04) E-4	(1.16 ± 0.05) E-02	(2.51 ± 0.08) E-02	2.17 ± 0.12	100%
MPX11	(4.23 ± 0.04) E-4	(6.41 ± 0.38) E-03	(1.03 ± 0.02) E-02	1.60 ± 0.10	100%
MPX12	(2.76 ± 0.03) E-4	(5.37 ± 0.20) E-02	(9.21 ± 0.48) E-02	1.71 ± 0.11	64%
MPX13	(2.94 ± 0.04) E-4	(5.38 ± 0.17)	(4.44 ± 0.27)	0.83 ± 0.06	43%
MPX14	(3.13 ± 0.06) E-4	(6.17 ± 0.81) E+02	(1.51 ± 0.02) E+03	2.45 ± 0.32	6%
MPX15	(3.34 ± 0.07) E-4	(1.20 ± 0.26) E+04	(1.42 ± 0.05) E+04	1.19 ± 0.26	11%
MPX16	(3.78 ± 0.04) E-4	(9.02 ± 3.78) E-05	-	-	

* pp inelastic cross section of 71 mb assumed [13]

Table 8. Average background HETP cluster rate (no collisions period) and the average HETP cluster rate per unit luminosity during collisions as measured by ATLAS-MPX detectors. The background HETP cluster rates are calculated from all measurements done in 2010. The HETP collision cluster rates were determined from runs in 2011 (except for MPX01, MPX14 and MPX15 operating at high threshold in 2011). The statistical uncertainty of the measurement during collisions varies between 0.1 and 0.7% for MPX01 - MPX15 and rises to 2.5% for MPX16. For comparison, MC-2010 calculated HETP currents are stated as well. Values from MC simulation include protons with E < 200 MeV, all light nuclei, muons with E < 25 MeV, pions with E < 32 MeV and charged kaons with E < 110 MeV. Also, fast neutrons are included (see Appendix H). See Appendix F to Appendix H for details on determination of measured and simulated values and their uncertainties presented in this table.

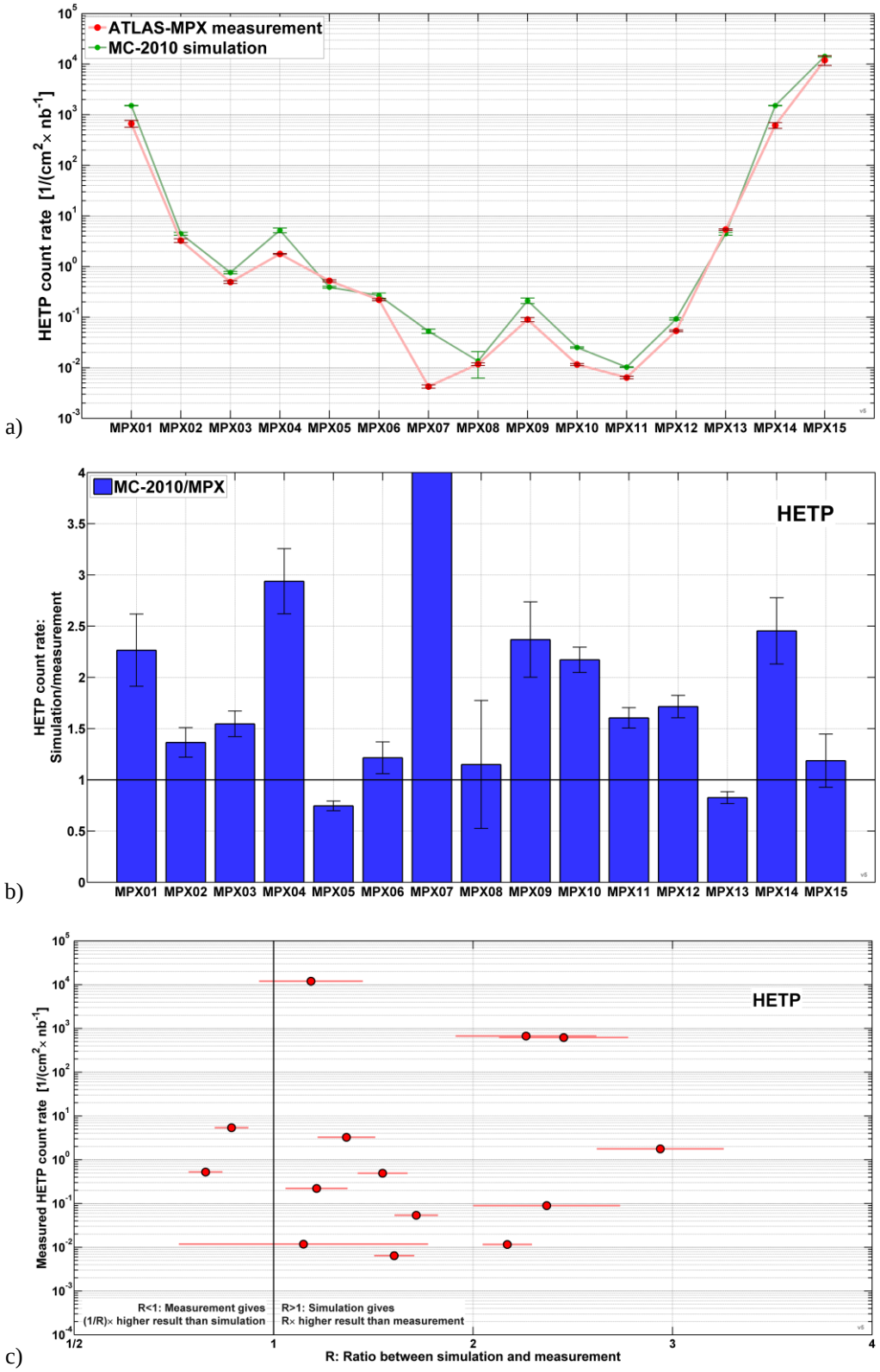

Figure 34. a) Measured (red) and MC-2010 simulated (green) HETP count rates during collisions at all ATLAS-MPX positions. b) Ratio of simulated and measured HETP count rates at all ATLAS-MPX positions. c) Measured HETP count rate plotted against the corresponding ratio of simulated and measured HETP count rates.

6.4 Minimum ionizing particles

The spatial distribution of MIP cluster rate per unit luminosity as measured with the ATLAS-MPX detectors is shown in Fig. 35a as a function of the distance R(m) from the beam axis and the coordinate Z(m) along the beam axis, from the interaction point (IP1). The lowest MIP cluster rate is recorded with MPX11 which is located on the cavern wall USA HS (level 4 – side A, see Tab. 1). The highest number of MIP cluster rate is recorded with MPX15 (closest to the beam axis, along LUCID).

MPX15, MPX14 and MPX01 are recording a much higher MIP cluster rate than other ATLAS-MPX devices (see Tab 9). The number of recognized MIP tracks depends on the ATLAS-MPX detector orientation and position with respect to the beam axis. Being closer to the beam axis, MPX01, MPX14 and MPX15 are sensitive to MIPs produced from the interaction point.

For comparison, Fig. 35b shows the distribution of muons calculated with MC-2003 simulations. Similarly to HETP particles, only a rough comparison of measured MIP cluster rates with simulated data can be done because the MIPs measured with ATLAS-MPX detectors consist of all ionizing particles which create a thin straight track in the detector with a 20 pixel length (see section A.1.1). The "thin track" means that the deposited energy is at maximum several tens of keV per pixel, i.e., high energy protons can be registered as MIPs as well. The summary at the beginning of this section lists simulated particles to be recognized as MIPs.

As seen from Tab 9, there is a significant difference between simulation and measurement of MIPs current. The discrepancy will be further studied with detailed Monte Carlo simulations of response of ATLAS-MPX device. Data presented in Tab. 9 are visualized in Fig. 36. Measurement uncertainty in Tab. 9 expresses the dispersion of the individual values of MIP cluster rate around the mean and it is calculated according to a procedure described in Appendix F. In any case it should not be confused with the measurement statistical uncertainty during collisions which varies between 0.1% and 0.5% for all MPX devices except MPX11 and MPX16 where it reaches to 0.9% and 5.5%, respectively.

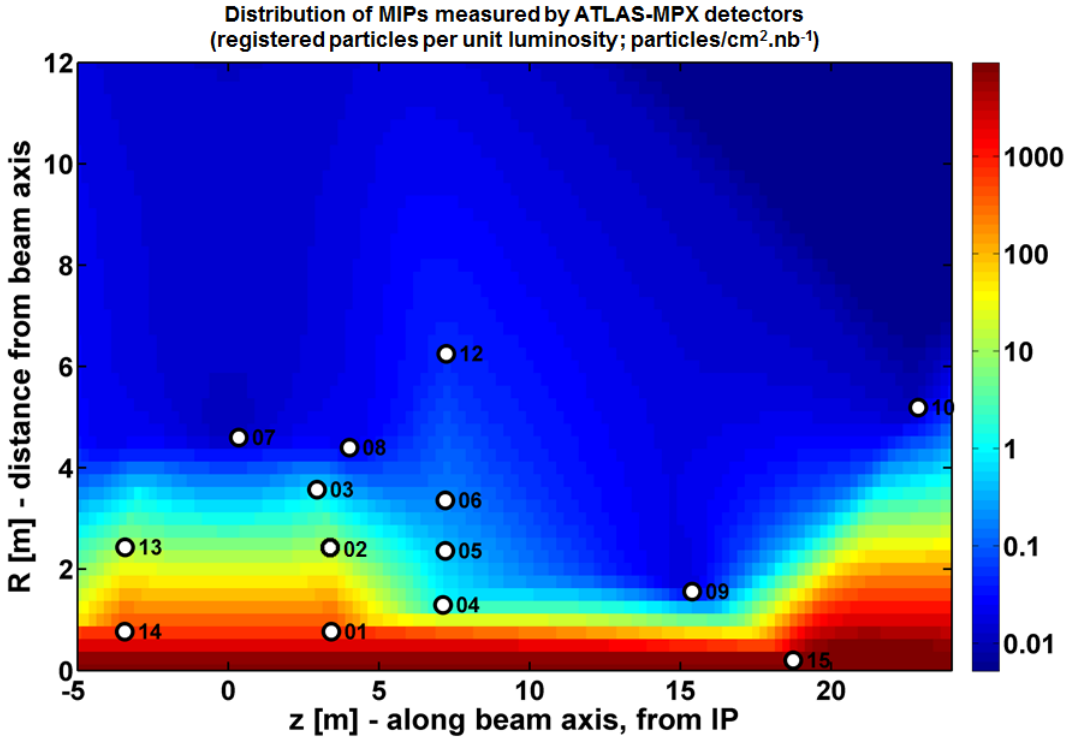

a)

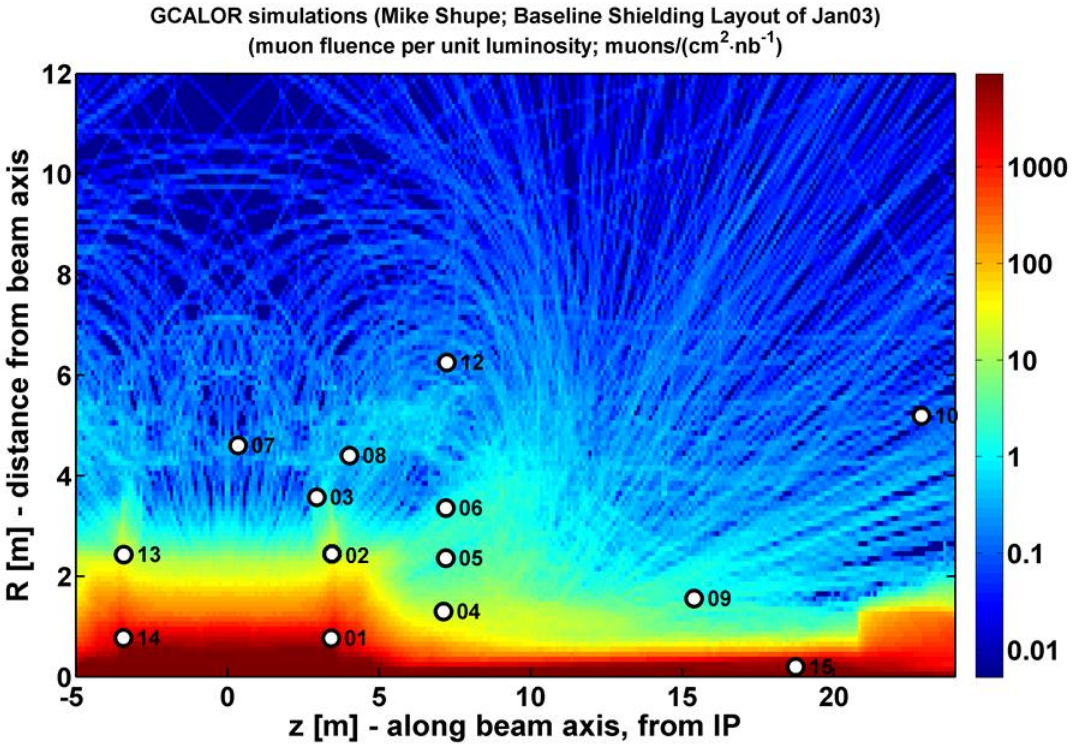

b)

Figure 35. a) Spatial distribution of MIPs interpolated from data obtained from ATLAS-MPX measurements. b) Calculated spatial distribution of muons (MC-2003 simulations). MPX11 is not shown on the figure as its coordinates (Z = 4.86 m, R = 16.69 m) do not match the y-scale used for the display of the simulated distribution of muons.

Detector	ATLAS-MPX average MIP background cluster rate per second [$cm^{-2}.s^{-1}$]	ATLAS-MPX average MIP collision cluster rate per unit luminosity [cm^{-2}/nb^{-1}]	MC-2010 MIP collision current per unit luminosity [cm^{-2}/nb^{-1}] *	Ratio MC-2010 / ATLAS-MPX
MPX01	(5.94 ± 0.18) E-5	(1.21 ± 0.28) E+03	(2.98 ± 0.07) E+02	0.25 ± 0.06
MPX02	(9.27 ± 0.22) E-5	(9.61 ± 0.84)	(6.26 ± 0.70)	0.65 ± 0.09
MPX03	(4.09 ± 0.12) E-5	(9.03 ± 0.54) E-01	(1.52 ± 0.87)	1.68 ± 0.97
MPX04	(3.98 ± 0.12) E-5	(1.55 ± 0.07)	(3.16 ± 3.16) E-02	0.02 ± 0.02
MPX05	(4.24 ± 0.12) E-5	(5.05 ± 0.30) E-01	-	-
MPX06	(4.21 ± 0.12) E-5	(2.30 ± 0.14) E-01	(8.73 ± 8.73) E-03	0.04 ± 0.04
MPX07	(1.33 ± 0.06) E-5	(9.77 ± 0.53) E-03	(1.18 ± 0.31) E-02	1.21 ± 0.32
MPX08	(4.73 ± 0.12) E-5	(1.48 ± 0.09) E-02	(1.72 ± 0.40) E-02	1.16 ± 0.28
MPX09	(6.78 ± 1.52) E-7	(2.52 ± 0.25) E-01	(1.06 ± 0.73) E-02	0.04 ± 0.03
MPX10	(3.16 ± 0.10) E-5	(9.11 ± 0.62) E-03	(3.74 ± 1.91) E-03	0.41 ± 0.21
MPX11	(5.39 ± 0.13) E-5	(2.46 ± 0.21) E-03	-	-
MPX12	(5.71 ± 0.13) E-5	(5.58 ± 0.31) E-02	(1.05 ± 0.25) E-02	0.19 ± 0.05
MPX13	(3.61 ± 0.12) E-5	(1.47 ± 0.04) E+01	(6.26 ± 0.70)	0.43 ± 0.05
MPX14	(3.98 ± 0.19) E-5	(1.03 ± 0.16) E+03	(2.98 ± 0.07) E+02	0.29 ± 0.04
MPX15	(6.79 ± 0.27) E-5	(1.57 ± 0.34) E+04	(7.43 ± 0.78) E+02	0.05 ± 0.01
MPX16	(1.74 ± 0.07) E-5	(3.54 ± 1.46) E-05	-	-

* pp inelastic cross section of 71 mb assumed [13]

Table 9. Average background MIP cluster rate (no collisions period) and the average MIP cluster rate per unit luminosity during collisions as measured by ATLAS-MPX detectors. The average background MIP cluster rates are calculated from all measurements done in 2010. The MIP collision cluster rates were determined from runs in 2011 (except for MPX01, MPX14 and MPX15 operating in high threshold in 2011). The statistical uncertainty of the measurement during collisions varies between 0.1 and 0.5% for MPX01 - MPX15 for all MPX devices except MPX11 and MPX16 where it reaches 0.9% and 5.5%, respectively. For comparison, MC-2010 calculated MIP currents are stated as well. Values from MC simulation include electrons, muons, pions, charged kaons and protons with the angle between the direction vector and sensor normal inside the interval <75°,105°>, corresponding to track length of 20 pixels in the sensor. The particles minimum energy was 0, 25, 32, 110, and 200 MeV, respectively. See Appendices F, G and H for details on the determination of measured and simulated values and their uncertainties presented in this table.

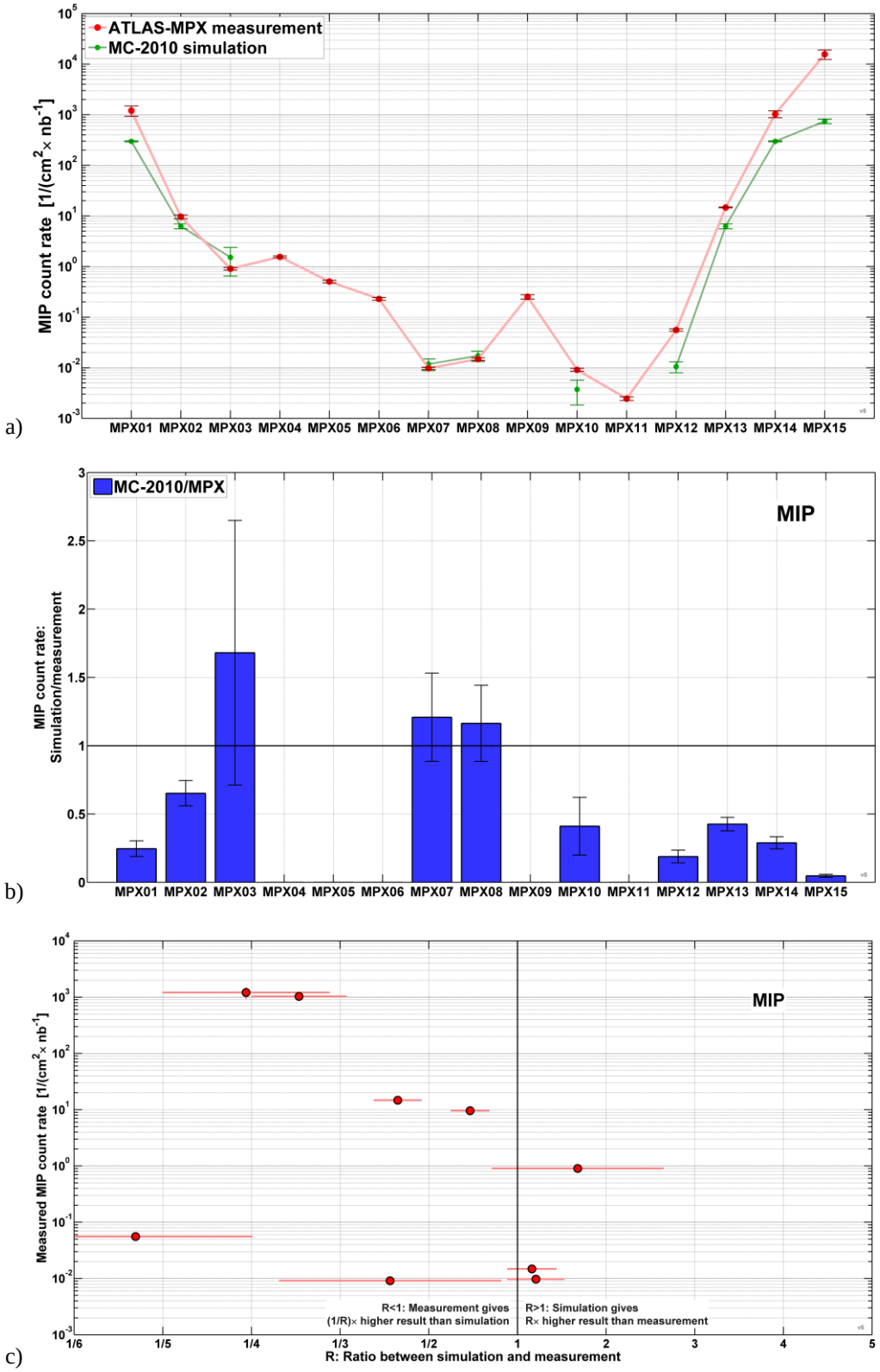

Figure 36. a) Measured (red) and MC-2010 simulated (green) MIP count rates during collisions at all ATLAS-MPX positions. b) Ratio of simulated and measured MIP count rates at all ATLAS-MPX positions. c) Measured MIP count rate plotted against the corresponding ratio of simulated and measured MIP count rates.

6.5 Thermal neutrons

We have defined thermal neutrons as all neutrons with the energy below 0.5 eV which is the rough energy of so called "cadmium edge", i.e., edge energy for high cross section for neutron capture on ^{113}Cd. Using ^{6}Li the thermal neutrons are detected effectively via charged ions from the nuclear reaction

$$n + {}^{6}Li \rightarrow \alpha\ (2.05\ MeV) + {}^{3}H\ (2.73\ MeV); \quad \sigma\ (25\ meV) = 940\ b$$

in the ATLAS-MPX detector area covered with a ^{6}LiF layer (see Fig. 4). Neutron fields, produced by the interactions of particles with surrounding materials yielded by the collisions of protons, cover a large spectrum of energies, from fast to thermal. However, low A materials (hydrogen, carbon and other light elements) present within the ATLAS detector and its environment give large attenuation on fast neutrons. Thermalization of fast neutrons increases the thermal neutron flux by an amount which depends on the quantity of material present in the environment of a given ATLAS-MPX detector. The lowest thermal neutron flux is recorded with MPX11 which is located far from the beam axis and surrounded with less light material. MPX01, MPX14 and MPX15, close to the beam axis and surrounded by large amount of light materials, are recording a much higher number of thermal neutrons.

A.1.8 Correction of ^{6}Li measured signal to contribution of epithermal neutrons

As described in previous paragraph, ATLAS-MPX detectors register thermal neutrons using nuclear interaction with ^{6}Li. The nucleus disintegrates into two heavy charged particles (triton and alpha particle) which can subsequently enter the sensor chip and cause signal recognized as a heavy blob. Although the n(^{6}Li,T)α interaction cross-section is very high for thermal neutrons, it is not negligible for higher neutron energies and hence the measured signal supposed to be from thermal neutrons can be caused by epithermal and fast neutrons as well (see Fig. 37 for n(^{6}Li,T)α interaction cross-section).

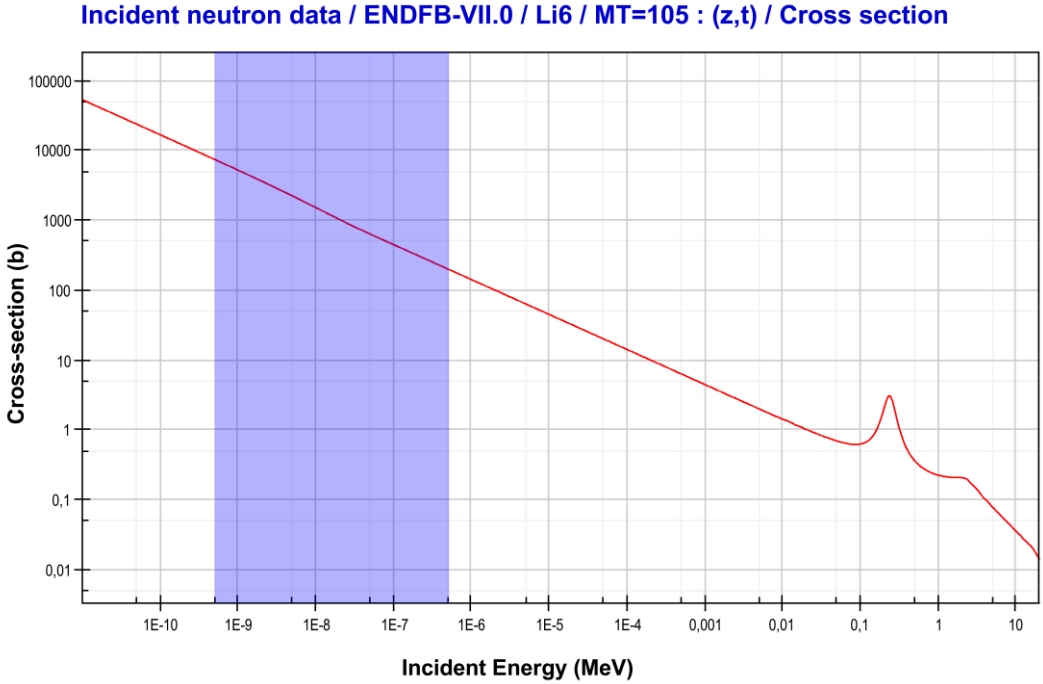

Figure 37. Cross-section for (n,α) interaction on ^{6}Li. Energy region of thermal neutrons (E < 0.5 eV) is highlighted by blue color.

This can cause overestimate of thermal neutron flux especially in untypical neutron fields where the thermal component is missing or it significantly differs from the thermal neutron calibration field used for the ATLAS-MPX detectors calibration (see Appendix B). This case occurs inside the neutron shielding where MPX15 is located (see Fig. 9 and Tab. 1) as can be seen from MC-2010 simulated neutron spectra depicted in Fig. 38.

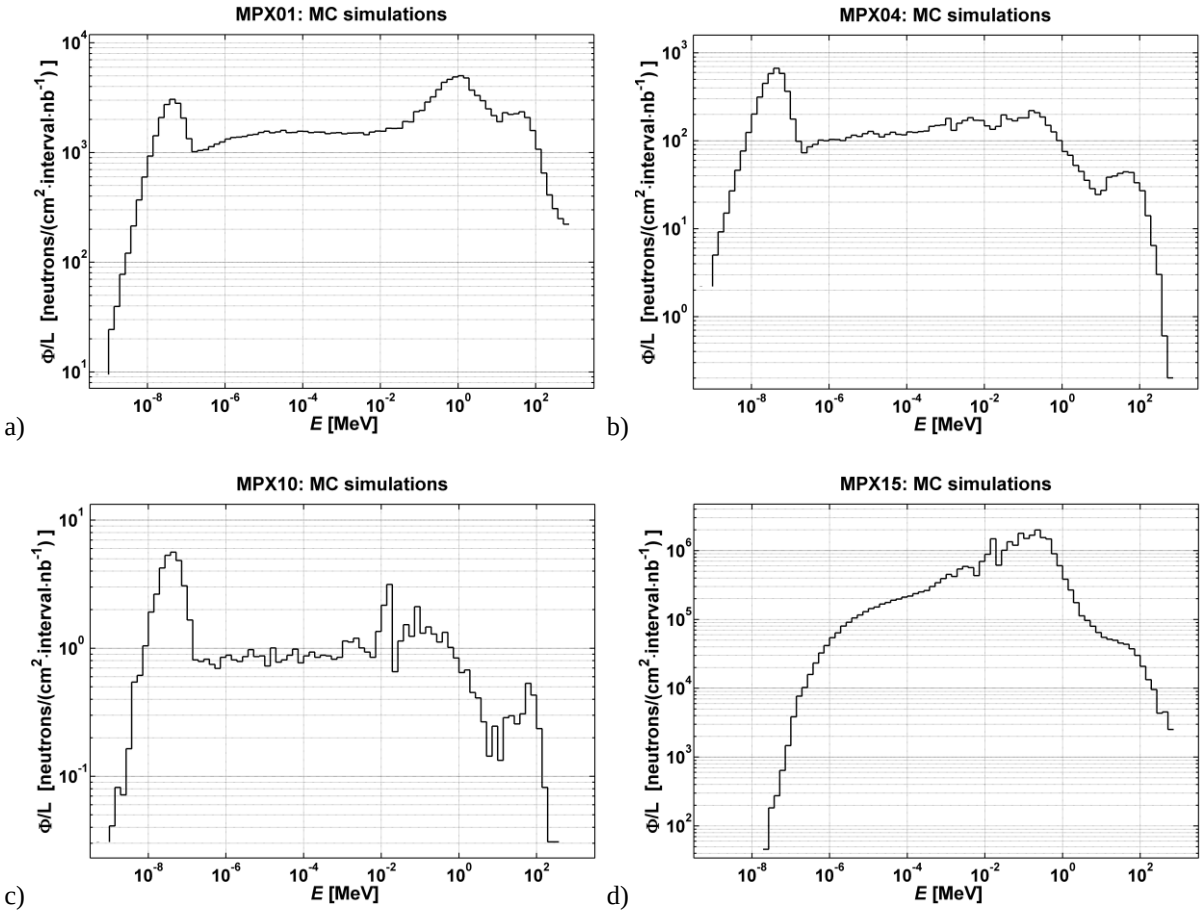

Figure 38. Spectral fluence distribution of neutrons at locations of a) MPX01, b) MPX04, c) MPX10 and d) MPX15 obtained from MC-2010 simulations. y-axis is normalized to the integrated unit luminosity. It can be seen that with increasing distance from the interaction point (MPX01 – MPX04 – MPX10) the thermal neutron component of the spectra is increasing while the fast neutron component decreases (relatively). For the MPX15 position the fast component of the neutron spectrum is dominating contrary to what is observed in the other MPX positions.

Correction of the measured thermal neutron fluxes to the signal caused by non-thermal neutrons was performed using resonance integrals. The correction is at level of 4 – 10% for all ATLAS-MPX detectors except for MPX15 where the correction reaches 90%. Details on calculation of this correction can be found in Appendix E.

A.1.9 Correction to thermal neutron field anisotropy

Response of ATLAS-MPX detectors to thermal neutrons was calibrated in isotropic thermal neutron calibration field (see subsection 2.3). However, according to MC-2010 simulations there are not fully isotropic fields of thermal neutrons at positions of MPX detectors. The anisotropy is caused by huge amount of different materials in ATLAS and a position of MPX detectors very close to concrete walls, cable trays, or other massive objects. The procedure of determination of this correction is described in Appendix H. The correction varies between the factor of 0.79 (i.e., the correct value of flux is lower) and 1.04 (i.e., the correct value of flux is higher).

A.1.10 Spatial distribution of thermal neutrons

The average thermal neutron fluences per unit luminosity during collisions were measured by each ATLAS-MPX detector. Measured spatial distribution of thermal neutron fluence is shown in Fig. 39 as a function of the distance R from the beam axis and the coordinate Z along the beam axis, from the interaction point (IP1) together with the distribution calculated from MC-2010 simulations.

Table 10 summarizes the results of thermal neutron flux measurements. It can be seen that the background neutron flux of nearly all detectors is not statistically distinguishable from zero. The only exception is MPX04 accidentally contaminated at one single point of the sensor chip by an alpha-emitter with long half-life. Hence the increased background of this detector is not related to the outer influence. The comparison with MC-2010 Monte Carlo simulations shows a good agreement within a factor of two. Higher deviations are observed in the low radiation regions of the cavern (MPX07 and MPX11) where the measured thermal neutron flux is found to be lower than simulated. The added JM and JF neutron shielding may explain this reduction.

Measurement uncertainty in Tab. 10 expresses the dispersion of the individual values of measured thermal neutron fluence around the mean and it is calculated according to a procedure described in Appendix F. In any case this uncertainty should not be confused with the measurement statistical uncertainty which varies between 0.1% and 0.5% for all detectors except for MPX11, MPX01, MPX14 and MPX15 where the uncertainty rises to 0.9%, 1.7%, 1.2%, and 6.6%, respectively.

The comparison of thermal neutron fluence measurements and simulation is also shown in Fig. 40.

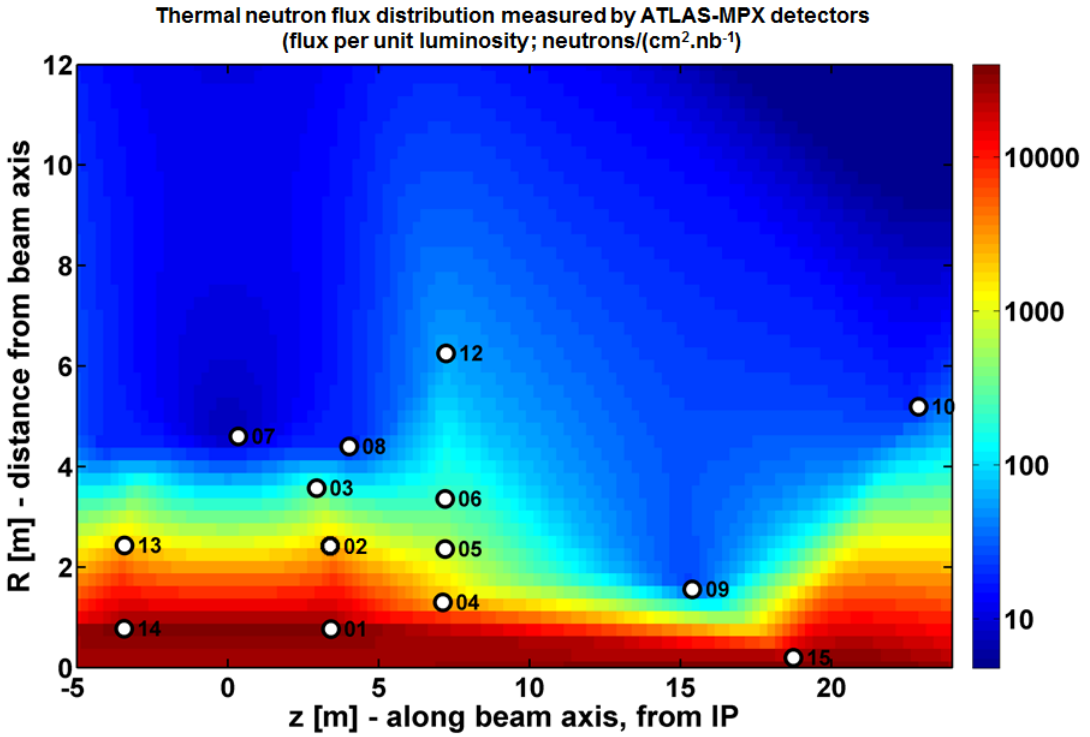

a)

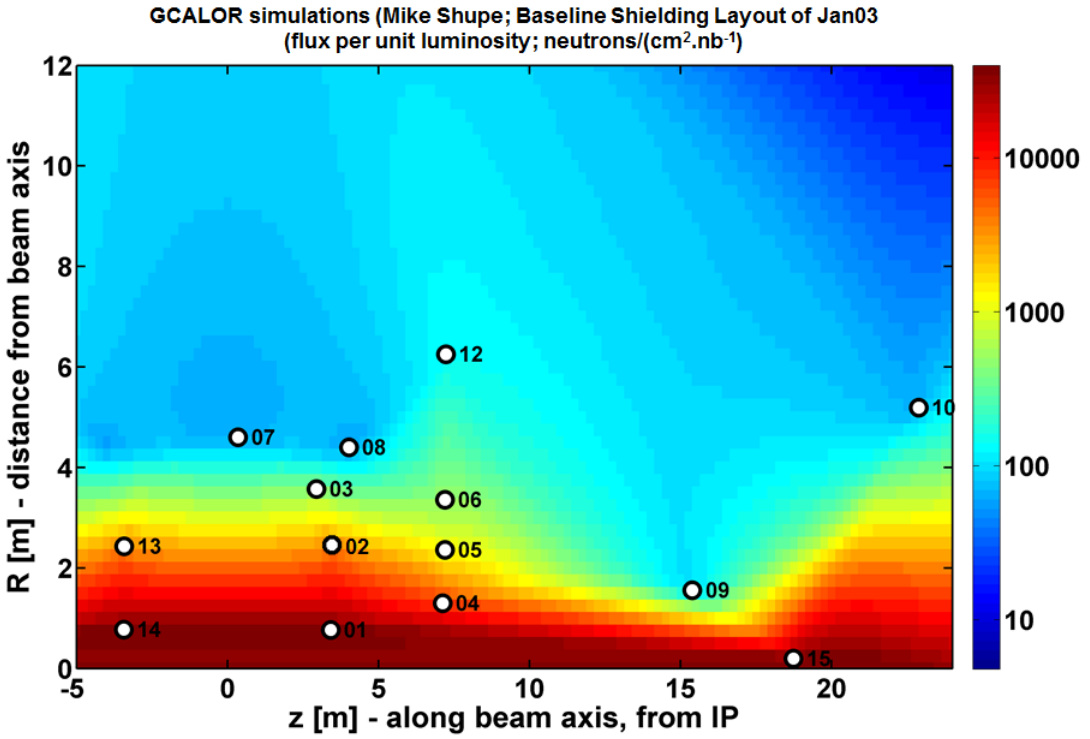

b)

Figure 39. a) Spatial distribution of thermal neutron fluence per unit luminosity interpolated from data obtained from ATLAS-MPX measurements. b) Spatial distribution of thermal neutron fluence per unit luminosity as calculated from MC-2010 simulations. The detector MPX11 is not shown on the figure as its coordinates (Z = 4.86 m, R = 16.69 m) do not match the y-scale used for the display of the simulated distribution of thermal neutrons.

Detector	ATLAS-MPX average thermal neutron background flux [$cm^{-2}.s^{-1}$]	ATLAS-MPX average collision thermal neutron fluence per unit luminosity [cm^{-2}/nb^{-1}] *	MC-2010 thermal neutron fluence per unit luminosity [cm^{-2}/nb^{-1}] **	Ratio MC-2010 / ATLAS-MPX	Resonance integral correction of raw measured data	Anisotropy correction of raw measured data
MPX01	(1.4 ± 2.7) E-02	(3.33 ± 0.58) E+04	(2.97 ± 0.01) E+04	0.89 ± 0.15	-10%	-21%
MPX02	(-1.7 ± 3.7) E-03	(1.66 ± 0.15) E+03	(2.95 ± 0.02) E+03	1.78 ± 0.16	-8%	2%
MPX03	(-3.4 ± 2.9) E-03	(2.45 ± 0.16) E+02	(3.42 ± 0.06) E+02	1.40 ± 0.10	-5%	-9%
MPX04	(-3.7 ± 0.2) E-01[#]	(3.40 ± 0.08) E+03	(5.54 ± 0.04) E+03	1.63 ± 0.04	-4%	4%
MPX05	(2.5 ± 2.0) E-03	(6.87 ± 0.27) E+02	(7.75 ± 0.10) E+02	1.13 ± 0.05	-8%	-6%
MPX06	(-0.6 ± 2.2) E-03	(1.81 ± 0.06) E+02	(3.99 ± 0.07) E+02	2.21 ± 0.09	-10%	-12%
MPX07	(2.2 ± 1.5) E-03	(6.02 ± 0.37)	(4.76 ± 0.09) E+01	7.90 ± 0.50	-9%	-5%
MPX08	(-1.4 ± 1.2) E-03	(1.66 ± 0.06) E+01	(4.31 ± 0.09) E+01	2.59 ± 0.10	-10%	4%
MPX09	(-2.5 ± 1.4) E-03	(2.56 ± 0.19) E+01	(7.39 ± 0.19) E+01	2.88 ± 0.23	-5%	-10%
MPX10	(-0.5 ± 1.8) E-03	(1.77 ± 0.07) E+01	(4.85 ± 0.08) E+01	2.74 ± 0.11	-4%	-11%
MPX11	(-1.8 ± 2.3) E-03	(2.82 ± 0.27)	(7.05 ± 0.06) E+01	24.98 ± 2.38	-4%	-2%
MPX12	(-2.2 ± 1.4) E-03	(6.24 ± 0.21) E+01	(1.07 ± 0.01) E+02	1.72 ± 0.06	-8%	3%
MPX13	(5.9 ± 4.4) E-03	(2.75 ± 0.11) E+03	(2.95 ± 0.02) E+03	1.07 ± 0.04	-8%	2%
MPX14	(1.2 ± 1.2) E-02	(2.93 ± 0.86) E+04	(2.97 ± 0.01) E+04	1.01 ± 0.30	-10%	-21%
MPX15	(6.7 ± 2.4) E-02	(1.85 ± 0.58) E+04	(5.39 ± 0.19) E+04	2.91 ± 0.91	-90%	-11%
MPX16	(1.0 ± 1.8) E-03	(1.12 ± 0.67) E-02	-	-		

* including resonance integral correction and anisotropy correction obtained from MC-2010 simulated data
** pp inelastic cross section of 71 mb assumed [13]
[#] The detector is accidentally contaminated at one single point of the sensor chip by an alpha-emitter with long half-life.

Table 10. Average background thermal neutron flux and average thermal neutron fluence per unit luminosity during collisions as measured by ATLAS-MPX detectors and comparison with MC-2010 simulations. The background thermal neutron fluxes are calculated from all measurements done in 2010. The collision thermal neutron fluences were determined from runs in 2011 (except for MPX01, MPX14 and MPX15 operating at high threshold in 2011). See Appendices F, G and H for details on determination of measured and simulated values and their uncertainties presented in this table. The statistical uncertainty of the measurement during collisions varies between 0.1 and 0.5% for all detectors except for MPX11, MPX01, MPX14 and MPX15 where the uncertainty rises to 0.9%, 1.7%, 1.2%, and 6.6%, respectively.

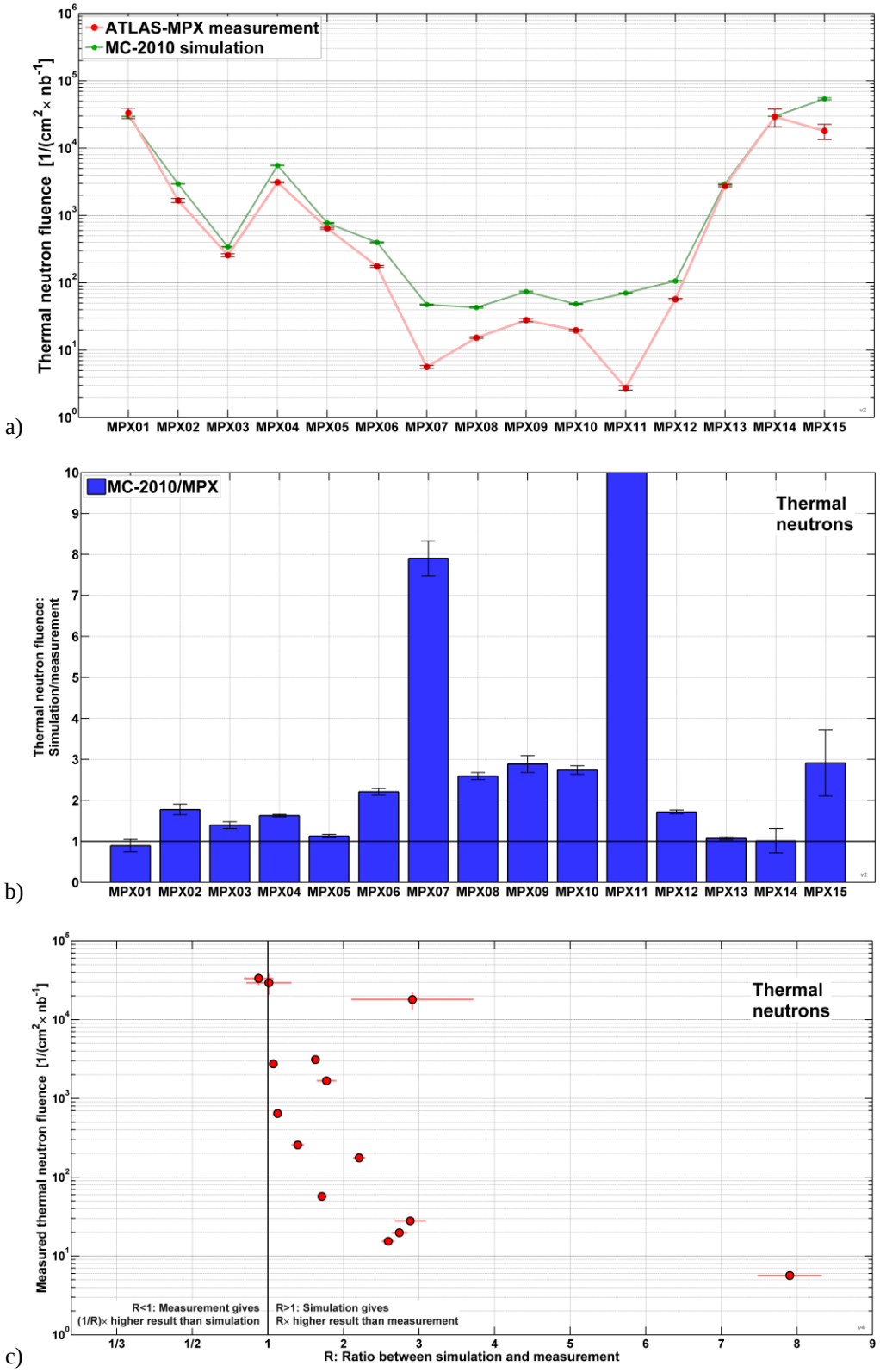

Figure 40. a) Thermal neutron fluence per unit luminosity at every MPX position as calculated by MC-2010 simulations (green) and measured by the ATLAS-MPX network (red). b) Ratio of thermal neutron fluence per unit luminosity calculated by MC-2010 simulations and measured by the ATLAS-MPX network. c) Measured thermal neutrons fluence plotted against the corresponding ratio of simulated and measured thermal neutron fluence.

7. Conclusions and outlook

The ATLAS-MPX network has performed real-time measurements of spectral characteristics and composition of the radiation field in the ATLAS detector and its environment. The network of ATLAS-MPX detectors has been running continuously starting from early 2008 (background and cosmic radiation measurements) through the stable LHC operation during the 2010 and 2011 run periods (collision data) up to nowadays. The primary goals of the ATLAS-MPX network was initially to measure the radiation field inside the ATLAS detector volume with focus on neutron field within the ATLAS environment, background radiation in the experimental hall and the detector surroundings and validation of early Monte Carlo predictions about radiation field in ATLAS. During the network operation it appeared that it is possible to observe averaged background from LHC collisions, van der Meer luminosity scans and induced radioactivity in between/after collision.

The residual material activation in the ATLAS environment due to the high particle flux during collisions is measured through the detection of gamma decay of radionuclides produced by the interaction of collision particles with these materials. Comparison with dose rate calibration measurements done with gamma ray sources provides an estimate of a mean photon ambient dose equivalent rate. The induced activation as measured with an MPX detector is analyzed in terms of short and long decay components with the cluster rate measured after the end of collisions. This analysis exhibits up to four decay components with the following effective half-lives: a few minutes, a few hours, several tens of hours and longer than 50 days.

The measured particle types are separated into four categories: i) particles with low energy transfer (LETP) - electrons, gamma rays, X-rays; ii) particles with high energy transfer (HETP) - alphas, protons, heavier ions, fast neutrons, iii) MIPs and iv) thermal neutrons, with different types of clusters assigned to each category. The LETP, HETP and MIPs cluster rate and thermal neutron flux during collisions were measured for each ATLAS-MPX detector and normalized per unit luminosity. Results of these measurements obtained with each ATLAS-MPX detector were compared to corresponding output from Monte Carlo.

The LETP comparison shows measured values systematically higher, as documented in Tab. 7. The difference may be caused, e.g., by electron energy cut-off at 800 keV applied in the simulation.

In case of HETP and MIPs the comparison (see Tab. 8 and 9) suffers from the poor statistic of the simulated charged particles at most of the ATLAS-MPX positions further from interaction point. The measured rates of the HETP are systematically below the simulated predictions.

One important task of the ATLAS-MPX detectors network is to determine the neutron component of the mixed radiation field within the ATLAS environment. For the purpose, each detector is covered with a mask of converter materials dividing its area into regions sensitive to the type of neutron (thermal and fast). A ^{6}LiF layer is used for thermal neutrons detection and a polyethylene foil for fast neutrons detection. The spectral composition of the neutron field is obtained by comparing the responses from the different regions. The calibration of the detection efficiency for several energies in the different regions of all devices has been performed with various known fast neutron (^{252}Cf, ^{241}AmBe) and thermal neutron sources, and neutrons produced with a Van de Graaff accelerator beam. The average thermal neutron fluences per unit luminosity during collisions were measured for each ATLAS-MPX detector. Their comparison with Monte Carlo simulations shows a fair agreement within a factor of two. Significant deviations are observed in the low radiation region of the UX15 cavern, where the measured thermal neutron flux is found to be lower than simulated, caused mainly due to insufficient description of simulation model in larger distances from interaction point.

The measurement of fluxes of the main radiation species inside the ATLAS detector volume and environment, in particular fast neutrons and photons with ATLAS-MPX detectors, produce 2D maps

of fluences and doses for a given integrated luminosity. Such a measurement will possibly allow the calculation of the safety factors to be used in the future to determine the viability of the ATLAS electronics exposed to growing fluences and doses of neutrons and photons, in particular in view of contemplated beam energy and luminosity upgrades. However, such a calculation requires the measurement of fast neutrons fluxes in absolute value and distinguishing forward from backward moving neutrons at a given ATLAS-MPX detector position which will be considered for the network upgrade.

The correlation established between clusters rate of each radiation species recorded in each ATLAS-MPX detector at a given time and the LHC machine luminosity gives the ATLAS-MPX detectors the capability of bringing real-time information on beam conditions and to directly visualize any beam manipulation including beam set-up, adjustment, and particularly luminosity scans performed according the van der Meer method. The measurement of the effective sizes of the overlapping beams and maximum collision rate are obtained from ATLAS-MPX detectors which are continuously recording cluster rates during the van der Meer horizontal and vertical scans. The count rates measured as a function of time give bell-shaped curves with their maximum achieved at a time corresponding to zero beam separation. For all ATLAS-MPX detectors considered for van der Meer luminosity scan measurement, a Gaussian and a constant background is used to fit the cluster rates measured during the van der Meer luminosity transverse scans. Application of this fit procedure, gives values of the effective horizontal (Σ_x) and vertical (Σ_y) profiles (translated into microns) of the overlapping beams.

On-line measurements of the radiation field will also contribute to estimates of Single Event Upsets (SEU) possibly affecting the electronic devices and control functions operating in the ATLAS experiment environment. An increasing rate of radiation induced failures is observed as the machine peak luminosity increases. For instance, Single Event Effects (SEE) failure are now in 2011 claimed to be the dominant cause of beam dumps (estimate of 1 SEE dump per 60 pb^{-1}) [15]. At the present stage of our study, what we call abnormal events are observed with ATLAS-MPX detectors. These events appear as saturated pixels. Some of SEE could be catalogued as events showing up at pixel locations varying in time, other are due to dead pixel channels with location fixed in time or occasional large overlaps of tracks with location varying in time. Further study is being done to separate events candidates for SEE from other types of abnormal events.

Removal of ambiguity between energetic protons and neutron signals, better determination of the direction of entering MIPs on a sensor area and discrimination of orthogonally incident MIPs from low energy electrons and photons can be possibly achieved by adding Timepix detectors [16] to the network of ATLAS-MPX detectors. The Timepix detector with its Time-Over-Threshold (TOT) capability is analogous to a Wilkinson type ADC and allows direct energy measurement in each pixel. It will possibly provide measurement of absolute fluxes of fast neutrons and allow distinguishing directionality (backward from forward) of neutron motion at their position. This upgraded network will contribute further to estimates of SEE effects affecting the ATLAS and LHC machine electronic devices. The Timepix detectors positioned close to Tile and Liquid Argon calorimeters could provide measurement of the missing transverse energy and study of hadron leakage into the muon detector system. In addition, an increase of the data readout speed by factor of 50 is foreseen [17], thus reducing the measurements dead time significantly. This improved readout system will use a single-wire communication, simplifying the present cable structure.

Acknowledgements

We would like to express our gratitude and thanks to Sergei Malyukov, Siegfried Wenig, Tatiana Klioutchnikova and Stefan Valkar for their valuable help during the installation of the ATLAS-MPX network at CERN. Also we thank to Dzmitry Maneuski, Val O'Shea, Dominic Greiffenberg, Michael Fiederle, Miroslav Kralik and Vladimir Sochor for their help with the detector calibrations. Very important input was provided to us by Mike Shupe for the comparison of our measurements with the simulations. Our thanks also belong to Lukas Tlustos, Jan Jakubek, Cestmir Kuca, Ian Dawson and Vincent Hedberg for their help.

It would not be possible to realize this large project without the contribution of the authors of the project proposal [1] and technical note [2] as well as their mother institutions (Czech Technical University in Prague, Charles University in Prague, CERN, Glasgow University, University of Montreal, NIKHEF, FMF Freiburg) which supported the project from the beginning.

The project was supported by the Ministry of Education, Youth and Sports of Czech Republic under projects no. MSM68400029 and LA0032. The Group of the Université de Montréal thanks the support of the Natural Sciences and Engineering Research Council of Canada (NSERC).

Bibliographic references

[1] M. Campbell, C. Leroy, S. Pospisil, M. Suk, *Measurement of Spectral Characteristics and Composition of Radiation in ATLAS by MEDIPIX2-USB Devices*, Project proposal, 2006. Available at https://edms.cern.ch/document/815615

[2] T. Holy, J. Jakubek, S. Pospisil, J. Uher, Z. Vykydal, Z. Dolezal, M. Suk, I. Wilhelm, M. Campbell, E. Heijne, X. Lopart, L. Tlustos, C. Leroy, B. Mikulec, M. Nessi, C. Buttar, V. O'Shea, K.M. Smith, *Proposal to measure spectral characteristics and composition of radiation in ATLAS by MEDIPIX2-USB Devices*, Project technical note, 2006. Available at https://edms.cern.ch/document/815615

[3] CERN Medipix2 collaboration at http://www.cern.ch/medipix.

[4] X. Llopart, M. Campbell, R. Dinapoli, D. San Segundo and E. Pernigotti, *Medipix2: a 64-k Pixel Readout Chip With 55-μm Square Elements Working in Single Photon Counting Mode*, IEEE Transactions on Nuclear Science, Vol. 49, 2002. doi:10.1109/TNS.2002.803788

[5] Z. Vykydal, *Evaluation of Radiation Field Properties with Pixel Semiconductor Detectors Operating in Particle Tracking Mode*, Doctoral thesis, Albert-Ludwigs-University in Freiburg, 2012

[6] S. Pospisil, B. Sopko, E. Havrankova, Z. Janout, J. Konicek, I. Macha and J. Pavlu, *Si Diode as a Small Detector of Slow Neutrons*, Radiation Protection Dosimetry, Vol. 46, 1993. Available at http://rpd.oxfordjournals.org/content/46/2/115

[7] S. Pospisil, *Spectrometry of fast neutrons using recoiled proton method in semiconductor detectors*, Diploma thesis (in Czech), Czech Technical University in Prague, 1964.

[8] Operation page of the ATLAS-MPX network measurements at http://www.cern.ch/Atlas.

[9] The ATLAS Collaboration, *Luminosity Determination in pp Collisions at $\sqrt{s}$ = 7 TeV Using the ATLAS Detector at the LHC*, Eur. Phys. J. C, Vol. 71, 2011. doi:10.1140/epjc/s10052-011-1630-5

[10] M. Tibbetts, *First Look at May σ LUCID Fits*, Presentation, 19th May 2011.

[11] Radiation Background Task Force, *Predicted Radiation levels in ATLAS*, Available at http://atlas.web.cern.ch/Atlas/GROUPS/PHYSICS/RADIATION/Radiation_Levels.html

[12] M. Shupe, private communication, 2010.

[13] K. Goulianos, *Diffraction, Saturation and pp Cross Sections at the LHC*, arXiv:1105.4916v2 [hep-ph] Mar 2011.

[14] X-5 Monte Carlo Team, *MCNP - A General Monte Carlo N-Particle Transport Code, Version 5 - Volume I: Overview and Theory*, LA-UR-03-1987, Los Alamos National Laboratory, revised 2/2008 (2008).

[15] Giulia Papotti, *LHC Status and Performance in 2011*, Proceedings of the 13th ICATPP Conference, Villa Olmo, Como, Editors S. Giani et al, World Scientific, Singapore, 2012. ISBN: 978-981-4405-06-5

[16] X. Llopart, R. Ballabriga, M. Campbell, L. Tlustos, W. Wong, *Timepix, a 65k programmable pixel readout chip for arrival time, energy and/or photon counting measurements*, Nuclear Instruments and Methods A, Vol. 581, 2007. doi:10.1016/j.nima.2007.08.079

[17] V. Kraus, M. Holik, J. Jakubek, M. Kroupa, P. Soukup, Z. Vykydal, *FITPix - Fast Interface for Timepix Pixel Detectors*, Journal of Instrumentation 6 C01079, 2011. doi:10.1088/1748-0221/6/01/C01079

[18] Z. Vykydal, J. Bouchami, M. Campbell, Z. Dolezal, M. Fiederle, D. Greiffenberg, A. Gutierrez, E. Heijne, T. Holy, J. Idarraga, J. Jakubek, V. Kral, M. Kralik, C. Lebel, C. Leroy, X. Llopart, D. Maneuski, M. Nessi, V. O'Shea, M. Platkevic, S. Pospisil, V. Sochor, J. Solc, M. Suk, L. Tlustos, P. Vichoudis, J. Visschers, I. Wilhelm, J. Zemlicka, *Evaluation of the ATLAS-MPX Devices for Neutron Field Spectral Composition Measurement in the ATLAS Experiment*, 2008 IEEE Nuclear Science Symposium Conference Record, 2009. doi:10.1109/NSSMIC.2008.4774829

[19] S. Baranov, M. Bosman, I. Dawson, V. Hedberg, A. Nisati and M. Shupe, *Estimation of Radiation Background Impact on Detectors, Activation and Shielding Optimization in ATLAS*, ATL-GEN-2005-001, 2005. Available at https://cdsweb.cern.ch/record/814823

[20] ICRU Report 85, *Fundamental Quantities and Units for Ionizing Radiation*, Journal of the ICRU, Vol. 11, 2011. doi:10.1093/jicru/ndr012

Appendix A. ATLAS-MPX WEB site user guide

The user can access the ATLAS-MPX web page from the Radiation Monitors option in ATLAS detector operation page [5]. It is possible to select a particular ATLAS-MPX detector, use a browser frame to visualize frames of this given (or any other) detector and finally visualize different cluster types or hits in pixels over a given period of time in a form of a plot.

A.1 Select Device

Select Device page shows the positions of all the detectors within the UX15 cavern. User can click on each detector to select it for access to frames or graphs visualization. By hovering with cursor over the detector, its coordinates (X, Y, Z, R) are shown. The current operation status of all detectors is shown in the table on the right side of the screen (see Fig. 41).

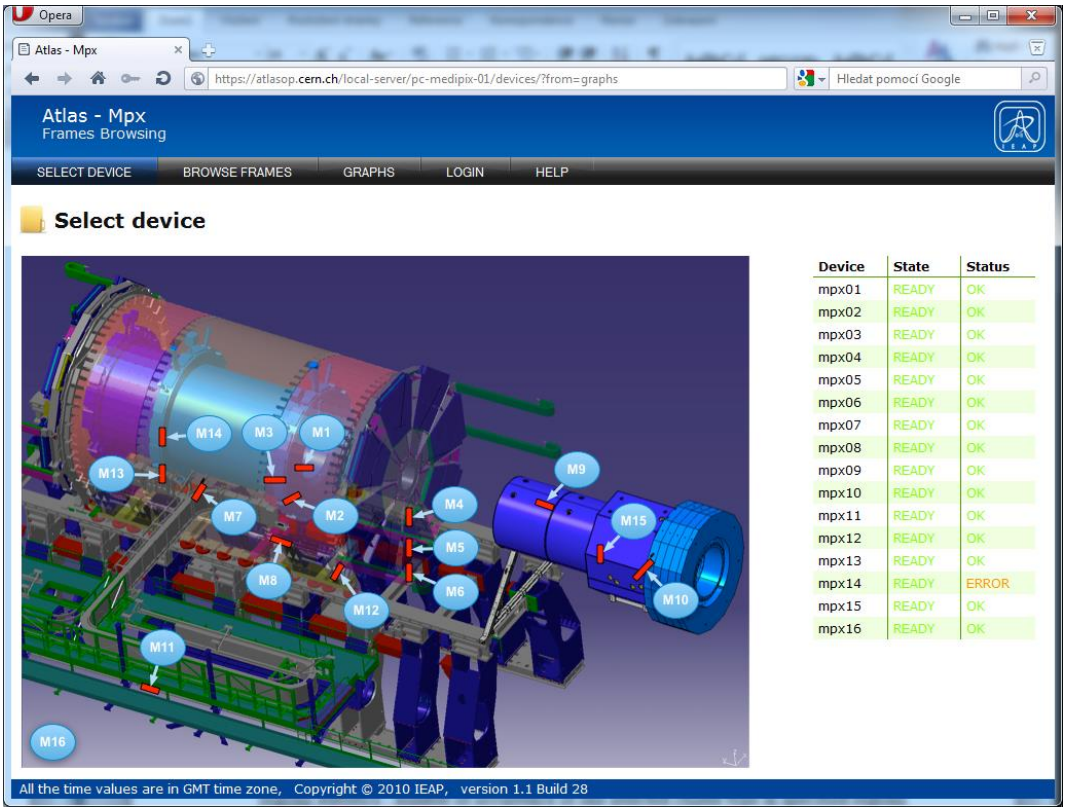

Figure 41. Screen shot from the Select Device page.

A.2 Browse Frames

Browse Frames page (see Fig. 42) is used to visualize single frames. In the detector box, user can change the detector to show frames either by selecting from the list box menu or by clicking on the *Select* link which will take him to *Select Device* page.

In the *Frame* box it is possible to find a particular frame by its date and time or by experiment through clicking on *Data Selection* link and choosing the experiment of interest.

In the *Integral Frame* one can generate integral frames (sum of several consecutive frames). The first frame is specified by date and time (*Date From* and *Time From*) and then the time range needs to be specified in which frames will be summed (*Integr. Time*). Frames can be integrated only within a single experiment. Experiment can be chosen from the *Data Selection* list box menu.

In the *Frame Range*, box use can specify the maximal range of Z axis (counts) in the frame. Browsing through the frames can be achieved by clicking on the *Next* and *Previous* link on top of the frame showing the next and previous frame, respectively. It is also possible to create an animation of frames by clicking on *Start* button in *Animation* box. Every second a next frame will be automatically visualized.

Region Statistics shows the sum of number of hits in pixels in each region. *Cluster Statistics* shows the sum of different cluster types in the current frame (or integral frame). In a case of integral frame, average number per frame is also calculated. In the *Experiment Info* box one can see the basic settings of the device used for the particular experiment.

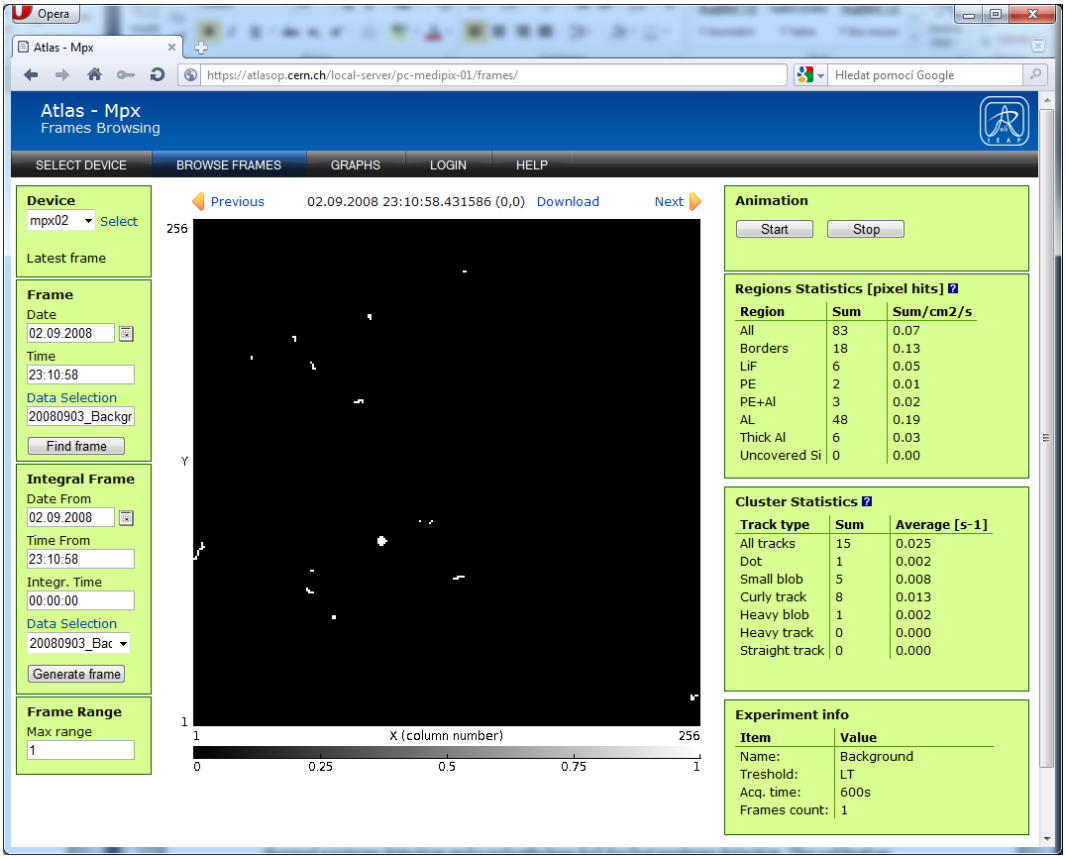

Figure 42. Screen shot from the Browse Frames screen.

A.3 Graphs

This page has the purpose of visualizing different cluster types or hits in pixels over longer period of time in a form of plot (see screen shot in the Fig. 43). The detector whose plot is to be seen can be selected in *Device* list box menu in the same manner as in *Browse Frames* page. There is also the possibility to show quickly plots for last hour, last 24 hours, last week and last month by clicking on the links in *Device* box, respectively. Cluster types that should be visualized in the plot can be selected in *Cluster type* box. Regions that will be included in the plot can be selected in *Regions* box. Time range is specified in the *Time range* box by selecting starting date and time (*From Date* and *From Time*) and end time (*To Date* and *To Time*). In the case there is more experiment in the selected time range user can choose the desired experiment in the *Data Selection* list box menu. When the time range of a whole experiment is needed, the experiment can be selected by clicking on *Data Selection* link and time range is automatically filled with the time range of the experiment. Different graph settings are available in *Graph parameters*:

- *Cluster/Region characteristics* - This switches plotting of the different cluster types in the selected *Regions* (cluster statistic) or number of occurrence of one selected cluster type in specified regions (region statistic).
- *Limit range of "Number of events" in graph* - Limits maximal range of Y axis.
- *Plot counts* - Instead of clusters, pixel hits in the frame are shown.
- *Integral graph* - Integral graph of clusters/pixel hits is plotted in the specified time range.

The *Statistics* box shows sum of different cluster types for the specified time range and average number normalized per second.

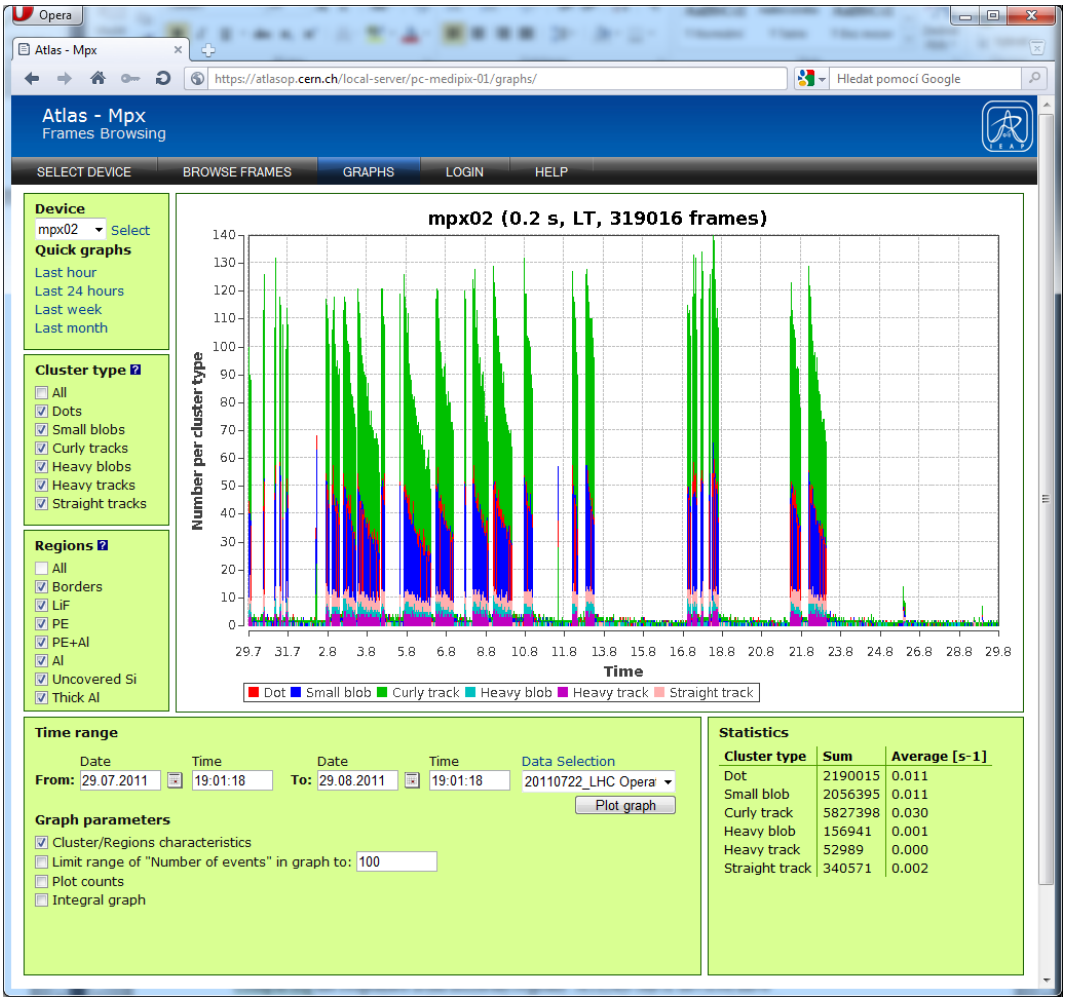

Figure 43. Screen shot from the Graphs screen.

The easiest way to generate a plot in a graph tab is to select the device of interest from the *Device* frame and click on *Last hour*, *Last day* etc. This will generate the default plot. If the parameters of the measurement have been modified (different sets of measured data called "experiments") during the selected time scale, the first one will be displayed and the next one can be displayed by choosing it from the *Data selection* combo box in the *Time range* frame and click on *Plot graph* button.

The assignment of morphological categories (blob, track, etc.) to real particles is displayed as an help text when the cursor is moved over the corresponding check box in the "Cluster type" frame (that is generally the kind of help used over the whole web page but more detailed text to the help tab as well is in preparation). Note that this description is valid only for the low threshold measurements (marked as LT on the graph label).

Noteworthy, the time as given on MPX network web page is the GMT time. However, the time used in text describing results obtained with the MPX network can be CET time, including seasonal time shifts (winter, summer time). Hence, the user should accordingly take into account one or two hour shift in time between MPX network time and current CET time.

A.4 DCS data available in ATLAS Control Room

The ATLAS-MPX page in DCS shows cluster rate in Hz.cm^{-2} (see Fig. 44). In the top part of the image the positions of the detectors are shown together with actual count rate calculated from last measured frame. In the bottom part, two charts show history of count rate in the last 8 hours for detectors MPX01 and MPX15. It is possible to visualize other detectors by selecting the corresponding checkbox in each chart.

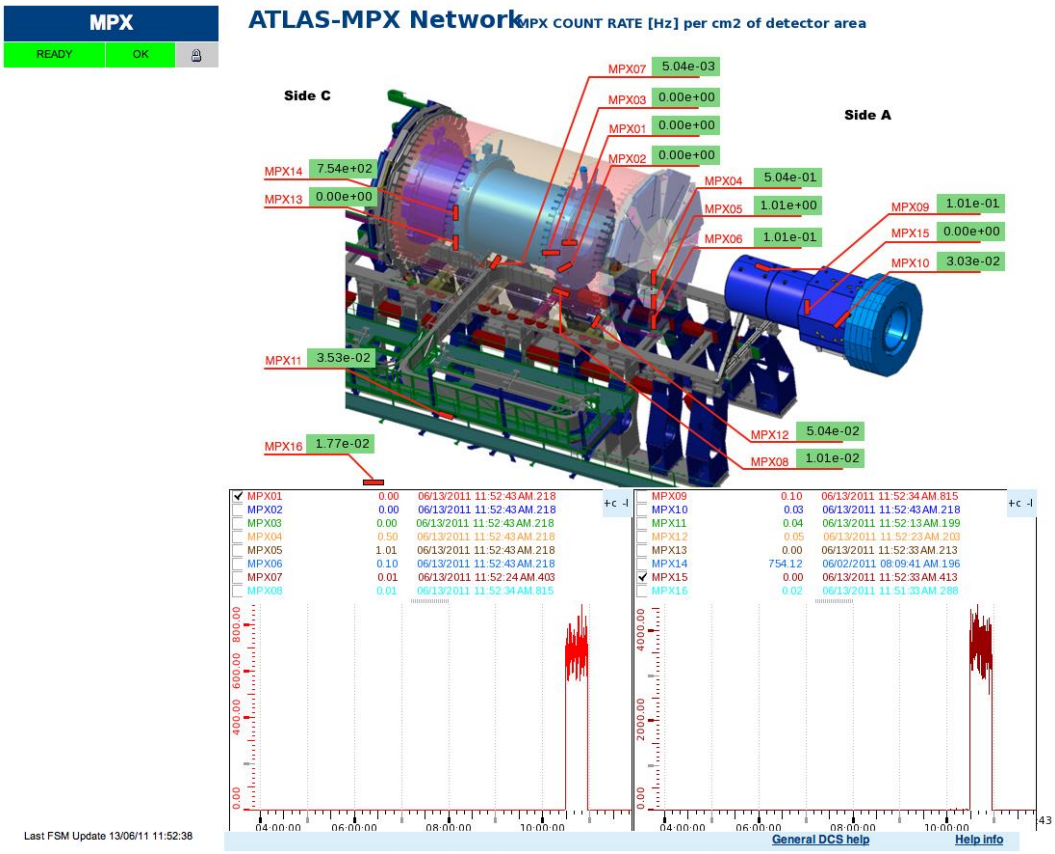

Figure 44. Screen shot of the ATLAS-MPX DCS webpage.

Unfortunately too many different variables prevent sending all the available information to the central ATLAS DCS database. However, the ATLAS-MPX network provides DCS data for each detector, namely:

- CNT_ALL - number of clusters in a frame normalized to 1 second
- FLX_ALL - number of clusters in a frame normalized to 1 second and cm^2
- STG - settings id number
- TIME_STAMP - start time of the frame CNT_ALL and FLX_ALL
- DEV_STATUS - status of the detector

Appendix B. Calibration of the neutron detection efficiency

Detection efficiency for neutrons depends significantly on the geometry of neutron convertors positioning above the sensitive silicon area. Therefore, the efficiency calibration was performed individually for all devices with a set of known neutron sources: thermal neutrons, ^{252}Cf, ^{241}AmBe, 14 MeV neutrons from T(d,n)α reaction in a Van de Graaff accelerator (VDG) [18].

The high threshold (~230 keV) mode of operation was used in order to exclude all clusters induced by light particles in silicon. The insensitivity of the devices was tested with a ^{90}Sr source. The exposure time was set short enough in order to get about 100 clusters per frame. These separated clusters have been identified and counted. The efficiencies have been calculated according to the following equation:

$$\varepsilon_{A-Si} = \frac{\frac{N_A}{S_A} - \frac{N_{Si}}{S_{Si}}}{\Phi . t} \tag{5}$$

where N_A, N_{Si} are detected number of clusters during the whole measurement in region A (^{6}LiF region was used for thermal neutrons, PE region was used for fast neutrons) and for uncovered (Si) region (see Fig. 4b); S_A, S_{Si} are the areas corresponding to these regions; Φ is the incident neutron flux and t is the time of measurement. The following Fig. 45 shows the results of neutron efficiency calibration for all ATLAS-MPX devices (also reference devices) compared to the simulation. Mean values of the efficiency are summarized in Tab. 11.

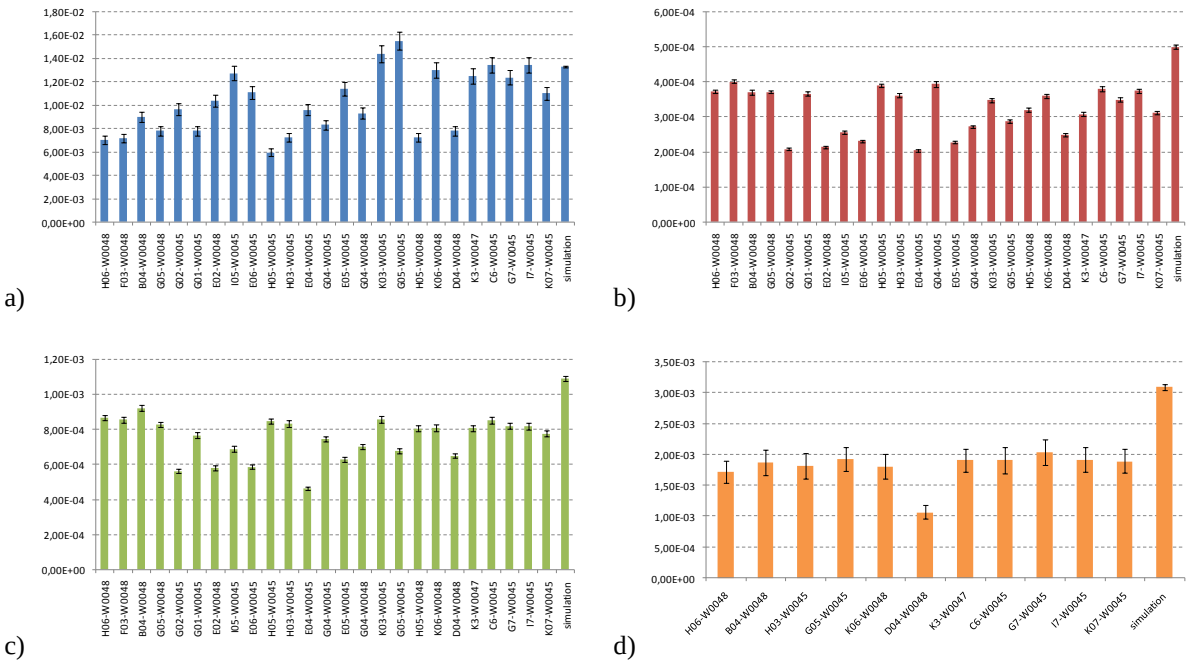

Figure 45. a) Thermal neutron detection efficiencies (^{6}LiF-Si region); mean value 1.02E-2; tolerance 26%. b) ^{252}Cf neutron (mean energy 2.2 MeV) efficiencies (PE-Si region); mean value 3.17E-4; tolerance 21%. c) ^{241}AmBe neutron (mean energy 4.2 MeV) efficiencies (PE-Si region); mean value 7.51E-4; tolerance 16%. d) 14 MeV neutron efficiencies from Van de Graaff accelerator (PE-Si region); mean value 1.81E-3; tolerance 14%. All tolerances are standard tolerance of all calibrated devices.

Source	Mean efficiency	Tolerance*
Thermal neutrons	1.02E-2	26%
^{252}Cf source (mean energy 2.2 MeV)	3.17E-4	21%
^{241}AmBe source (mean energy 4.2 MeV)	7.51E-4	16%
14 MeV neutrons from VDG	1.81E-3	14%

*This means standard tolerance of all calibrated devices.

Table 11. Neutron mean detection efficiency summary.

The cluster ratio between PE and PE+Al regions which brings information about the energy hardness of the incident neutron spectrum (recoiled protons of lower energies are more attenuated in the aluminum layer, see Fig. 7) nicely corresponds to the result of the Monte Carlo simulations (see Fig. 46).

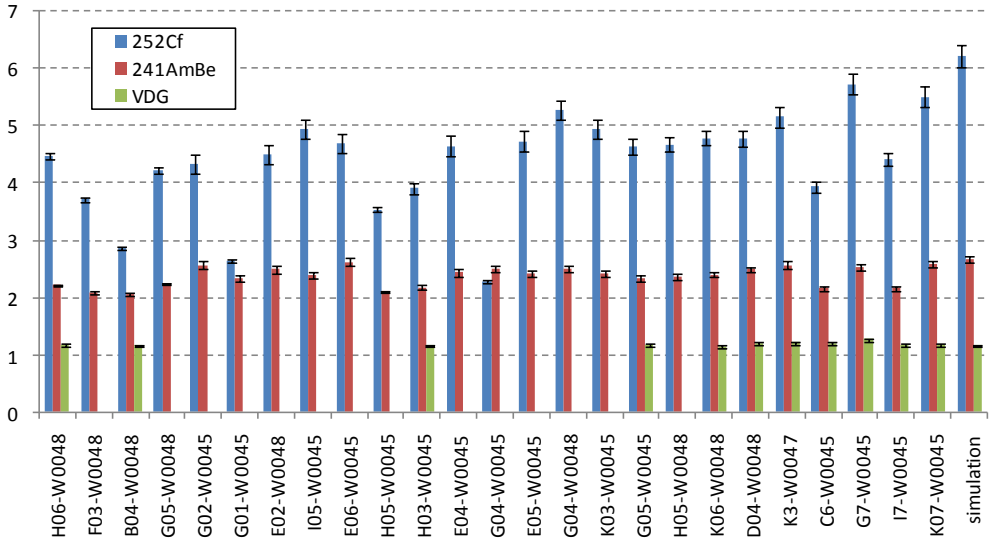

Figure 46. Detected cluster ratio between PE and PE+Al region (see Fig. 4). Mean value for ^{252}Cf is 4.37; tolerance 19%, for ^{241}AmBe it is 2.37; tolerance 7% and for 14 MeV neutrons mean value is 1.19; tolerance 3% (note that not all the devices were calibrated with 14 MeV neutrons).

Despite these promising results we are not able to distinguish fast neutrons from the other high energy transfer particles because the composition of the radiation field inside the ATLAS detector is too different from the field from neutron sources used for the device calibrations.

Appendix C. Analysis of Pb-Pb collisions data in 2010

Collisions of ^{208}Pb ions at a center-of-mass energy per nucleon pair $\sqrt{s_{NN}}$ = 2.76 TeV took place in November 2010. The ATLAS-MPX detectors network was recording data during that period. The results of measurement for four categories of measured particle types (see section 2 for category assignment) are summarized in Tab. 12: average thermal neutrons fluence per unit luminosity and low energy transfer particles (LETP), high energy transfer particles (HETP) and MIP average cluster rate per unit luminosity. The results of detailed analysis will be published separately in a forthcoming report.

MPX detector	**Average thermal neutron fluence per unit luminosity [cm^{-2}/μb^{-1}]**	**Average LETP cluster rate per unit luminosity [cm^{-2}/μb^{-1}]**	**Average HETP cluster rate per unit luminosity [cm^{-2}/μb^{-1}]**	**Average MIP cluster rate per unit luminosity [cm^{-2}/μb^{-1}]**
MPX01	(4.47 ± 0.69) E+05	(5.22 ± 0.22) E+05	(5.43 ± 0.19) E+03	(9.48 ± 0.46) E+03
MPX02	-	-	-	-
MPX03	(2.25 ± 0.97) E+03	(2.81 ± 0.59) E+02	(1.22 ± 0.43) E+01	(9.40 ± 2.56)
MPX04	(9.66 ± 2.72) E+03	(7.82 ± 0.57) E+02	(2.42 ± 0.87) E+01	(9.38 ± 2.45)
MPX05	(4.90 ± 3.26) E+03	(2.77 ± 0.43) E+02	(1.09 ± 0.55) E+01	(4.32 ± 2.02)
MPX06	(2.78 ± 1.41) E+03	(1.43 ± 0.37) E+02	(7.60 ± 4.82)	(4.35 ± 2.01)
MPX07	(5.50 ± 4.77) E+03	(5.43 ± 3.70) E+01	(1.04 ± 0.28) E+01	(2.70 ± 1.03)
MPX08	(2.32 ± 2.16) E+03	(4.72 ± 1.62) E+01	(5.69 ± 4.37)	(3.66 ± 0.85)
MPX09	(1.42 ± 1.61) E+03	(9.90 ± 9.57) E+01	(8.99 ± 7.92)	(7.41 ± 1.05) E+01
MPX10	(1.28 ± 1.55) E+03	(8.34 ± 3.96) E+01	(1.16 ± 0.62) E+01	(2.31 ± 1.67)
MPX11	(2.52 ± 1.99) E+03	(6.59 ± 4.15) E+01	(1.13 ± 0.63) E+01	(3.05 ± 1.56)
MPX12	(8.74 ± 8.32) E+02	(6.08 ± 2.42) E+01	(5.78 ± 2.62)	(3.10 ± 0.87)
MPX13	(2.44 ± 0.91) E+04	(3.47 ± 0.18) E+03	(5.01 ± 0.89) E+01	(1.31 ± 0.17) E+02
MPX14	(3.69 ± 0.35) E+05	(5.12 ± 0.19) E+05	(5.49 ± 0.21) E+03	(8.90 ± 0.51) E+03
MPX15	(8.85 ± 4.48) E+05	(1.49 ± 0.05) E+07	(6.88 ± 1.42) E+04	(9.08 ± 1.11) E+04
MPX16	(8.16 ± 7.75) E+02	(6.16 ± 3.15) E+01	(1.57 ± 0.41) E+01	(2.87 ± 1.27)

Table 12. Summary of ATLAS-MPX measurements during Pb-Pb collisions runs in November 2010.

Appendix D. Quantities and units for ionizing radiation used in this report

D.1 Radiation field quantities

For the description of the radiation field we use physical quantities: *particle current*, *particle fluence* and *particle flux* defined in a similar way done in Appendix II of [19].

Although the nomenclature and definitions differ from the official ones described in ICRU 85 [20], the quantities used in this report are more applicable to the data obtained with a two-dimensional, planar, square pixelated chip of ATLAS-MPX detectors. Furthermore, it allows easier comparison with Monte Carlo calculations.

- *Particle current* - is defined as the number of particles of a given type crossing through a given plane, normalized to the area of this plane and to time unit. The given plane is in our case the MPX sensor chip surface with an area of approximately 2 cm^2.
- *Particle fluence* - is defined as the number of particles of a given type incident on a sphere of cross-sectional area A, normalized to this area A.
- *Particle flux* - is defined as the particle fluence, normalized to time unit. This means that the fluence and flux are independent on particle direction, in contrast to the particle current. Because the MPX sensor chip is not spherical, the particle current obtained from measured cluster rate cannot be recalculated into flux without the knowledge of radiation field anisotropy and ATLAS-MPX device angular response. The only exception is a radiation field of thermalized neutrons which is supposed to be isotropic and therefore identical to the reference field used for ATLAS-MPX detectors calibration.

D.2 Radiation protection quantities

For the description of the ATLAS radiation field for radiation protection purpose, we use the quantity *photon ambient dose equivalent*, H*(10). This measurable quantity used in radiation protection surrogates the effective dose describing the biological effectiveness of the absorbed dose in different human tissues. In this report, H*(10) is used only for quantification of radiation field caused by activation products, i.e., photon radiation, and not mixed radiation field occurring during LHC runs. An ATLAS-MPX device was calibrated in reference photon fields to obtain a conversion from measured cluster rate to photon ambient dose equivalent rate.

Appendix E. Determination of neutron resonance integral

Resonance integrals were used for correction of the measured thermal neutron fluxes (calculated from heavy blob counts below the ^{6}LiF converter) to the signal caused by non-thermal neutrons. The resonance integral is in direct relation to the number of interactions of a given type of neutrons with energies in a given energy interval (e.g., (n,α)). It is calculated as a sum (integral) of a product of neutron flux and the corresponding cross-section (see Eq.1).

$$I_j = c \sum_i \mathrm{N}_{ij} \times \sigma_i \tag{6}$$

where:

I_j resonance integral for detector j

c normalization constant

N_{ij} number of neutrons in i-th energy bin of neutron spectral fluence distribution

σ_i cross section of interaction n(^{6}Li,t)α corresponding to the neutron energy of i-th bin of neutron spectral fluence distribution

Using the cross-section presented in Fig. 37 and neutron spectral fluence distributions obtained from MC-2010 simulations (see section 6.1 and Fig. 38), two resonance integrals were calculated:

- the first one (I_{th}) from 0 to 0.5 eV (energy range of thermal neutrons given by our definition of thermal neutrons – see the introduction to section 6),
- the second one (I_0) from 0 eV to infinity (energy range of all neutrons which could contribute to the measured signal).

The ratio I_{th}/I_0 is ≤ 1. The measured uncorrected thermal neutron flux was multiplied by this ratio to obtain the actual thermal neutron flux. Corrections are summarized in Tab. 13. Note that the correction is at level of 4 - 10% for all ATLAS-MPX detectors except for MPX15 where the correction reaches 90%. The corrected value of the thermal neutron flux at MPX15 is in better agreement with Monte Carlo predictions.

Detector	I_0, Resonance integral over all neutron energies	I_{th}, Resonance integral over thermal neutron energies (E < 0.5 eV)	Resonance integral correction, Ratio I_{th}/I_0	Without correction: Measured thermal neutron fluence per unit luminosity [cm^{-2}/nb^{-1}] *	With correction: Measured thermal neutron fluence per unit luminosity [cm^{-2}/nb^{-1}] *	MC simulated thermal neutron fluence per unit luminosity [cm^{-2}/nb^{-1}] **	Ratio MC/MPX
MPX01	1.19E+07	1.07E+07	0.90	(3.70 ± 0.64) E+04	(3.33 ± 0.58) E+04	(2.97 ± 0.01) E+04	0.89 ± 0.15
MPX02	1.16E+06	1.06E+06	0.92	(1.81 ± 0.17) E+03	(1.66 ± 0.15) E+03	(2.95 ± 0.02) E+03	1.78 ± 0.16
MPX03	1.37E+05	1.31E+05	0.95	(2.58 ± 0.17) E+02	(2.45 ± 0.16) E+02	(3.42 ± 0.06) E+02	1.40 ± 0.10
MPX04	2.25E+06	2.16E+06	0.96	(3.55 ± 0.08) E+03	(3.40 ± 0.08) E+03	(5.54 ± 0.04) E+03	1.63 ± 0.04
MPX05	3.21E+05	2.95E+05	0.92	(7.48 ± 0.29) E+02	(6.87 ± 0.27) E+02	(7.75 ± 0.11) E+02	1.13 ± 0.05
MPX06	1.61E+05	1.45E+05	0.90	(2.01 ± 0.07) E+02	(1.81 ± 0.06) E+02	(3.99 ± 0.07) E+02	2.21 ± 0.09
MPX07	1.85E+04	1.68E+04	0.91	(6.62 ± 0.40)	(6.02 ± 0.37)	(4.76 ± 0.09) E+01	7.90 ± 0.50
MPX08	1.67E+04	1.51E+04	0.90	(1.84 ± 0.06) E+01	(1.66 ± 0.06) E+01	(4.31 ± 0.09) E+01	2.59 ± 0.10
MPX09	2.91E+04	2.76E+04	0.95	(2.70 ± 0.20) E+01	(2.56 ± 0.19) E+01	(7.39 ± 0.19) E+01	2.88 ± 0.23
MPX10	1.95E+04	1.88E+04	0.96	(1.84 ± 0.07) E+01	(1.77 ± 0.07) E+01	(4.85 ± 0.08) E+01	2.74 ± 0.11
MPX11	2.84E+04	2.73E+04	0.96	(2.93 ± 0.28)	(2.82 ± 0.27)	(7.05 ± 0.06) E+01	24.98 ± 2.38
MPX12	4.29E+04	3.94E+04	0.92	(6.78 ± 0.23) E+01	(6.24 ± 0.21) E+01	(1.07 ± 0.01) E+02	1.72 ± 0.06
MPX13	1.16E+06	1.06E+06	0.92	(3.01 ± 0.12) E+03	(2.75 ± 0.11) E+03	(2.95 ± 0.02) E+03	1.07 ± 0.04
MPX14	1.19E+07	1.07E+07	0.90	(3.26 ± 0.96) E+04	(2.93 ± 0.86) E+04	(2.97 ± 0.01) E+04	1.01 ± 0.30
MPX15	1.02E+08	9.97E+06	0.10	(1.89 ± 0.59) E+05	(1.85 ± 0.58) E+04	(5.39 ± 0.19) E+04	2.91 ± 0.91

* Anisotropy correction already taken into account
** pp inelastic cross section of 71 mb assumed [13]

Table 13. Resonance integrals for (n,α) reaction on ^{6}Li obtained from Monte Carlo calculated (MC-2010) neutron energy spectra (columns 1 and 2) and corrections of measured thermal neutron fluence to the signal not caused by thermal neutrons.

Appendix F. Description of evaluation of ATLAS-MPX measured raw data

F.1 LETP, HETP and MIP count rates

The measured values presented in Tab. 2, 7, 8, 9 and 13 are the weighted mean count rates of count rates calculated independently for each separate collision period. Collision period is defined as a time interval when MPX detectors observe significantly higher cluster rate per frame than what was the background cluster rate per frame before. The count rates are normalized per unit area and per unit luminosity and they are calculated according to Eq. (7).

$$(M_A)_j = \frac{1}{L_j} \times \frac{1}{S_B} \times \left[\left(\sum_{i=(t_1)_j}^{(t_2)_j} (N_{AB})_i \right) \times \frac{(t_2)_j - (t_1)_j}{\sum_{i=(t_1)_j}^{(t_2)_j} T_i} - \left(\sum_{i=(t_1)_j-((t_0)_j+(\Delta t)_j)}^{(t_1)_j-(t_0)_j} (N_{AB})_i \right) \times \frac{(t_2)_j - (t_1)_j}{\sum_{(t_1)_j-((t_0)_j+(\Delta t)_j)}^{(t_1)_j-(t_0)_j} T_i} \right] \quad (7)$$

where:

M_A is number of clusters of type A normalized per unit area and unit luminosity. Cluster types A can be: dots, small blobs, curly tracks, heavy blobs, heavy tracks, straight tracks.

$(N_{AB})_i$ detected number of clusters of type A below the convertor B in *i*-th frame. This number is already corrected to the track overlapping (see subsection F.3 of Appendix F). Convertor B can be: ^{6}LiF, polyethylene, polyethylene + Al, Al, thick Al, uncovered. In case of LETP, clusters from the whole sensor chip area are counted. In case of HETP, cluster only below polyethylene, polyethylene + Al, Al, thick Al, uncovered silicon are counted. In case of MIP, clusters from the whole sensor chip area are counted.

L_j integrated luminosity during the *j*-th collision period obtained from LUCID data

S_B area of the convertor B

T_i exposition time of the *i*-th frame during the *j*-th collision period

t_1, t_2 start time, end time of the *j*-th collision period

t_0 delay for summation of background

Δt time period of background summation.

The first term in the big brackets in Eq. (7) is the sum of clusters corrected for the real detector measurement time. The second term represents the subtraction of the background determined from the cluster rate before the *j*-th collision period. Time shift t_0 was introduced in order to neglect frames obtained just before or after the collision period. Such frames can include counts from short lived activation products (after a collision period) or signal from beam initialization (before the collision period) causing the overestimation of the background. In most cases the time frame of 3 hours, 0.5 hour before the start of the collision period is used for background determination. In case that the time between following collision periods is shorter than 3.5 hours, the $(t_0+\Delta t)$ value is adapted accordingly.

The count rates M_{Aj} for each cluster type A (i.e. dots, small blobs and curly tracks) were summed to provide the total count rate M_j measured during the *j*-th collision period.

The resulting value of measured count rate $\langle M \rangle$ is calculated as a weighted mean of each individual count rates obtained for each collision period (Eq. (8)) to decrease the significance of scattered data points:

$$\langle M \rangle = \frac{\sum_j [M_j \times w_j]}{\sum_j w_j} \quad (8)$$

where the weights w_j are calculated according to Eq. (9):

$$w_j = \frac{1}{\left|M_j - median([M_1, M_2, \ldots, M_{n-1}, M_n])\right|} \tag{9}$$

Index *j* goes from 1 to the total of *n* collision periods. The mean value calculated using the weights according to Eq. (9) is a suitable mean value which is not affected by occasional data points scattered far from the median (see for example Fig. 48).

The uncertainty of the weighted mean value is determined by Eq. (10) which represents the unbiased estimator of a weighted population variance:

$$\sigma(\langle M \rangle) = \sqrt{\frac{\sum_j w_j}{\left(\sum_j w_j\right)^2 - \sum_j w_j^2} \times \sum_j \left(w_j \times \left\{M_j - \langle M \rangle\right\}^2\right)} \tag{10}$$

The uncertainty calculated in such way is visualized in Fig. 48. It can be seen that this is a reliable estimation of the uncertainty of the weighted mean value <M>. It should be stressed that this uncertainty corresponds to the dispersion of the individual values of cluster rates around the weighted mean and it does not represent the measurement statistics, i.e. the real number of detected clusters. The uncertainty on the number of detected clusters is much lower and it is expressed in the appropriate subsections 6.2 - 6.5.

Table 14 summarizes areas and cluster types used for the determination of LETP, HETP and MIP count rates.

Particle group	Cluster types	Convertor areas
LETP	dot, small blob, curly track	whole sensor chip
HETP	heavy blob, heavy track	polyethylene, polyethylene + Al, Al, thick Al, uncovered Si
MIP	straight track	whole sensor chip

Table 14. Areas and cluster types used for the determination of LETP, HETP and MIP count rates.

F.2 Thermal neutron fluence

Measured values presented in Tables 2, 10 and 12 represent the weighted mean fluences per unit luminosity of fluences calculated independently for each separate collision period. Because the thermal neutron fluence is obtained from the difference of measured signal below two convertors, the equation for determination of thermal neutron fluence is slightly different from Eq. (7) used for LETP, HETP and MIP count rates. The following Eq. (11) is used:

$$(\Phi)_j = \frac{1}{L_j} \times \frac{(t_2)_j - (t_1)_j}{\sum_{k=(t_1)_j}^{(t_2)_j} T_k} \times \frac{\sum_k \left(N_{HB}^{LiF}\right)_k}{U_C \times S_{LiF}} \times \left(1 - \frac{S_{LiF}}{S_{Al}} \times \frac{\sum_k \left(N_{HB}^{Al}\right)_k}{\sum_k \left(N_{HB}^{LiF}\right)_k}\right) \tag{11}$$

where:

- Φ_j thermal neutron fluence normalized per unit luminosity calculated from the frames recorded during the *j*-th collision period,
- $(N_{HB})_k$ detected number of heavy blobs under ^{6}LiF/Al convertor in the *k*-th frame. This number is already corrected to the track overlapping (see subsection F.3 of Appendix F),
- L_j integrated luminosity during the *j*-th collision period obtained from LUCID data,
- S_{LiF} area of the ^{6}LiF convertor,
- S_{Al} area of the Al convertor,
- U_C thermal neutron detection efficiency as obtained from the measurements in isotropic thermal neutron calibration field (see Appendix B),

T_k exposition time of the *k*-th frame during the *j*-th collision period,
t_1, t_2 start time, end time of the *j*-th collision period.

Equation (11) incorporates the normalization to unit luminosity, detector real measurement time correction, conversion from cluster rate into fluence and subtraction of heavy blobs not caused by ^{6}Li disintegration (i.e. cluster rate below ^{6}LiF converter is subtracted from the cluster rate below Al converter). There should be no background heavy blobs and so no calculation of background is performed. Determination of weighted mean thermal neutron fluence, the appropriate weights and overall uncertainty is performed according to Eqs. (8), (9) and (10), respectively. The value obtained this way was then corrected to thermal neutron field anisotropy and resonance integral as described in subsections A.1.8, A.1.9 and Appendices E and H.

F.3 Track overlapping correction

Track overlapping is an effect occurring when there are too many clusters registered in one frame and so the particle tracks occasionally and randomly overlap each other causing the detection of lower number of clusters by a track pattern recognition algorithm in the tracking mode of the detector.

The correction to track overlapping is done by empirically found functions. MPX13 frames obtained during fill 1408 on 11 Oct 2010 (3500 frames with 180 000 clusters in total resulting in mean 51 clusters per frame) were used and summed together step by step to achieve up to 1200 original clusters per frame. In each step the number of clusters detected by a pattern recognition algorithm was recorded to obtain a relation between the detected and the correct number of clusters. Six correction functions are used, one for each of the cluster type (dot, small blob, curly track, heavy blob, heavy track and straight track). The same function is used for every MPX detector assuming that the correction is the same for each detector. The following equations are used for the corrections:

For less than 500 detected clusters per frame:

$$y = \frac{a + c \cdot x}{1 + b \cdot x + d \cdot x^2} \tag{12}$$

for more than 500 detected clusters per frame:

$$y = e \cdot x + f \tag{13}$$

The parameters of the Eq. (12) are stated in Tab. 15.

Cluster type	a	b	c	d
Dot	9.9935E-01	-1.7027E-03	-1.2433E-03	4.7501E-07
Small blob	9.9904E-01	-1.8017E-03	-1.2293E-03	6.0396E-07
Curly track	9.9834E-01	-1.6441E-03	-1.1524E-03	3.8796E-07
Heavy blob	9.9430E-01	-2.0916E-03	-1.3661E-03	9.2597E-07
Heavy track	1.0012	-1.0224E-03	-1.3350E-03	-5.8549E-07
MIP	1.0132	-2.2977E-03	-4.3789E-04	1.2829E-06

Table 15. Parameters of the Eq. (12) used for the correction to track overlapping.

Parameters *e* and *f* of Eq. (13) are calculated from the value of Eq. (12) at the border point. It was found experimentally that the suitable border point between the use of Eq. (12) and Eq. (13) is 500 clusters per frame because it turned out that the correction using just Eq. (12) can be unreliable for more than roughly 600 clusters per frame. However, the aim of the measurement is to keep the detected number of clusters per frame well below 500, preferably lower than 250 clusters per frame.

Figure 47 visualizes the track overlapping correction functions for different types of tracks. An example of track overlapping correction on measured data is depicted in Fig. 48.

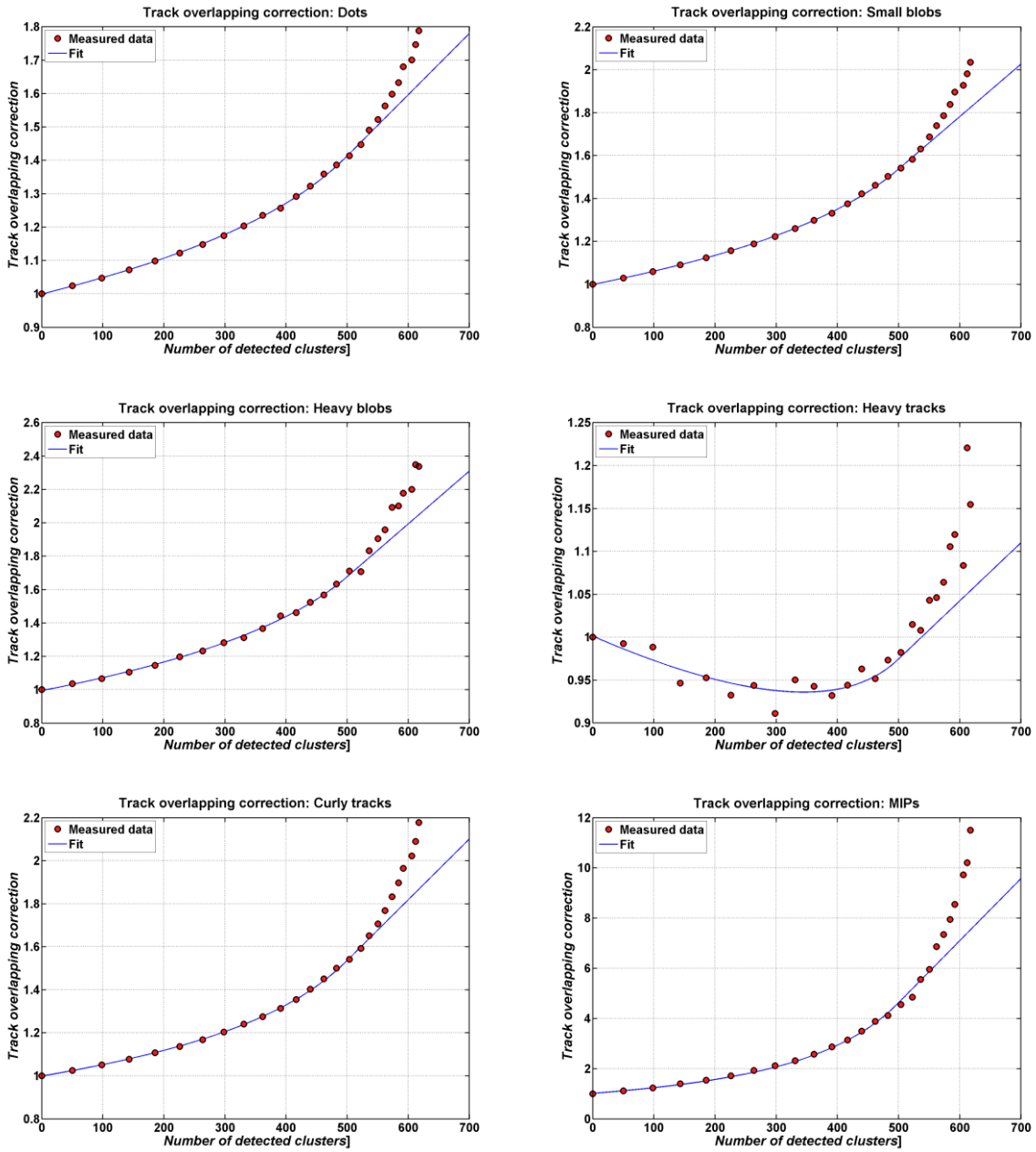

Figure 47. Track overlapping correction for different types of clusters. The correction curves (blue curves) of experimental data (red dots) uses Eq. (12) if the number of detected clusters per frame is lower than 500 and Eq. (13) if the number of detected clusters is higher than 500.

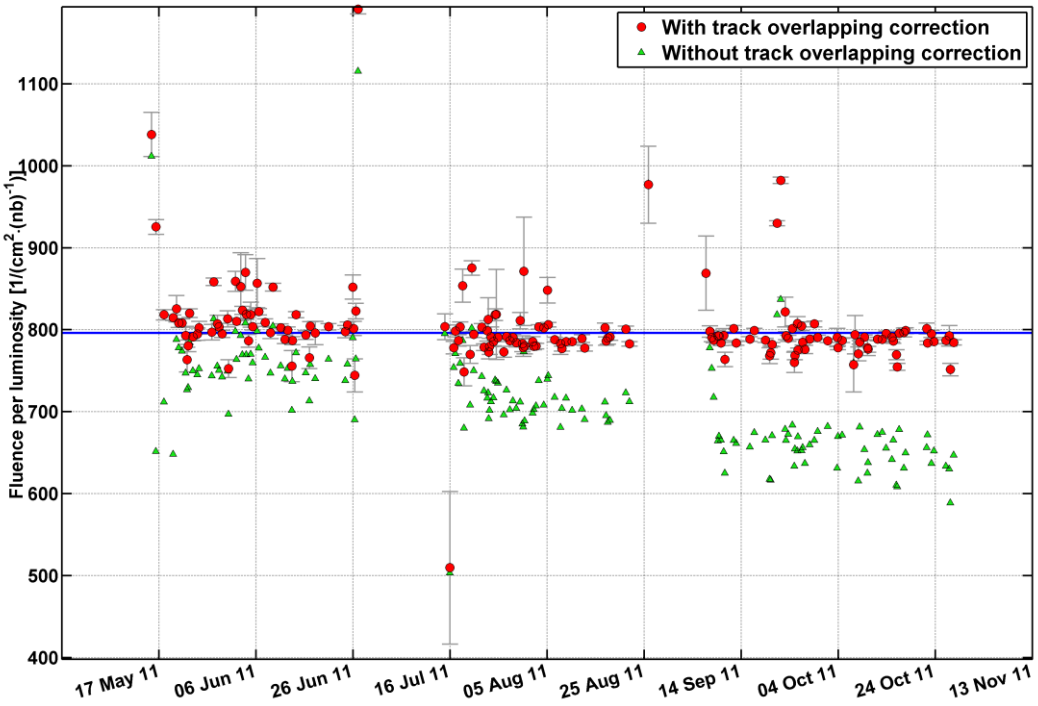

Figure 48. Example of the track overlapping correction: thermal neutron fluence per unit luminosity obtained by MPX05 from June to November 2011 independently for each collision period as calculated without (green triangles) and with (red dots) the track overlapping correction. In this case, the correction function for heavy blobs was used. Three separate groups of collision periods are visible, obviously differing by increased luminosity rate. Because the MPX05 exposition time remained the same throughout the whole 5 month period, the detector recorded more clusters per frame in each subsequent group of collision periods resulting in higher track overlapping rate and consequently requiring higher track overlapping correction.

Appendix G. Description of evaluation of MC-2010 simulated raw data

The raw MC-2010 simulation data were stored in a simple text file (the particle file). Each row in the file represents one particle which entered a pre-defined scoring volume of the annulus shape with 1 mm thickness. There were 13 scoring volumes in MC-2010 simulations at Z and R positions of MPX01 - MPX12 and MPX15. For each recorded particle, the following information was stored in the file: scoring volume (i.e., MPX detector number), particle type, energy, coordinates, and direction cosines. By analyzing the file and filtering the particles, it was possible to calculate quantities which could be compared to measurement.

The method for determination of MC-2010 LETP, HETP and MIP count rates and thermal neutron fluence consisted of three main steps. At first, the particle file was filtered to select only the particles with the energy and incident angle matching the criteria for the given quantity. The criteria are listed in section 6. Subsequently, a mean detection efficiency value ε_{MC} was assigned to each particle type included in the given signature group (LETP, HETP, MIP) according to the method described in subsection H.10 of the Appendix H. Finally, the resulting value Y of MC-2010 LETP, HETP or MIP count rate and thermal neutron fluence was obtained following Eq. (14):

$$Y = c \times \sum_{i=1}^{n} \left(N_i \times \varepsilon_i^{MC} \right) \tag{14}$$

where

N_i the number of filtered particles of type i counted to the LETP, HETP or MIP count rate or thermal neutron fluence,

ε_i^{MC} mean detection efficiency value for particles of type i obtained according to the method described in subsection H.10 of the Appendix H,

n total number of particle types included in the given quantity,

c a constant converting the quantity from "per one MC-2010 proton-proton interaction" to "per unit area and luminosity" according to Eq. (15):

$$c = \frac{\sigma \times 10^9}{N \times S} \tag{15}$$

where:

σ inelastic cross section of pp interactions at √7 TeV, σ = 71 mb [9], [13],

N number of pp collisions in MC-2010 simulation,

10^9 recalculation of the number of pp collisions for a luminosity of 1 nb^{-1},

S area of the scoring volume annulus calculated as $\pi(R^2_{max} - R^2_{min})$ for detectors oriented perpendicularly to Z-axis (MPX01 - MPX06 and MPX13 - MPX15) and as $2\pi.R.dZ$ for detectors oriented parallel to Z-axis (MPX07 - MPX12). R_{min}, R_{max} and R are inner, outer and mean radii of the scoring volume annulus, respectively.

The absolute uncertainty $\sigma(Y)$ on the MC-2010 quantities Y was calculated by Eq. (16):

$$\sigma(Y) = \sqrt{\sum_{i=1}^{n}\left(\frac{\partial Y}{\partial N_i} \times \sigma(N_i)\right)^2} = \sqrt{\sum_{i=1}^{n}\left(c \times \varepsilon_i^{MC} \times \sqrt{N_i}\right)^2} = c\sqrt{\sum_{i=1}^{n}\left(N_i \times \left[\varepsilon_i^{MC}\right]^2\right)} \qquad (16)$$

Such procedure takes into account the real detection probability of the ATLAS-MPX device allowing the most precise recalculation from MC-2010 particle angular-energy flux distribution into the detector signal.

Appendix H. Special treatment of different particle types based on detailed MC simulations of ATLAS-MPX response

This appendix describes the procedures used for assessment of:

- the contribution of photons on the LETP count rate;
- the contribution of fast neutrons on the HETP count rate;
- the contribution of charged particles on LETP, HETP and MIP count rate;
- the anisotropy correction on the thermal neutron flux.

The procedure utilizes the energy and angular detection efficiency curves of ATLAS-MPX detector obtained by Monte Carlo simulations of ATLAS-MPX response.

H.1 MC simulations of ATLAS-MPX

A detailed model of the ATLAS-MPX detector was created (see Fig. 49) and used for calculation of various quantities using the MCNPX code in version v2.7e [14]. The MCNPX is a general-purpose Monte Carlo code developed at Los Alamos National Laboratory (LANL, USA). The code is well validated by numerous benchmarks and it allows transporting nearly any type of particles. For the purpose of this report, the model was used for the following calculations:

- Determination of the angular and energy detection efficiency of the ATLAS-MPX device on monoenergetic:
  - Photons
  - Fast neutrons
  - Electrons
  - Protons
  - Muons
  - Pions
- Determination of the angular detection efficiency of the ATLAS-MPX device on thermal neutrons (thermalized neutron spectrum).

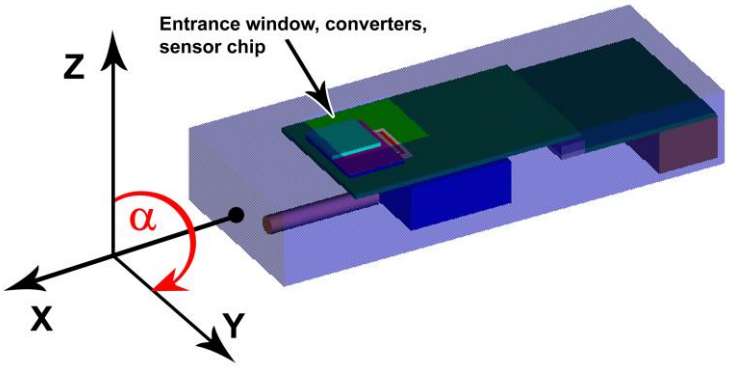

Figure 49. Visualization of the detailed model of the ATLAS-MPX detector. The duralumin box is set to be semi-transparent to see the inner structure. The position of the sensor chip is marked by the arrow.

To obtain such detection efficiency functions, the ATLAS-MPX detector model, rotated by a specified angle around x-axis, was irradiated with a parallel beam of mono energetic particles. The beam cross section was 5×5 cm^2 for all particle types except for thermal neutrons where the beam with the cross-section of 6×15.5 cm^2 was used. The beam cross section was chosen to be larger than

the sensor chip in order to include the contribution of particles scattered on MPX detector material into the detector response. The simulated quantity was the amplitude spectrum of the absorbed energy in silicon deposited by charged particles inside the sensor chip, i.e. electrons (photon detection efficiency), protons and ions (fast neutron detection efficiency), tritons and alphas (thermal neutron detection efficiency), etc. The sum N_{det} of the amplitude spectrum above the preset energy limit is related to the detection efficiency ε according to the Eq. (17):

$$\frac{N_{src}}{S_{src}} = \frac{N_{det}}{S_{det} \times \varepsilon} \tag{17}$$

where:

N_{src} number of simulated source particles

S_{src} area of the source

N_{det} number of simulated counts in the detector amplitude spectrum above the preset energy threshold. All charged particles are counted, both primary and secondary, e.g., in the simulation of muon detection efficiency, both primary muons and secondary electrons are included in the simulated impulses.

S_{det} area of the sensitive part of the detector (e.g., area below ^{6}LiF in thermal neutron simulations)

ε detection efficiency

The lower energy detection limit was 7 keV for photon, electron, proton, muon and pion detection efficiencies and 230 keV for thermal and fast neutron detection efficiencies.

The assumption was made that the angular and energy detection efficiencies calculated for the rotation around the x-axis are the same as for the detector rotated around the y-axis. This simplifies the calculation of the corrections for thermal neutron fluences and mean detection efficiencies as described in subsections H.5, H.6 and H.7 of Appendix H. It is supposed that the error introduced by this assumption, e.g. the change in mean detection efficiency as calculated from MC-2010 data, is small.

H.2 Angular and energy detection efficiencies for photons

The detection efficiencies were calculated for 17 photon energies from 10 keV up to 1 GeV and 13 angles from 0° to 180°. The dependence for selected energies and angles is visualized in Fig. 50a and Fig. 50b.

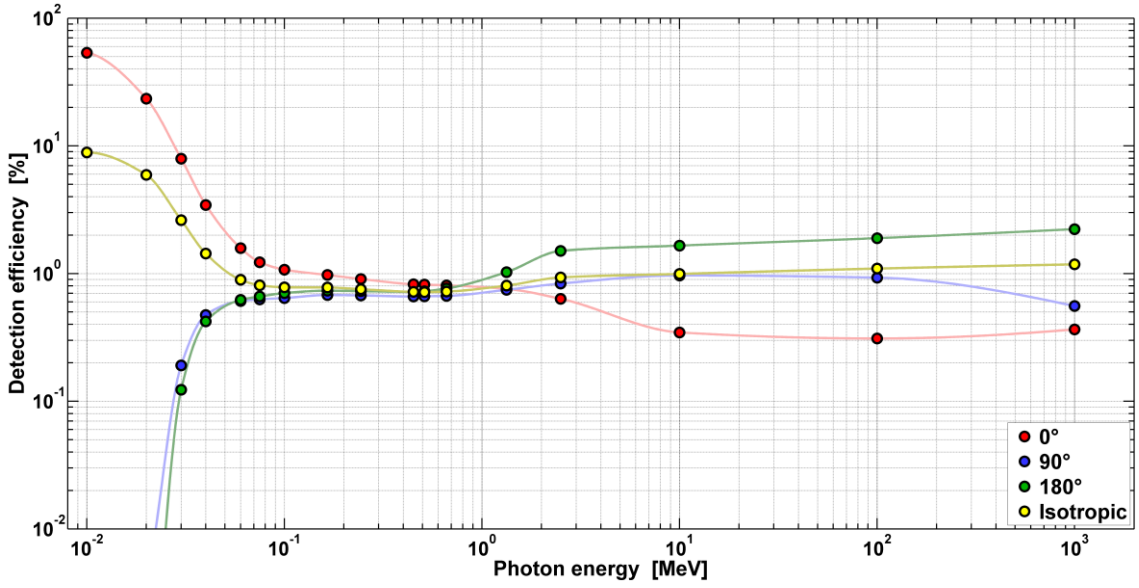

a)

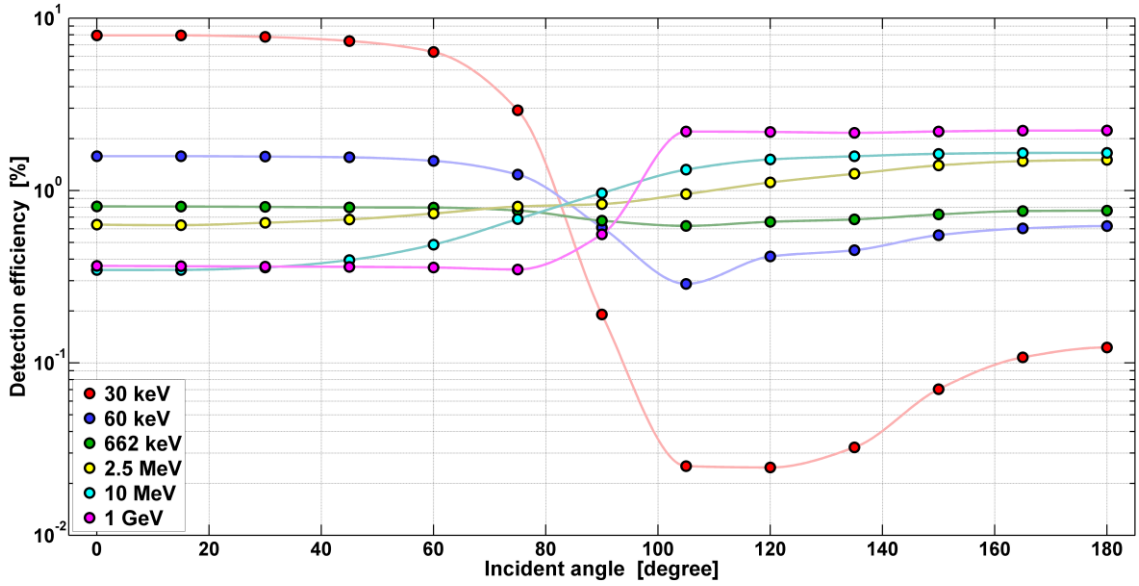

b)

Figure 50. a) The detection efficiencies for mono energetic photons incident on the sensor chip at the angles of 0°, 90° and 180° and with the isotropic angular distribution. b) Angular detection efficiencies for mono energetic photons with the energy of 30, 60 and 662 keV and 2.5, 10 and 1000 MeV.

H.3 Angular and energy detection efficiencies for fast neutrons

The detection efficiencies were calculated for 19 neutron energies from 500 keV up to 1 GeV and 13 angles from 0° to 180°. The dependence for selected energies and angles is visualized in Fig. 51a and Fig. 51b. The minimum energy transferred by neutron to silicon nucleus by elastic recoil had to be 230 keV to be treated as a registered fast neutron.

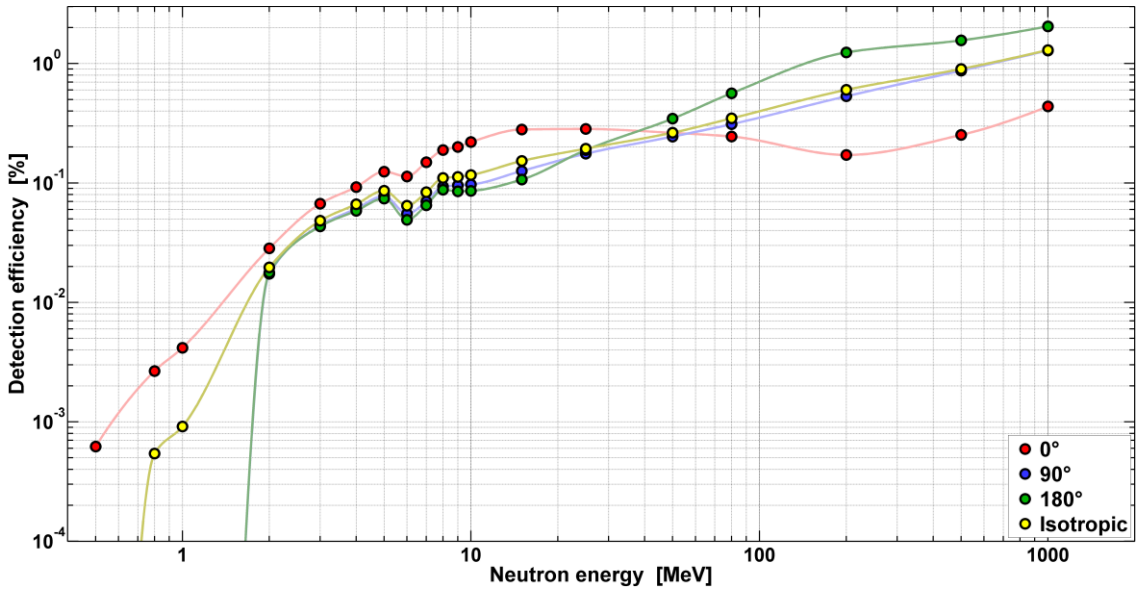

a)

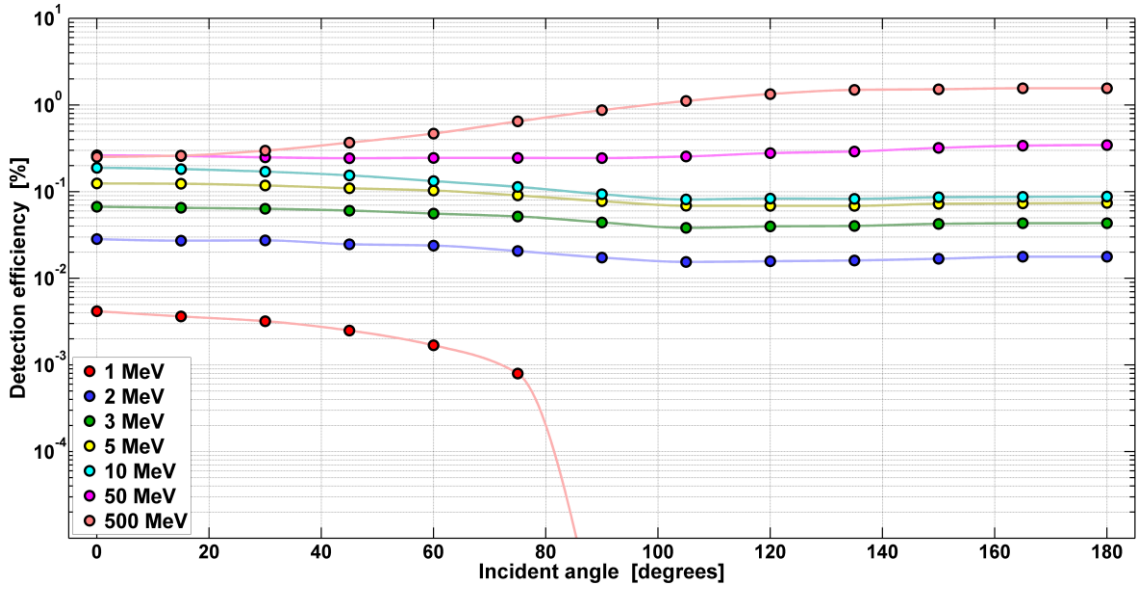

b)

Figure 51. a) The detection efficiencies for mono energetic neutrons incident on the sensor chip at the angles of 0°, 90° and 180° and with the isotropic angular distribution. b) Angular detection efficiencies for mono energetic neutrons with the energy of 1, 2, 3, 5, 10, 50 and 500 MeV.

H.4 Angular and energy detection efficiencies for electrons

The detection efficiencies were calculated for 26 electron energies from 10 keV up to 1 GeV and 13 angles from 0° to 180°. The dependence for selected energies and angles is visualized in Fig. 52a and Fig. 52b.

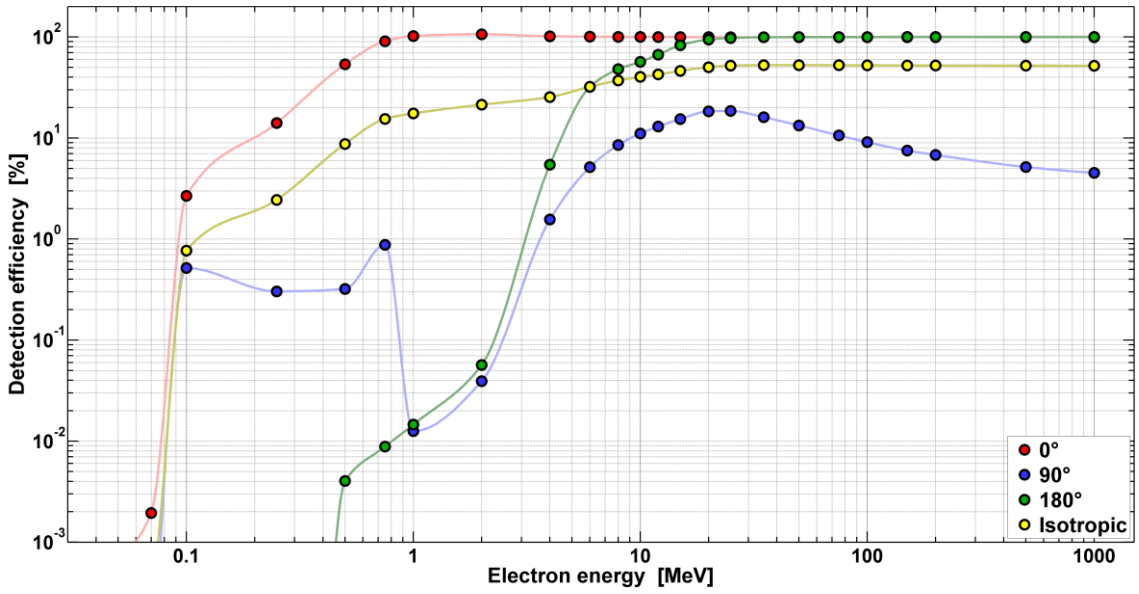

a)

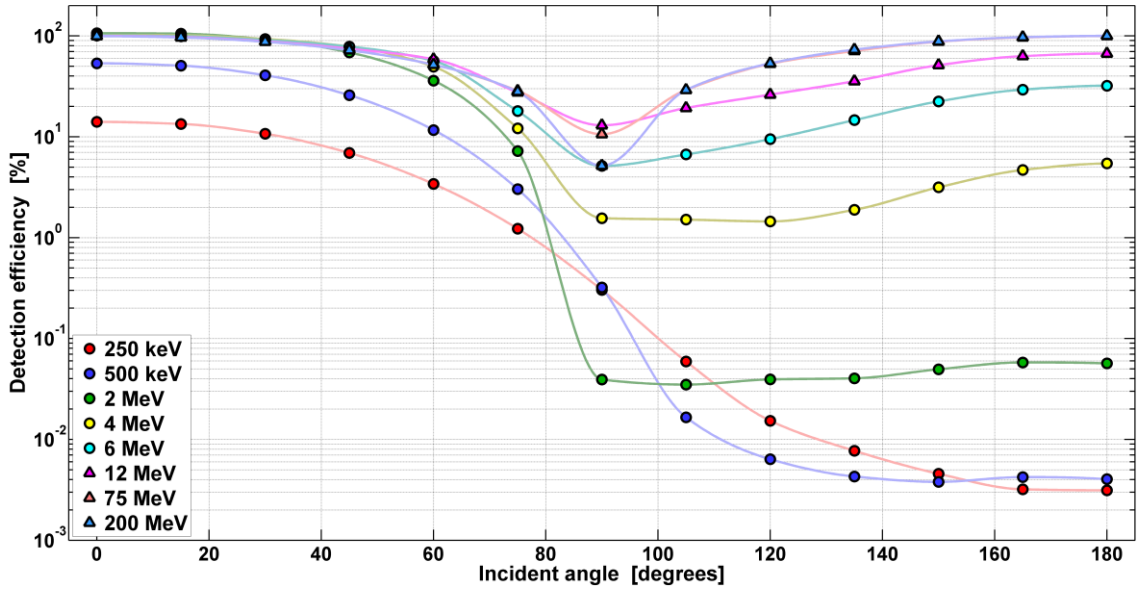

b)

Figure 52. a) The detection efficiencies for mono energetic electrons incident on the sensor chip at the angles of 0°, 90° and 180° and with the isotropic angular distribution. b) Angular detection efficiencies for mono energetic electrons with the energy of 0.25, 0.5, 2, 4, 6, 12, 75 and 200 MeV.

H.5 Angular and energy detection efficiencies for protons

The detection efficiencies were calculated for 18 proton energies from 300 keV up to 500 MeV and 13 angles from 0° to 180°. The dependence for selected energies and angles is visualized in Fig. 53a and Fig. 53b.

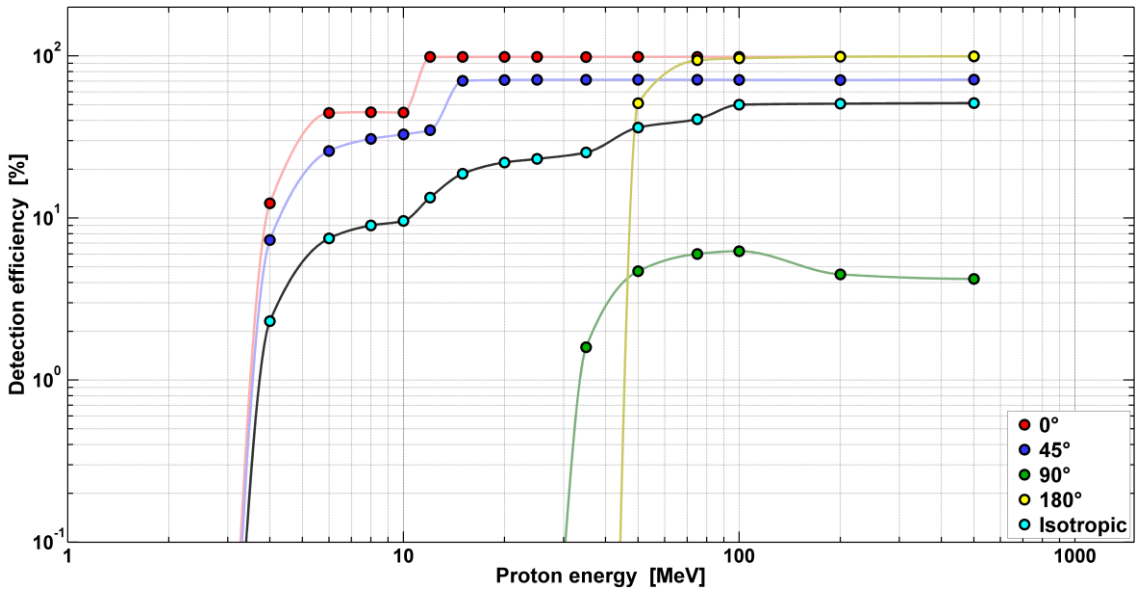

a)

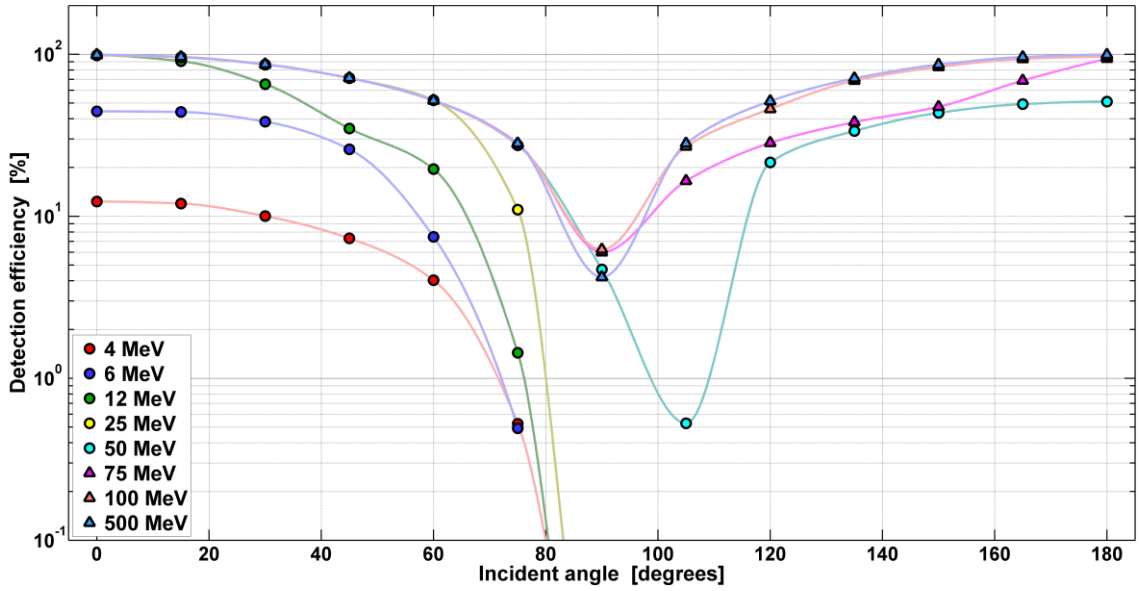

b)

Figure 53. a) The detection efficiencies for mono energetic protons incident on the sensor chip at the angles of 0°, 45°, 90° and 180° and with the isotropic angular distribution. b) Angular detection efficiencies for mono energetic protons with the energy of 4, 6, 12, 25, 50, 75, 100 and 500 MeV.

H.6 Angular and energy detection efficiencies for muons

The detection efficiencies were calculated for 20 muon energies from 500 keV up to 1 GeV and 13 angles from 0° to 180°. The dependence for selected energies and angles is visualized in Fig. 54a and Fig. 54b.

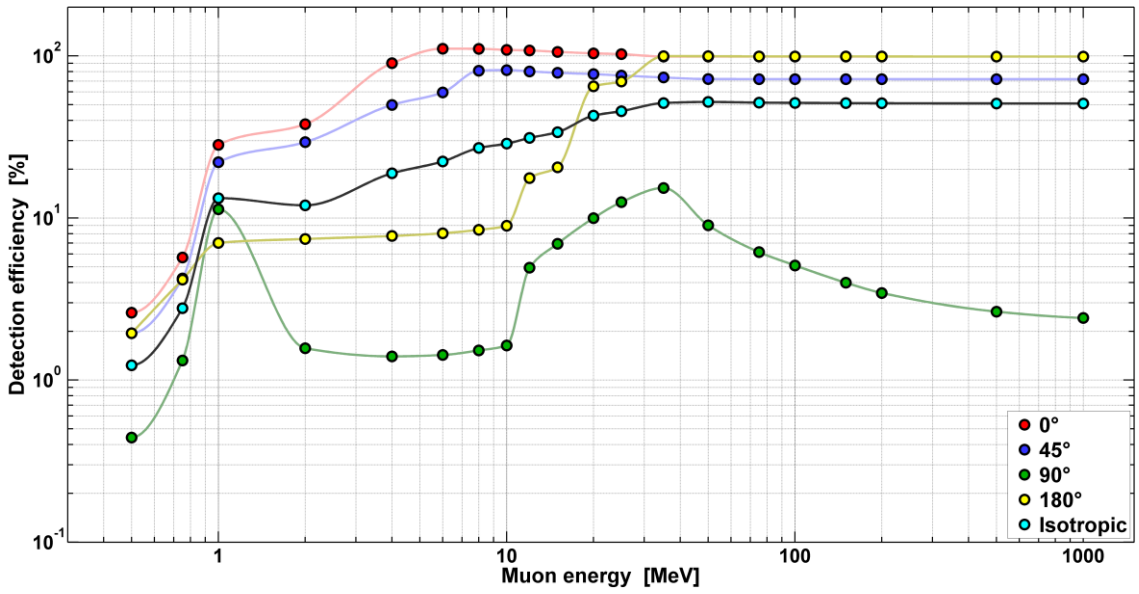

a)

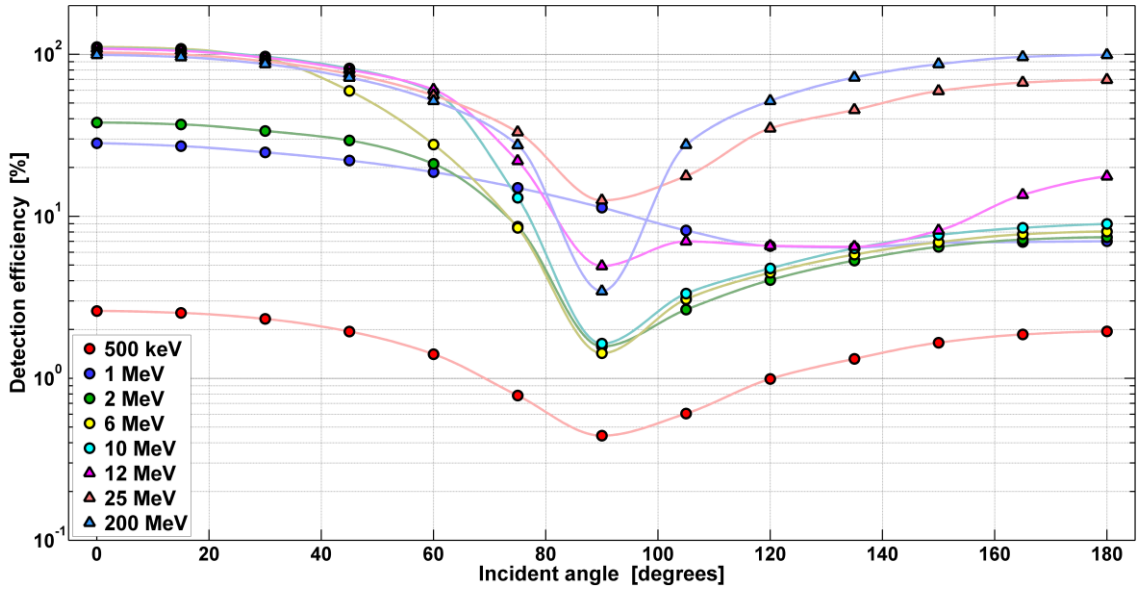

b)

Figure 54. a) The detection efficiencies for mono energetic muons incident on the sensor chip at the angles of 0°, 45°, 90° and 180° and with the isotropic angular distribution. b) Angular detection efficiencies for mono energetic muons with the energy of 0.5, 1, 2, 6, 10, 12, 25 and 200 MeV.

H.7 Angular and energy detection efficiencies for pions

The detection efficiencies were calculated for 18 pion energies from 1 MeV up to 1 GeV and 13 angles from 0° to 180°. The dependence for selected energies and angles is visualized in Fig. 55a and Fig. 55b.

a)

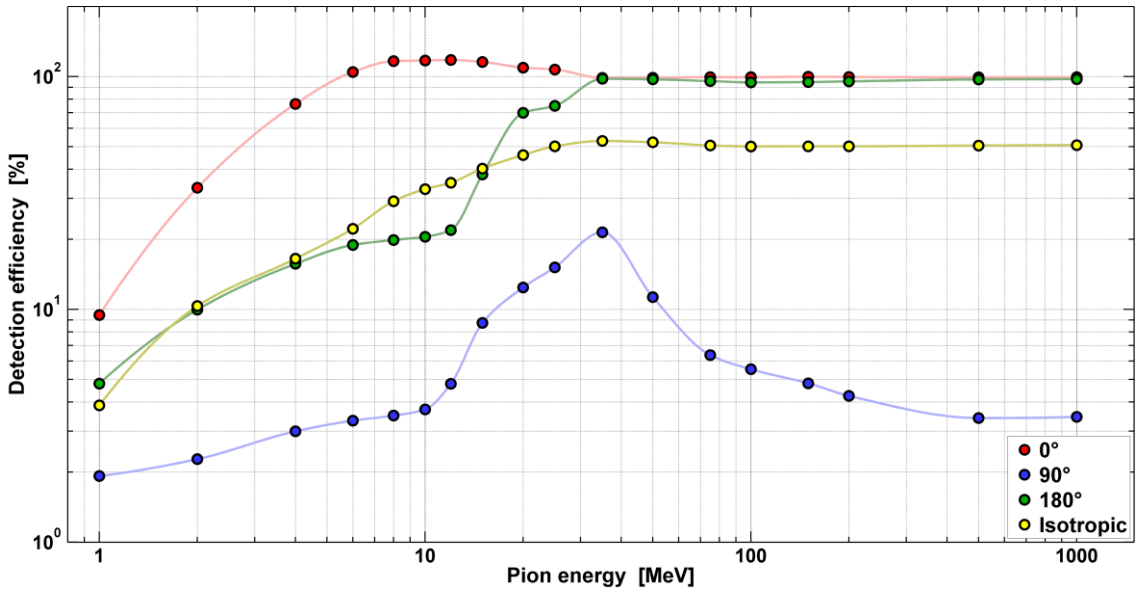

b)

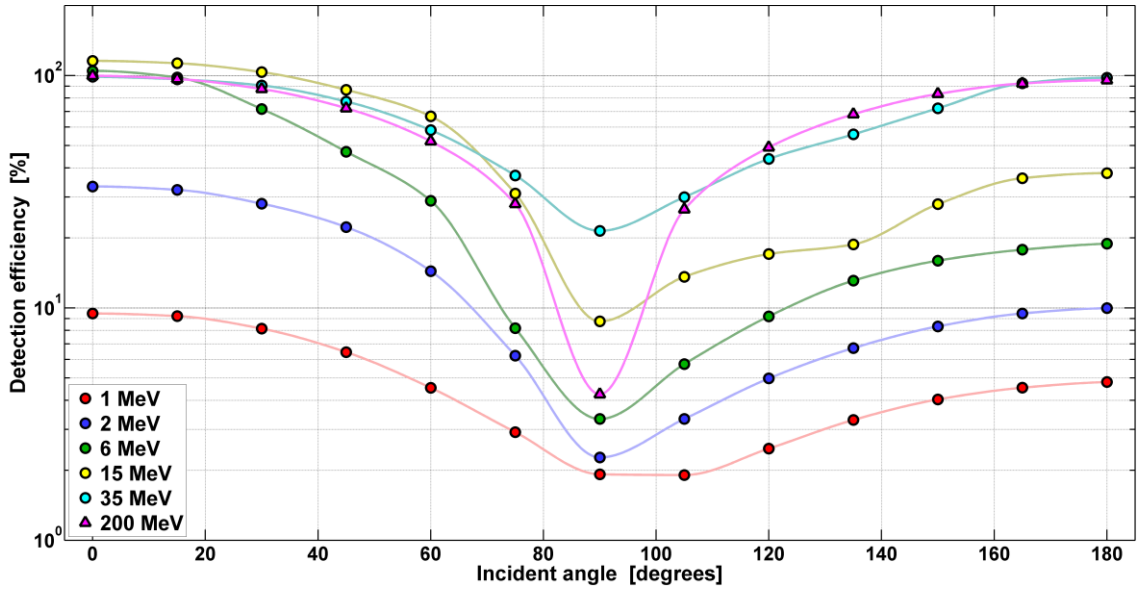

Figure 55. a) The detection efficiencies for mono energetic pions incident on the sensor chip at the angles of 0°, 90° and 180° and with the isotropic angular distribution. b) Angular detection efficiencies for mono energetic pions with the energy of 1, 2, 6, 15, 35 and 200 MeV.

H.8 Angular detection efficiencies for thermal neutrons

The detection efficiencies were calculated for thermalized neutron spectrum with the Maxwell-Boltzmann distribution of neutron energies corresponding to the temperature of 290 K. The detection efficiency as a function of the incident angle is shown in Fig. 56.

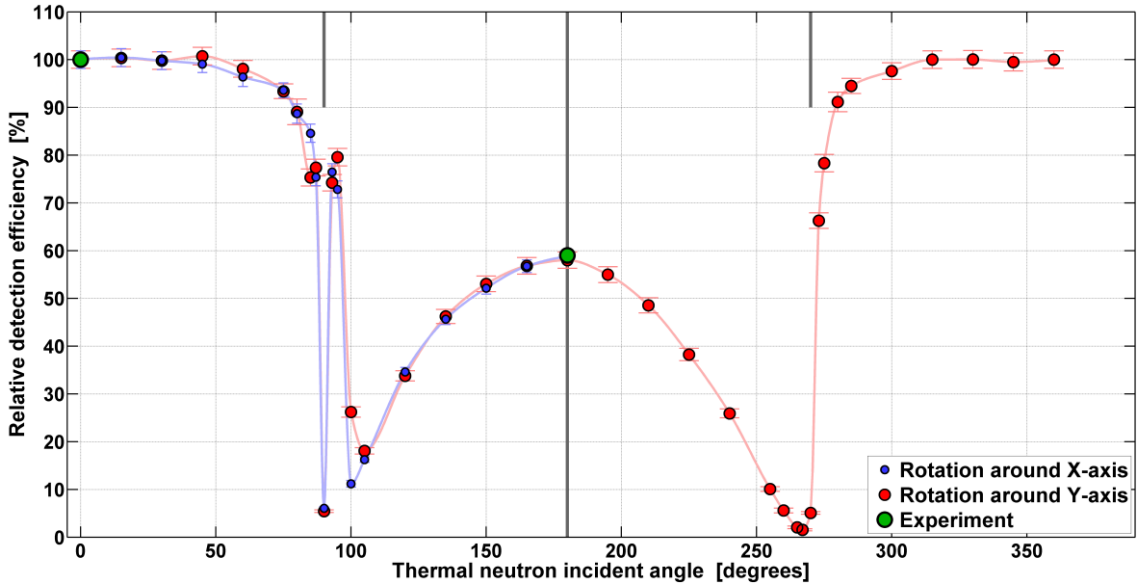

Figure 56. Angular detection efficiency for thermal neutrons. The narrow peak around 95° is caused by neutrons coming into the ^{6}Li converter layer from beneath the converter not yet shielded by the silicon of the sensor and readout chip.

H.9 Determination of thermal neutron field anisotropy correction

The response of ATLAS-MPX detectors was calibrated in isotropic thermal neutron flux field available at the Czech Metrology Institute. However, the thermal neutron flux field at positions of MPX detectors in ATLAS can be anisotropic as resulted from MC-2010 simulations. That is why an anisotropy correction to the measured data is introduced to reflect the actual thermal neutron field at each MPX detector.

This correction utilizes the angular distribution of thermal neutron direction vectors obtained from MC-2010 simulations and angular detection efficiency curve for thermal neutrons obtained from MCNPX simulations (see subsection H.8 of Appendix H). The following algorithm is used to calculate the anisotropy correction:

For every thermal neutron from the MC-2010 simulation, an incident angle is calculated and corresponding *relative detection efficiency* ε_{Aj} is interpolated from a 1D angular detection efficiency curve presented in Fig. 56. Linear interpolation is used. Incident angle is an angle between negative sensor chip normal and the particle direction vector. It can reach values between 0° (particle incidents on a chip from the front) and 180°. The index *j* represents the ordinal number of the thermal neutron. A detection efficiency weight is applied for each particle entering an MC-2010 scoring volume from the thin sides (i.e. perpendicular to sensor chip plane). The weight is calculated as follows:

$$w_j = \frac{R_{max} - R_{min}}{z_{max} - z_{min}} \tag{18}$$

for the scoring volumes thin in *dz* and thick in *dR* (i.e., MPX01 - MPX06 and MPX13 - MPX15), and

$$w_j = \frac{z_{max} - z_{min}}{R_{max} - R_{min}} \tag{19}$$

for the scoring volumes thin in *dR* and thick in *dz* (i.e., MPX07 - MPX12). R_{min}, R_{max}, z_{min} and z_{max} are the inner and outer radius and lower and higher *z*-axis coordinates of the scoring volume annulus, respectively. The weights compensate the under sampling of particle numbers with direction vector parallel to thick planes of scoring volume annulus. The weight w_j for particles entering the scoring volume from other (i.e., thick) sides is equal to 1.

The *weighted mean detection efficiency* ε_{MC} obtained from all MC-2010 thermal neutron data for the given MPX detector is then calculated according to the Eq. (20):

$$\varepsilon_{MC} = \frac{\sum_j (\varepsilon_{Aj} \times w_j)}{\sum_j w_j} \tag{20}$$

The *weighted detection efficiency for isotropic field* ε_{iso} has to be calculated from values presented in Fig. 56 by weighting them by the difference of cosines i.e. with an area of a spherical zone visible from the sphere center at the given angle interval (see Eq. (21)):

$$\varepsilon_{iso} = \frac{1}{2} \times \sum_i \frac{\varepsilon(\theta_i)}{\varepsilon(\theta = 0°)} \times [(\cos(\theta_i + \delta) - \cos(\theta_i - \delta)] \tag{21}$$

where:

$\varepsilon(\theta_i)$	thermal neutron detection efficiency for the incident angle θ_i
$\varepsilon(\theta = 0°)$	thermal neutron detection efficiency for the incident angle of reference, 0°
$cos(\theta_i \pm \delta)$	cosine of incident angle θ_i changed by δ - half of the width of angle interval $< \theta_{i-1}, \theta_i >$ or $< \theta_i, \theta_{i+1} >$

Number 2 in the denominator represents the normalization sum of the cosines expression inside angle brackets over all indexes *i*. The structure of Eq. (21) is similar to Eq. (20). The value of ε_{iso} is a constant equal to 0.623 (relative to the detection efficiency for 0° incident angle) and it is the same for all MPX detectors as far as the angular detection efficiencies do not change from detector to detector.

The thermal neutron field anisotropy correction is then obtained as a ratio of ε_{iso} and ε_{MC}. The measured value of thermal neutron fluence should be multiplied by this number to apply the correction. Values of the correction for all MPX detectors are presented in Tab. 10. The correction varies between 0.79 (i.e., the correct value of flux is lower) and 1.04 (i.e., the correct value of flux is higher).

H.10 Determination of contribution of different particle types into LETP, HETP and MIP count rate

Contribution of different particle types to the MC-2010 simulated count rates can be estimated if an angular and energy detection efficiencies of an MPX detector for the given particle type is known. The requested efficiencies were obtained using MCNPX simulations and the resulting values are visualized in Figures 50 to 55.

Table 16 presents the particle types for which the contribution to the simulated LETP, HETP and/or MIP count rates was obtained by the method described in this chapter.

Particle type	LETP	HETP	MIP
photons	×	-	-
electrons	×	-	×
protons	×	×	×
fast neutrons	-	×	-
muons	×	×	×
charged pions	×	×	×
charged kaons	×	×	×

Table 16. Summary of the investigated contribution of different particle types into the value of simulated count rates.

The method for the determination of the contribution of different particle types to the simulated count rates for each MPX device from the particle energy and angular distribution as predicted by MC-2010 simulations is analogous to the one described for thermal neutrons in subsection H.9 of Appendix H. The main steps are as follows:

For every particle of given particle type (in addition, the particles can be filtered by energy or incident angle) from the MC-2010 simulation, an incident angle is calculated and a corresponding *detection efficiency* ε_{Aj} is interpolated from a 2D angular-energy detection efficiency function. The efficiency curves for selected angles and energies are presented in Figures 50 to 55. 2D linear interpolation of data points plotted in logarithmic energy and efficiency axes and linear angular axis is used. Index *j* represents the particle ordinal number.

A detection efficiency weight is applied for each particle entering a scoring volume from the thin sides (i.e. perpendicular to sensor chip plane) according to Eqs. (18) and (19). The weights compensate the under sampling of particle numbers with direction vector parallel to thick planes of scoring volume annulus.

The weight for particles entering the scoring volume from other (i.e., thick) sides is equal to 1. The *weighted mean detection efficiency* ε_{MC} obtained from MC-2010 angular and energy distribution is then calculated according to Eq. (22):

$$\varepsilon_{MC} = \frac{\sum_j \left(\varepsilon_{Aj} \times w_j\right)}{N} \tag{22}$$

where N is the total number of particles of given type, energy and incident angle filtered from MC-2010 particle file.

For example for photons, the common value of ε_{MC} varies around 1.5%. This is weighted photon detection efficiency, not the real mean photon detection efficiency. The difference is that the weighted detection efficiency takes into account, in addition, the detection efficiency to the photons which were not recorded in the MC-2010 particle file (i.e., they did not enter a scoring volume) because the scoring volume is very thin in one dimension resulting in under sampling the number of particles which enter the scoring volume through the thin sides.

The resulting contribution of a given particle type into simulated LETP, HETP or MIP count rate of the given MPX detector is then calculated as a product of the weighted mean detection efficiency ε_{MC} calculated for such MPX detector and the (by energy/angle filtered) number of particles of the given type per unit area and luminosity recorded in the MC-2010 scoring volume representing this MPX detector.

The photon contribution to the simulated LETP count rate is presented in Tab. 7. For most of the MPX detectors, the contribution varies between 67% and 86% of the total simulated LETP count rate.

The fast neutron contribution to the simulated HETP count rate is presented in Tab. 8. For most of the MPX detectors, the contribution varies between 43% and 100% of the total simulated HETP

count rate. The farther is the MPX detector from the interaction point, the higher is the contribution of fast neutrons into the simulated HETP count rate.